Unraveling Luminescent and Enabling Photocatalytic Processes of Double and Lead Halide Perovskite Nanocrystals

Fei He

Munich, 2025

Unraveling Luminescent and Enabling Photocatalytic Processes of Double and Lead Halide Perovskite Nanocrystals

Dissertation

zur Erlangung des Doktorgrades der Naturwissenschaften (Dr. rer. nat.)

an der Fakultät für Physik

der Ludwig-Maximilians-Universität München

vorgelegt von

Fei He

aus Shandong, China

München, 11. August 2025

Erstgutachter:	Prof. Dr. Jochen Feldmann
Zweitgutachter:	Prof. Dr. Emiliano Cortés
Tag der mündlichen Prüfung:	9. Oktober 2025

Publications, Conferences, and Awards

Scientific Publications of Results Presented in This Work

- F. He, Y. Wang, T. Debnath, M. Döblinger, Q. A. Akkerman, J. Feldmann, A. Dey
  Silver-Nanoclusters and Vacancies Influence the Optical Properties of Spherical $Cs_2AgBiCl_6$ Nanocrystals
  Advanced Optical Materials 12, 2302898 (2024)

- L. Wu,[†] F. He,[†] H. Du, Y. Zhang, S. Ghimire, M. Stein, H. Huang, L. Polavarapu, Q. Zhang, J. Feldmann, T. Debnath, Y. Wang
  Light-Driven Hydrogen Generation from Methanol Vapor Using Halide Perovskite Nanocrystals
  ACS Energy Letters 10, 2978-2985 (2025)

Additional Publications

- J. G. Mann, F. He, Q. A. Akkerman, T. Debnath, J. Feldmann
  A Bound Exciton Resonance Modulated by Bulk and Localized Coherent Phonons in Double Perovskites
  The Journal of Physical Chemistry Letters 15, 2169-2176 (2024)

- A. Dey, S. Strohmair, F. He, Q. A. Akkerman, J. Feldmann
  Fast Electron and Slow Hole Spin Relaxation in $CsPbI_3$ Nanocrystals
  Applied Physics Letters 121, 201106 (2022)

Conferences and Workshops

- *German Physical Society (DPG) Spring Meeting (Talk)*
  Dresden, Germany, March 2023

- *12th SolTech Conference 2023 (Poster)*
  Würzburg, Germany, October 2023

- *MATSUS24: Materials for Sustainable Development Conference Spring (Talk)*
  Barcelona, Spain, March 2024

Zusammenfassung

Kolloidale Halbleiter-Nanokristalle (NK) haben sich aufgrund ihrer einstellbaren optoelektronischen Eigenschaften und fortschrittlichen Synthesemethoden, die einheitliche und gut definierte Strukturen ermöglichen, zu einer wichtigen Plattform in der Nanomaterialforschung entwickelt. Ihr größenabhängiges Verhalten macht sie sowohl für die Grundlagenforschung als auch für technologische Anwendungen vielseitig einsetzbar. Unter ihnen zeichnen sich Blei-Halogenid-Perowskit (BHP)-NK durch ihre hervorragende Leistung in lichtabsorbierenden, -emittierenden und -detektierenden Anwendungen aus, was auf ihre hohe Fehlertoleranz und vereinfachte Bandstruktur zurückzuführen ist. Ihre praktische Anwendung wird jedoch durch geringe Feuchtigkeitsstabilität und die hohe Bleitoxizität eingeschränkt.

BHP NK zeigen großes Potenzial für die photokatalytische Wasserstoffproduktion, da sie hohe Absorptionskoeffizienten und lange Ladungsträger-Diffusionslängen besitzen. Ihre Zersetzung in polaren Lösungsmitteln begrenzt jedoch die Einsatzmöglichkeit für diese Anwendung. In dieser Arbeit wird eine Dampfphasenstrategie vorgestellt, die eine Feststoff-Gas-Grenzfläche etabliert, um den Kontakt zwischen polaren Flüssigkeiten und BHP-Nanoplättchen (NPl) zu minimieren. Die über 20 Stunden unter simuliertem Sonnenlicht aufrechterhaltene Wasserstoffentwicklungsrate der BHP NPl/Platin (Pt)-Katalysatoren bestätigt die Machbarkeit des Ansatzes. Zur Untersuchung des Ladungsträgertransfers von BHP NPl zu Pt-Cokatalysatoren wird zeitaufgelöste Photolumineszenz (PL)-Spektroskopie eingesetzt. Die Ergebnisse verdeutlichen die zentrale Rolle der Exzitonen-Diffusion, modelliert mit exponentieller Zeitverteilung, welche durch Größe, Geometrie und Konzentration der NPl und Pt-Nanocluster beeinflusst wird. Transiente Absorptionsspektroskopie zeigt zudem ultraschnellen Elektronentransfer von BHP NPl zu Pt-Nanoclustern.

$Cs_2AgBiCl_6$-Doppelperowskit (DP)-NK bieten eine vielversprechende bleifreie Alternative zu BHP und zeigen Potenzial für weiße Lichtemission. Das breite PL-Spektrum mit zwei Emissionspeaks wird bei $Cs_2AgBiCl_6$-NK mit indirekter Bandlücke beobachtet, deren Ursprünge bislang umstritten waren. Mittels PL-Anregungs- und temperaturabhängiger PL-Spektroskopie werden diese in dieser Arbeit aufgeklärt. Die rote Emission stammt von defektgebundenen Exzitonen mit hoher Oszillatorstärke, was den starken Absorptionspeak mit hoher Bindungsenergie erklärt. Die blaue Emission steht in engem Zusammenhang mit der Oberflächenchemie und hängt stark von der Synthesemethode ab. Diese Ergebnisse unterstreichen die zentrale Rolle von Silber für die optischen Eigenschaften der $Cs_2AgBiCl_6$-NK.

Die Ergebnisse dieser Arbeit liefern wertvolle Erkenntnisse zur Optimierung von Perowskit-NK in praktischen Anwendungen, insbesondere hinsichtlich der Verbesserung der Feuchtigkeitsstabilität in der Photokatalyse und der Reduzierung der Toxizität bei Weißlichtemission.

Abstract

Colloidal semiconductor nanocrystals (NCs) have become a key platform in nanomaterial research due to their tunable optoelectronic properties, and advanced synthesis methods that yield uniform, well-defined structures. Their size-dependent behavior—from quantum-confined to bulk-like regimes—makes them highly versatile for both fundamental studies and device applications. Among them, lead halide perovskite (LHP) NCs stand out for their exceptional performance in light absorbing, emitting, and detecting applications, thanks to their high defect tolerance and a simplified band structure. However, their practical use remains limited by poor moisture stability and the high toxicity of lead.

LHP NCs show significant potential for photocatalytic hydrogen production due to their high absorption coefficients and long charge-carrier diffusion lengths. However, their degradation in polar solvents limits the use of LHPs in this application. This thesis proposes a vapor-phase strategy to address this limitation by establishing a solid–gas interface that minimizes direct contact between liquid polar solvents and LHP nanoplatelets (NPls). The sustained high hydrogen evolution rate of LHP NPls/platinum (Pt) over 20 hours under simulated solar light demonstrates the feasibility of the developed vapor-phase approach, characterized by the vapor composition and different types of LHP NPls. To elucidate the charge carrier transfer mechanism from the LHP NPls to Pt cocatalysts, time-resolved photoluminescence (PL) spectroscopy is employed. The results highlight the critical role of exciton diffusion, modeled with an exponential time distribution. The diffusion time distribution is influenced by the size and geometry of NPls and the concentration of Pt nanoclusters. Moreover, transient absorption spectroscopy further reveals ultrafast electron transfer dynamics from LHP NPls to Pt nanoclusters.

On the other hand, $Cs_2AgBiCl_6$ double perovskite (DP) NCs offer a potential lead-free alternative to LHPs, showing promise for white light emission. The broad PL spectrum featuring dual emission peaks is observed in $Cs_2AgBiCl_6$ NCs with an indirect bandgap, the origins of which have been under debate. The study clarifies their origins using PL excitation and temperature-dependent PL spectroscopy. The red emission comes from excitonic recombination of defect-bound excitons with a giant oscillator strength, explaining the strong absorption peak with an extralarge binding energy. The blue emission closely relates to the surface chemistry of the DP NCs, associated with the synthetic methods. These findings underscore the critical role of silver in determining the optical properties of $Cs_2AgBiCl_6$ NCs.

The results in this thesis offer valuable insights for optimizing the performance of perovskite NCs in practical applications, including mitigating moisture instability in photocatalysis and reducing toxicity in white light emission systems.

Table of Contents

1

Introduction

The conceptual foundation of nanotechnology laid by Richard Feynman in his visionary 1959 lecture–There's Plenty of Room at the Bottom– highlighted the vast potential of manipulating matter at the atomic and molecular scale.[1] He anticipated a future where materials and devices could be engineered with atomic precision. This idea has since inspired the development of nanoscience, enabling breakthroughs in fields ranging from electronics to energy conversion.

Advances in ultrafast spectroscopy over the ensuing decades significantly propelled nanoscale research, ultimately giving rise to a specialized branch of nanotechnology centered on colloidal semiconductor nanocrystals (NCs). Currently, a wide range of semiconductor NCs with precise structural, compositional, and size control are being actively explored.[2] The diversity of these NCs enables a broad spectrum of optoelectronic applications, including light-emitting diodes (LEDs), photovoltaics, transistors, biomedicine, and photo/electrocatalysis.[3–5] To meet the growing demands in these sectors, continued efforts are required in two key research areas: the discovery and development of novel materials with targeted performance advantages, and the fundamental investigation of their properties using advanced characterization techniques.

Thanks to their remarkable optical properties such as a large absorption cross-section, bright and narrow-band emission, high charge carrier diffusion lengths, and exceptional defect tolerance, lead halide perovskite (LHP) NCs have rapidly regained research prominence since their first successful colloidal synthesis in 2014.[6] This resurgence followed the groundbreaking discovery of perovskites for photovoltaic applications in 2009.[7] Over the past decade, significant advances have been made in the colloidal synthesis of LHP NCs, enabling precise control over their composition, size, morphology, surface chemistry, and self-assembly behavior.[8]

The sizes of NCs can be precisely tuned within the sub-10 nm range with the strong/weak quantum confinement regimes, making excitonic transition bands distinguishable.[9,10] Over the past decade, the power conversion efficiency of perovskite solar cells (PSCs) has increased dramatically to 25.0%, placing them at the forefront of the drive toward next-generation, cost-effective photovoltaic and integrated energy technologies, in direct competition with established silicon-based photovoltaics.[8] Furthermore, LHPs show great promise for LEDs, offering full-color display capabilities with wide color gamut, high color purity, and high luminescence efficiencies.[11]

Although LHPs show great potential in replacing traditional semiconductors for various optoelectronic applications, they show intrinsic drawbacks which hinder the commercialization—moisture instability and high toxicity. This thesis focuses on addressing and mitigating these two challenges in the context of specific application requirements.

On one hand, humidity has been identified as the primary factor driving instability in LHP devices. Besides moisture, LHPs are soluble in most polar solvents. This limits the use of LHPs for photocatalytic hydrogen production, which requires polar reactants capable of donating protons. LHP NCs show significant potential for photocatalytic hydrogen production due to their high absorption coefficients and long charge-carrier diffusion lengths, which enhance the photogeneration and utilization of charge carriers.[12] To overcome instability challenges, strategies such as using hydrohalic acid solutions and encapsulation have been developed.[13,14] However, these approaches face practical limitations for industrial application, due to either insufficient long-term stability or low hydrogen yield, respectively. When exposed to water molecules, LHPs interact with them through a series of reactions—hydration, phase transformation, decomposition, and dissolution.[15] It has been demonstrated that the hydration process, defined as the rapid formation of hydrogen bonds between water and organic cations, is reversible when water is taken away from the system.[16,17] On the basis, further studies are needed to manipulate the polar atmosphere for LHP photocatalysis and to investigate the underlying mechanisms.

On the other hand, the presence of lead in LHPs raises significant environmental and health concerns. Double perovskites (DPs) have attracted considerable attention as potential lead-free alternatives to LHPs due to their less toxicity.[18] Bismuth with its ionic radius and electronic configuration similar to lead, is a promising candidate for incorporation into DPs to retain desirable optical properties while improving environmental safety.[19] Among the family of bismuth-based DPs, Cs_2AgBiX_6 (X = Br, Cl) exhibits broad PL spectra, long charge carrier lifetimes, and good thermal and environmental stability.[20,21] By alloying with metal ions such as sodium, indium, they can achieve a high PL quantum yield, potential for single-emitter white light LEDs.[22] However, the origin of their broad emission remains a subject of ongoing debate. To optimize their performance for next-generation lighting and display technologies, further investigation is needed to clarify the charge recombination processes in Cs_2AgBiX_6.

In this thesis, optical spectroscopy is employed to characterize the charge carrier dynamics after photoexcitation. Chapter 2 offers the theoretical concepts of LHPs from the bulk to quantum confined NCs, strategies to mitigate their limitations, as well as advancements for optoelectronic applications. In Chapter 3, the chemical synthesis of NCs used in this study along with the optical characterization techniques, are presented. On the basis, Chapter 4 discusses the stable hydrogen evolution from polar vapor using $MAPbBr_3$ nanoplatelets (NPls), with an investigation of charge carrier transfer dynamics in the presence of Pt metal. Chapter 5 examines the charge carrier recombination mechanisms in $Cs_2AgBiCl_6$ NCs. Finally, a summary and outlook are provided in Chapter 6.

2

Fundamentals

This chapter highlights the fundamental physical concepts relevant to lead halide perovskite (LHP) nanocrystals (NCs) as used in this thesis. In Section 2.1, the development of LHP NCs for optoelectronic applications is introduced, including their basic physical properties and interactions with light. Lead-free bismuth-based double perovskites (DPs), which offer a solution to the high toxicity of LHPs, are discussed in Section 2.2. Finally, Section 2.3 focuses on the mechanism of photocatalytic hydrogen evolution, laying the theoretical foundation for Chapter 4. Various semiconductor NCs as light absorbers are introduced, and the advantages and challenges of LHPs in photocatalysis are addressed.

2.1 Lead Halide Perovskites

Deriving from inorganic perovskite oxides, halide perovskites with the generic chemical formula ABX_3 (where A represents Cs, methylammonium (MA), or formamidinium (FA) ions; B represents Pb or Sn ions; and X represents Cl, Br, or I ions) exhibit promising performance in photovoltaics, photodetectors, and LEDs, due to their tunable bandgaps and outstanding optoelectronic properties.[23–25] The rapid advancement of various applications based on halide perovskites has driven further investigation into their fundamental physicochemical properties. As the most extensively-studied perovskites, LHPs refer to a subcategory of halide perovskites in which Pb^{2+} ions occupy the B-site within a network of corner-sharing $[PbX_6]^{4-}$ octahedra.

In this section, I provide a brief overview of the development of LHPs in energy-related applications, and offer the fundamental physics underlying this unique material. In addition, the effect of quantum confinement on perovskite NCs is introduced, with a particular focus on two-dimensional NPls. This is followed by a discussion of the current challenges and potential solutions addressed in this thesis.

2.1.1 A Success Story

The first LHP was synthesized by Wells in 1892,[26] while the crystal structure of hybrid halide perovskites was characterized by Weber until the 1900s.[27,28] Since M. Era et al. applied them in an electroluminescent device in 1994[29] and Kagan et al. used them as semiconducting channels for field-effect transistors in 1999,[30] their potential for electronic and optical device applications has been increasingly recognized, attracting significant scientific interest.

In 2009, Kojima et al. demonstrated for the first time $MAPbI_3$ as a sensitizer in dye-sensitized solar cells with a power conversion efficiency of 3.8%.[7] Three years later, Lee et al. represented an evolution of perovskite-based solid-state sensitized solar cells, termed the meso-superstructured solar cell, which achieved a power-conversion-efficiency breakthrough of 10.9% under full solar illumination.[31] Since then, extensive studies on PSCs have emerged. Over the past 12 years, the efficiency of PSCs has been boosted dramatically from 3.8% to 25.0%,[8] pushing them to the forefront of the campaign for realizing next-generation economical photovoltaic and integrated technologies.

Alongside the development of PSCs, other optoelectronic applications based on LHPs have also flourished. The pioneering work on perovskite LEDs emerged in 1994,[29] followed by significant advancements since 2014, when Friend et al. designed perovskite LEDs based on $MAPbX_3$ thin films with an external quantum efficiency (EQE) below 1%.[32] Currently, green, red and near-infrared perovskite LEDs have achieved EQEs surpassing 20%,[33–35] with the highest EQE reaching up to 28.9% for green perovskite LEDs.[11] As ideal light emitters,

LHPs are promising candidates for LEDs to realize full-color displays with wide color gamut, high color purity, and high luminescence efficiencies. Moreover, LHPs have shown great potential in a broad range of technological applications including lasers,[36] photodetectors,[37,38] catalysts,[39] transistors,[40] memristors,[41] and artificial synapses.[42]

2.1.2 The Band Structure and Optical Properties

The Band Structure

The impressive optical and electronic properties of LHPs are a direct consequence of their band structure. LHPs are direct-bandgap semiconductors, with both the conduction band (CB) minimum and the valence band (VB) maximum located at the same point in k-space. Their energy bands are primarily dominated by the outer atomic orbitals of ^{82}Pb ([Xe]4f^{14}5d^{10}**6s**^{2}**6p**^{2}) and X (taking Br as an example: [Ar]3d^{10}**4s**^{2}**4p**^{5}), while the A-site cations participate only marginally in covalent bonding. Figure 2.1a illustrates the energy states of Pb 6s, Pb 6p, X *n*s, X *n*p orbitals and their hybridization states. Both the CB and the VB extrema are formed by anti-bonding states (σ^*) that originate from the hybridization of lead and halide orbitals. Specifically, the minimum of the CB is mainly composed of an antibonding state of Pb 6p and X *n*s orbitals, while the maximum of the VB band is characterized by a Pb 6s/X *n*p state.[43,44] In addition, the CB in LHPs exhibits overall p-character (orbital angular momentum $l = 1$), while the VB presents overall s-character ($l = 0$).

When taking into account spin-orbit coupling (SOC), the threefold degenerate CB of LHPs splits into a double-degenerate ($j = \frac{1}{2}$) and quadruple-degenerate ($j = \frac{3}{2}$) bands. The twofold degenerate band ($j = \frac{1}{2}$) is termed split-off band. It lies energetically below the fourfold degenerate bands, distanced by the split-off energy Δ_{SO}. In LHPs, the split-off band constitutes the CB minimum. Consequently, both the CB minimum and the VB maximum are two-fold degenerate. This behavior is atypical for traditional semiconductors such as II-VI and III-V compounds, where the VB maximum is usually p-like and four-fold degenerate, while the CB minimum is s-like and two-fold degenerate (Figure 2.1b). Moreover, the four-fold degenerate VBs in II-VI and III-V semiconductors consist of a light hole ($m_j = \pm\frac{1}{2}$) and a heavy hole ($m_j = \pm\frac{3}{2}$) band. In contrast, for LHPs, a light electron ($m_j = \pm\frac{1}{2}$) and a heavy electron ($m_j = \pm\frac{3}{2}$) band make up the four-fold degenerate CBs, as illustrated in Figure 2.1a.

Furthermore, the band structure determines the properties of photoinduced charge carriers. LHPs usually exhibit long carrier diffusion lengths and long carrier lifetimes. The orbital contributions of the bandedge states lead to a reduced spatial overlap of electron and hole wavefunctions, and hence decreased recombination rates.[45,46] Moreover, a weak preferential localization of electrons and holes in different regions of the perovskite unit cell may cause a reduction in the spatial overlap of electron and hole wave functions and hence recombination rates. These properties make LHPs well-suited for photovoltaic applications.

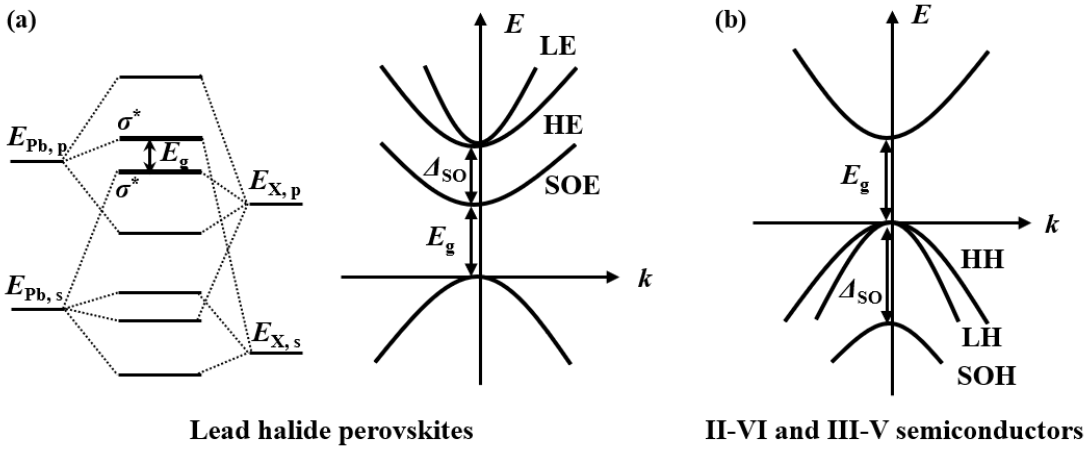

Figure 2.1: The Band Structures of LHPs and Conventional Semiconductors (a) Schematic energy-level diagram showing the hybridization of s and p orbitals from halide and lead atoms, and the resulting band structure of LHPs. The top of the VB band originates from a Pb 6s/X np antibonding state. Due to spin-orbit coupling (SOC), the CB bottom is formed by a spin-orbit electron (SOE) band, which is energetically separated from the four-fold degenerate light electron and heavy electron bands. Notably, both the CB bottom and the VB top in LHPs are derived from antibonding states. (b) Band structure of conventional II-VI and III-V compound semiconductors, which exhibit opposite bandedge characteristics compared to LHPs. In these materials, the CB minimum is s-like, while the VB maximum is p-like given by a heavy hole and a light hole dispersion along with a spin-orbit hole (SOH) band.

Extraordinarily, LHPs exhibit high defect tolerance, which is highly favorable for photovoltaics and other optoelectronic applications. In $MAPbI_3$, intrinsic point defects, such as MA_i^+ (i donates interstitials), V_{MA}^- (V donates vacancies), MA_{Pb}^-, V_{Pb}^{2-}, I_i^-, V_i^+, have low formation energies. They are calculated to lie approximately 0.05 eV above the VB maximum or below the CB minimum.[47] It has been reported that V_X^+ (halide vacancies) or V_A^- (A-site cation vacancies) as shallow defects are the dominant defects under X-poor or X-moderate/rich synthesis conditions, respectively.[48] Deep defects in LHPs have high formation energies, therefore their concentrations are quite low. This results in a high PL quantum yield because deep defects contribute to non-radiative recombination in LHPs, rather than shallow defects. In summary, most point defects in LHPs are shallow defects. It is attributed to the strong antibonding coupling of Pb s and X p orbitals, along with the high ionic character of LHPs. Shallow defects do not significantly perturb periodic crystal potentials, thereby enabling defect tolerance. Accordingly, solution-processed LHPs can sustain superior electronic properties in the presence of many intrinsic defects. This aligns with observations of long charge carrier diffusion lengths.

Optical Transitions

Having introduced the physical principles of electron and hole states in LHPs, I now turn to their interaction with electromagnetic waves. In the following text, LHP NCs without

quantum confinement are discussed first, followed by those exhibiting quantum confinement effects. Incident photons hit a LHP NC in its ground state. With a certain probability, electrons in the VB of the NC are excited into the CB along with the annihilation of the photons. Because of the law of energy conservation, the relation between absorbed photon energies, the ground state energies E_0 and the excited state energies E_1 is expressed as:

$$E_1 - E_0 = n \cdot \hbar\omega \tag{2.1}$$

where ω represents angular frequency. Such a optical transition process is called absorption of n photons. When $n = 1$, it is called linear absorption.

Besides energy conservation, momentum conservation needs to be satisfied during an optical transition. It is written as:

$$\hbar k_1 - \hbar k_0 = \hbar k \tag{2.2}$$

The wavevector of a photon, denoted by k, is given by $\frac{2\pi}{\lambda}$. This corresponds to values on the order of 10^7 m^{-1} for visible light excitation. In contrast, the crystal wavevector in the first Brillouin zone is associated with $\frac{\pi}{a}$ (a is the lattice constant) with the value order of 10^9 m^{-1} or 10^{10} m^{-1}, which is significantly larger than the wavevector of an absorbed photon from visible light. Therefore, the photon momentum change is neglected in Equation 2.2, which is simplified as: $\hbar k_1 = \hbar k_0$. Hence, optical transitions in direct semiconductors are commonly represented as "vertical" transitions in the energy dispersion diagram. For indirect-bandgap semiconductors, optical transitions happen with the help of phonons to fulfil the law of momentum conservation, which will be described in the next subsection.

The quantum mechanical transition rate $W_{0\to1}$, that an electron is excited from its ground state to an excited state by absorption of a photon with angular frequency ω, can be determined. Given by Fermi's golden rule, the transition rate is expressed as:

$$W_{0\to1} = \frac{2\pi}{\hbar}|M|^2 g(\hbar\omega) = \frac{2\pi}{\hbar}|\langle f|H'|i\rangle|^2 g(\hbar\omega) \tag{2.3}$$

Equation 2.3 shows that the dipole matrix element M and the density of states $g(\hbar\omega)$ are two factors influencing the transition rate. The dipole matrix element M describes the perturbation of electromagnetic waves on electrons, which is directly linked to the oscillator strength of respective optical transitions. H' is the perturbing Hamiltonian to describe the electric-dipole interaction, described by $-er \cdot \varepsilon$ where ε represents a perturbing electric field caused by the light wave. Based on the semi-classical approach and Bloch functions, the dipole matrix element M is simplified as:

$$|M| \propto \int_{\text{unit cell}} u_0(r) x u_1(r) \mathrm{d}^3 r \tag{2.4}$$

with the assumption that light is polarized along x axis of the unit cell. This matrix element M corresponds to the electric-dipole moment of transitions. Evaluating this quantity necessitates

knowledge of the envelope functions u_0 and u_1, which originate from atomic orbitals of constituent atoms. r is the position vector of electrons. As a result, the specific electronic structure of each material must be considered individually.

The factor of $g(\hbar\omega)$ in Equation 2.3 represents the joint density of states evaluated at the photon energy. The density of states describes the distribution of energy states within bands. In contrast, the joint density of states accounts for the availability of both ground and excited states within the CB and VB that are separated by the photon energy $\hbar\omega$. It effectively quantifies the number of possible electronic transitions at a given photon energy. For the simplified parabolic band structure shown in Figure 2.1a, the joint electron-hole density of states can be derived using the density of states equation for direct-bandgap semiconductors:

$$\begin{aligned} &\text{For } \hbar\omega < E_\mathrm{g}, \quad g(\hbar\omega) = 0; \\ &\text{For } \hbar\omega \geq E_\mathrm{g}, \quad g(\hbar\omega) = \frac{1}{2\pi^2}\left(\frac{2\mu}{\hbar^2}\right)^{3/2}(\hbar\omega - E_\mathrm{g})^{1/2} \end{aligned} \tag{2.5}$$

where μ is the reduced electron-hole mass: $\frac{1}{\mu} = \frac{1}{m_\mathrm{e}^*} + \frac{1}{m_\mathrm{h}^*}$ ($m_\mathrm{e}^*/m_\mathrm{h}^*$ represents the effective electron/hole mass). Based on Equation 2.3, the transition rate for a dipole-allowed interband transition is proportional to the joint density of states. The absorption coefficient α is proportional to the transition rate. Therefore, the absorption coefficient is expressed as:

$$\text{For } \hbar\nu \geq E_\mathrm{g}, \quad \alpha(\hbar\nu) \propto (\hbar\nu - E_\mathrm{g})^{1/2} \tag{2.6}$$

For direct-bandgap semiconductors, the bandgaps E_g are typically determined from the absorption onset. However, in some cases, the absorption spectra do not align well with the model. This discrepancy occurs when Coulomb interaction between electrons and holes is significant, or when defect states exist within the bandgap.

Excitons

The Coulomb interaction of electrons and holes can give rise to the formation of new energy states called excitonic energy states. A bound electron-hole pair is called an exciton, created when a photon is absorbed. The excitons introduce interesting optical properties, which are important for optoelectronic applications.

Bloch wavefunctions of free electrons and holes in a perfect crystal are delocalized, meaning that electrons/holes can move freely through the crystal lattice. The Coulomb interaction between electrons and holes perturbs the independent-particle Bloch picture. An exciton can move freely through the lattice, but the relative position of the electron and hole remains confined. The relative motion for excitons in real space leads to discrete eigenstates of the relative wavevector k, corresponding to excitonic states distinct from the continuum states of free electron-hole pairs.

Two types of excitons are observed in crystalline materials (Figure 2.2a): Wannier–Mott excitons and Frenkel excitons. Wannier–Mott excitons own a large radius spanning over many unit cells because of strong dielectric screening. They are delocalized states that can move throughout the crystal. They have small binding energies with typical values of around 0.01 eV. At room temperature, the collision with phonons of energy $k_B T$ can cause Wannier–Mott excitons to dissociate. In contrast, Frenkel excitons have a much smaller radius which is comparable to the size of a unit cell. They are tightly bound excitons confined to one molecule or atom and can hop from one atom site to another site. Frenkel excitons have larger binding energies of 0.1–1 eV, which makes them stable at room temperature.

A Wannier–Mott exciton is described in analogy to a hydrogen atom in a medium with a dielectric constant ϵ_r. In the Bohr model, discrete energetic states of excitons are separated from the continuum by binding energies. The binding energy E_B and the radius of the electron-hole orbit r characterized by the principle quantum number n are given as:

$$E_B(n) = -\frac{\mu}{m_0}\frac{1}{\epsilon_r^2}\frac{R_H}{n^2} = -\frac{R_X}{n^2} \tag{2.7}$$

$$r(n) = \frac{m_0}{\mu}\epsilon_r n^2 a_H = n^2 a_B \tag{2.8}$$

where R_H is the Rydberg energy of the hydrogen atom (13.6 eV). R_X is the exciton Rydberg energy. a_H is the Bohr radius of a hydrogen atom (5.29×10^{-11} m). a_B is the exciton Bohr

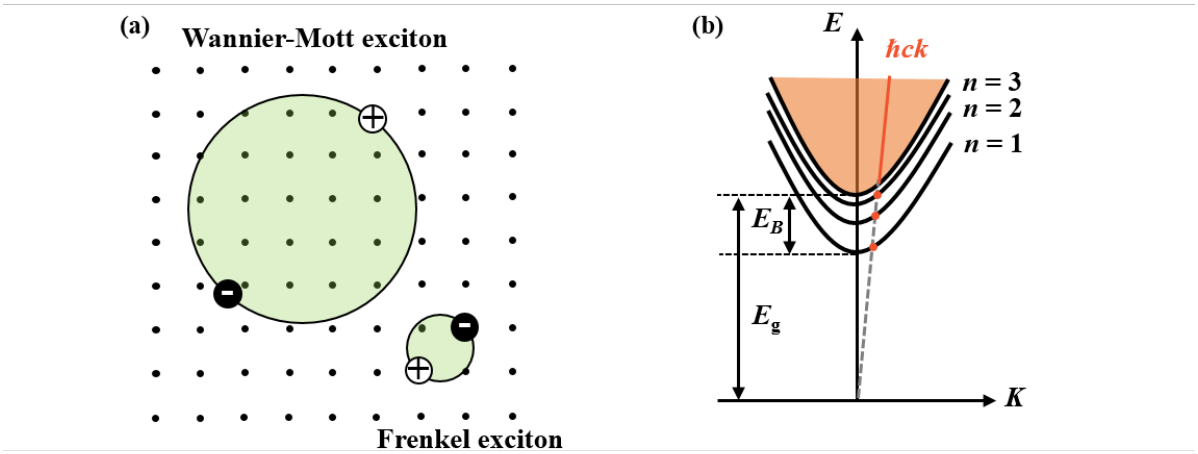

Figure 2.2: Excitons (a) Schematic diagram of a Wannier–Mott exciton and a Frenkel exciton within the crystal lattice. The Wannier–Mott exciton with a large radius and small binding energy can move freely through the unit cell, while the Frenkel exciton has a large binding energy and a small radius comparable to the unit cell, which can only hop from one atom site to another. (b) A two-particle picture of Wannier–Mott excitons. It shows the energy dispersion as a function of the exciton wave vector K. Discrete excitonic states with a parabolic dispersion are below the continuum of free electron-hole band states. At $K = 0$, excitonic states are isolated by their binding energies E_B. Optical transtions happen when the energy dispersion of excitons and the light dispersion overlap.

radius. m_0 is the free electron mass. Different from a one-particle picture showing the energy dispersion of free electrons/holes, a two-particle picture is introduced to visualize excitonic states of Wannier–Mott excitons. In Figure 2.2b, the excitonic energy dispersion with regard to the exciton wavevector $K = k_e + k_h$ is illustrated with a parabolic dispersion, given as:

$$E_n(K) = E_g - \frac{R_X}{n^2} + \frac{\hbar^2 K^2}{2(m_e^* + m_h^*)} \tag{2.9}$$

Moreover, optical transitions of excitons are displayed in the two-particle picture. Considering energy and momentum conservation, discrete excitonic states give rise to discontinuous absorption below the bandgap. In absorption spectra, it is represented by a series of individual absorption lines energetically below the absorption onset. In practice, these absorption lines are broadened into peaks due to homogeneous/inhomogeneous broadening. The Coulomb interaction between electrons and holes in excitons enhances their wavefunction overlap, resulting in an increased transition probability. Notably, the first excitonic peak is typically the most prominent, while the second and third excitonic peaks are sometimes indistinguishable because of the lower oscillator strength and the smaller energy separation from the continuum states, as well as between the excitonic states themselves.

Recombination

Subsequent to absorption, excitons in excited states return to their initial ground states radiatively or non-radiatively. Similar to the absorption process, energy and momentum conservation are fulfilled during recombination. An exciton recombines with a photon of a certain energy emitted, such spontaneous emission is called PL. In non-radiative recombination processes, the exciton energy is not transferred to photons. An exciton is sometimes trapped by a defect state and dissociates by generating heat. When excitons in the excited states have a high concentration, exciton-exciton annihilation may happen. In this process, an exciton transfers its energy non-radiatively to another exciton, promoting it to a higher energy state. For free charge carriers, this phenomenon is referred to as Auger recombination. Alternatively, an exciton or a charge carrier can transfer to other species in the vicinity, such as molecules or metal clusters, called energy or charge carrier transfer.

The recombination dynamics of excitons over time can be expressed by rate equations. The change in the density of excitons in the excited state with time $\frac{dn}{dt}$ is proportional to the exciton density $n(t)$, given as:

$$\frac{dn}{dt}(t) = -kn(t) = -(k_r + k_{nr})n(t) \tag{2.10}$$

where k indicates the recombination rate, which is the sum of the radiative recombination rate k_r and the nonradiative recombination rate k_{nr}. This applies to the monomolecular

recombination dynamics with only one excited state involved. In exciton-exciton annihilation, the variation of the exciton density scales with the squared exciton density $-k_{xx}n^2(t)$, given by a bimolecular model. In the thesis, exciton-exciton annihilation or Auger recombination are not considered. In actual experiments, the exciton density $n(t)$ is proportional to the PL intensity $I(t)$. Thus, a mono-exponential function as a function of time is obtained by solving the differential equation in Equation 2.10:

$$I(t) = I_0 e^{-(k_r+k_{nr})t} = I_0 e^{-t/\tau} \tag{2.11}$$

which represents the decay dynamics of excitons with an average lifetime of τ and an initial PL intensity I_0. The decay curve comprises both radiative and nonradiative recombination information without the contribution of exciton-exciton annihilation. Experimentally, PL decay could be monitored by time-resolved PL spectroscopy with different time scales, which I will describe in detail in Section 3.2.

2.1.3 Quantum Confinement

The optical properties of solids depend on the size when their dimensions are reduced to the nano-scale, as a consequence of the quantum confinement effect. The Heisenberg uncertainty principle indicates that quantum size effects will be important if a particle is confined to a region of x axis of length Δx, which is comparable to or smaller than the de Broglie wavelength $\lambda_{deB} \equiv h/p_x$ (p_x is the particle momentum along x) of the particle, as determined by its thermal motion. This applies to electrons or holes that are otherwise free. Alternatively, the quantum confinement effect matters when the crystal size gets close to the exciton Bohr diameter. Based on the degree of dimensionality with the quantum confinement effect, nanostructures are generally classified into quantum wells (one-dimensional confinement), quantum wires (two-dimensional confinement), and quantum dots (QDs) (three-dimensional confinement) (Figure 2.3).[49] In Chapter 4, I will investigate the optical properties of two-dimensional lead bromide perovskite NPls. Accordingly, fundamental physics of quantum wells will be introduced in the following.

The wave functions and the quantized states of electrons and holes in the conduction and valence bands of a quantum well can be calculated using Schrödinger's equation and the effective mass approximation. I talk about free electrons and holes as a start; the discussion of the quantum confinement effects of excitons will follow. By separating the free motion in the x, y plane and the quantized motion in the z direction, the total energy for an electron or hole in the nth quantum level is obtained:

$$E_{total}(n, \boldsymbol{k}) = E_n + \frac{\hbar^2 k^2}{2m^*} \tag{2.12}$$

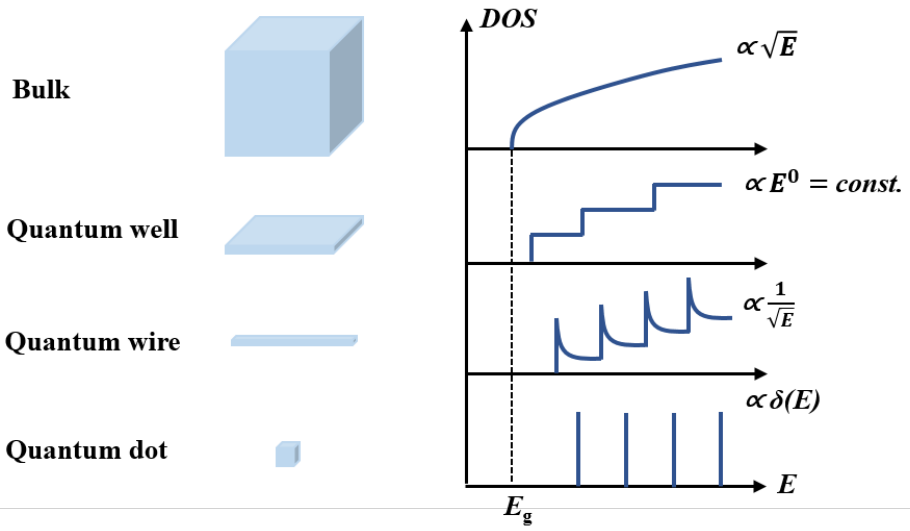

Figure 2.3: From Bulk to Lower Dimensional Semiconductors Schematic representation of bulk, quantum wells, wires, and dots. The generic shape of the density of states for electrons in the CB of a semiconductor with band gap E_g is shown for each type of structure.

with a wave vector $\boldsymbol{k}$ to specify the free motion in the x, y plane, and a quantum number n to indicate the energy level for the z direction. The calculation of the wave functions and energies for the quantized states in the z direction is determined by the spatial dependence of the conduction and valence bands, giving rise to infinite or finite potential wells.[50] In a model of infinite potential wells (Figure 2.4a), the eigenenergy E_n can then be calculated by solving Schrödinger's equation in (Equation 2.13) with $V(z) = 0$ $(0 \leq z \leq L)$ and with boundary conditions given by $\varphi(0) = \varphi(L) = 0$. The Schrödinger equation within the well is as follows:

$$H\varphi_n(z) = (-\frac{\hbar^2}{2m^*}\frac{\partial^2}{\partial x^2} + V(z))\varphi_n(z) = E_n\varphi_n(z) \tag{2.13}$$

with the solution:

$$\varphi_n(z) = A_n sin(\frac{n\pi z}{L}) \tag{2.14}$$

$$E_n = \frac{\pi^2\hbar^2}{2m^*L^2}n^2 \tag{2.15}$$

where L defines the thickness of the quantum well. The comparison of the quantization energies to the thermal energy k_BT offers insight into whether quantum effects are expected to be significant in a given quantum well at a particular temperature. From Equation 2.15, the energies of the quantized levels scale with the reciprocal of the effective mass and the inverse square of the well width. This indicates that low mass electrons/holes in narrow quantum wells own the highest energies.

Although the infinite well model is a useful starting point for the discussion of quantum-well physics because of its simplicity, it overestimates the confinement energies. Perovskite

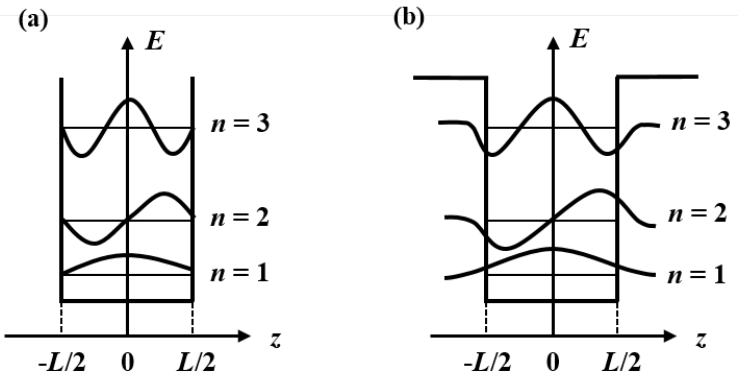

Figure 2.4: Infinite and Finite Potential Wells (a) The Schematic diagram shows an infinite one-dimensional potential well of width L with the first three energy levels and corresponding wave functions included. (b) A finite potential well of width *L*. The wave functions spread into the barrier regions by tunneling, consequently reducing the quantum confinement energy relative to a well with infinite barriers.

NPls discussed in the thesis are surrounded by ligands, which create finite potential barriers rather than infinite vacuum barriers. The finite potential discontinuity enables charge carriers to tunnel into the barriers to some extent, allowing the extension of their wavefunctions and reducing the confinement energy compared to a well with infinite barriers (Figure 2.4b). In addition, LHP NPls with different monolayers tend to stack with each other. In this case, a quantum well superlattice may form with the combination of multiple quantum wells from different perovskite NPls separated by ligands as barriers. For the superlattice, the wavefunctions of charge carriers in each quantum well can spread outside by tunnelling and hybridize with neighboring platelets. The electronic coupling results in the formation of minibands, reducing the absorption onset energies.

The optical transitions in a quantum well can be understood by applying the selection rules and density of states, which will be described as follows. As shown in Equation 2.3, the transition rate is determined by the joint density of states and the squared electric-dipole matrix element. Meanwhile, the matrix element M is given by Equation 2.6. On substituting the initial and final quantum well wave functions, the matrix element M breaks into two parts:

$$M = M_{\mathrm{CV}} M_{\mathrm{eh}} \tag{2.16}$$

where M_{CV} is the valence–conduction band dipole moment. It is intrinsic for a specific material and non-zero. M_{eh} represents the electron-hole overlap, which is non-zero only when the quantum number n of electron and hole states are the same for an infinite quantum well. It indicates that optical transitions are allowed only when the selection rule $\Delta n = 0$ is obeyed for an infinite quantum well. In finite quantum wells, electron and hole wave functions with different quantum numbers have a small overlap. However, their corresponding optical transitions are quite weak.

Given by the selection rules, optical transitions start with a threshold of photon energy based on Equation 2.12: $E = E_g + E_{1,e} + E_{1,h}$. It indicates that the absorption onset of a quantum well is shifted to the high energy side by $(E_{1,e} + E_{1,h})$ compared to that of the bulk semiconductor. Moreover, the confinement energy is determined by the quantum well width L. Derived from Equation 2.12 and Equation 2.13, the E–k_{xy} diagram shows parabolic dispersions for $\Delta n = 0$ transitions:

$$E = E_g + E_{n,e} + E_{n,h} + \frac{\hbar^2 k_{xy}^2}{2\mu} = E_g + \frac{\pi^2 \hbar^2}{2\mu L^2} n^2 + \frac{\hbar^2 k_{xy}^2}{2\mu} \tag{2.17}$$

In contrast to the bulk semiconductor, the density of states for the two-dimensional material is:

$$g_{2D}(E) = \frac{\mu}{\pi \hbar^2} \tag{2.18}$$

It decides that the absorption coefficient of a quantum well exhibits a step-like structure (Figure 2.3). A new step shows up at the energy of $(E_g + E_{n,e} + E_{n,h})$ for individual $\Delta n = 0$ transitions.

The effects of one-dimensional quantum confinement affect excitons as well as unbound carriers. From a bulk semiconductor to a confined regime, the mutual Coulomb attraction of an electron and a hole in an exciton increases greatly together with an enhanced exciton binding energy E_B^{2D} (Figure 2.5). On the one hand, the spatial limitation forces electrons and holes to be closer together. The reduction from three-dimension to two-dimension geometry enhances the exciton binding energy E_B^{2D} by a factor of four, without the consideration of dielectric effects.[51] On the other hand, the electric field extends outside of NPls into the surroundings, which possess a significantly smaller dielectric constant than within the crystals. This leads to a weaker dielectric screening of the electric field, and thus the overall stronger Coulomb interaction. With a larger exciton binding energy, excitons that dissociate in bulk could be stable in quantum wells at room temperature. Excitonic effects in quantum wells enhances their optical transition rates. Moreover, the transition energy of excitons is expressed based on Equation 2.17:

$$E_{exciton} = E_g + E_{1,e} + E_{1,h} - E_B^{2D} = E_g + \frac{\pi^2 \hbar^2}{2\mu L^2} - E_B^{2D} \tag{2.19}$$

In addition, there are two regimes of quantum confinement determined by the relation of the nanostructure length L and the exciton Bohr diameter a_B. In a weak confinement regime, when L is larger than a_B, electrons and holes are considered to move coherently as a hydrogen-like exciton. The exciton binding energy is calculated using the effective mass approximation. When $L < a_B$, the strong confinement regime dominates, where electron and

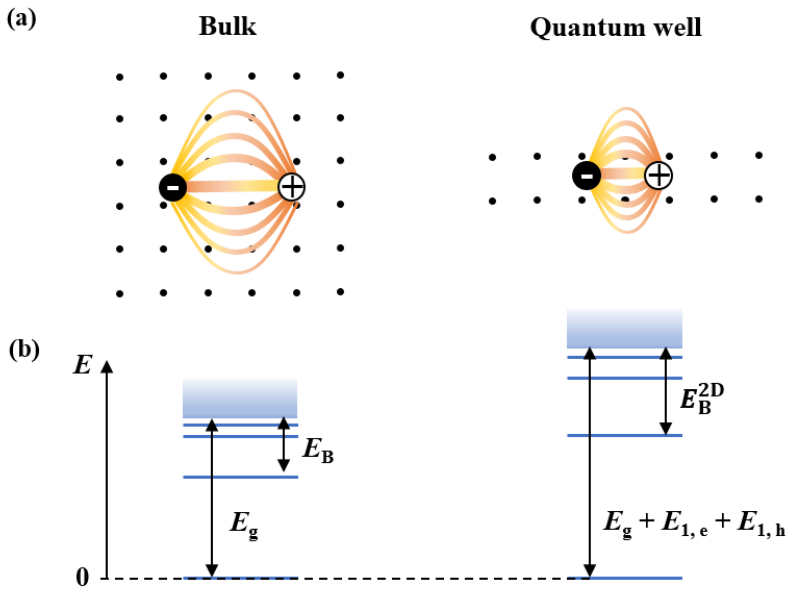

Figure 2.5: The Quantum Confinement Effect in a Quantum Well (a) Schematic diagram of an exciton in bulk and in a quantum well. In a quantum well, the electric field of the exciton extends beyond the platelet. Thus, the dielectric screening of the Coulomb interaction is not as strong as that within the bulk counterpart. (b) From bulk to a two dimensional quantum well leads to an increase in the continuum onset ($E_g + E_{1,e} + E_{1,h}$) and a larger exciton binding energy E_B^{2D}.

hole are regarded as individual particles. Therefore, the exciton binding energy is calculated differently.[52]

Layered LHPs were reported for the first time in the late 1980s.[53] In recent years, two-dimensional NPls with quasi-two-dimensional characteristics have received much attention with the prosperous development of perovskites in photovoltaics, as well as characterization techniques to probe two-dementional nanostructures. Particularly, two-dimensional NPls have been demonstrated with atomic-precision control over their thickness down to a single monolayer and large exciton binding energies, an attractive feature for light-emitting devices. In 2015, Sichert et al. obtained $MAPbBr_3$ NPls with thickness from a single monolayer to five monolayers by tuning the ratio of the organic cations.[54] In 2018, Bohn et al. presented a facile synthetic approach for two-dimensional $CsPbBr_3$ NPls of only one specific thickness ranging from 2 to 6 monolayers, leading to sharp photoluminescence.[55] It is shown that the reduction of the monolayer numbers results in an increase of the continuum absorption onset given by Equation 2.17 at $k = 0$. The exciton binding energy increases simultaneously. The shift of the continuum absorption onset is usually larger than the increase of exciton binding energy, ensuring an overall blueshift of excitonic resonance.

Furthermore, the increased overlap between electron and hole wave functions in quantum confinement regimes enhances the emission probability and shortens radiative recombination lifetime. Additionally, the discrete nature of the density of states reduces the thermal distribu-

tion of carriers within their bands. As a result, the emission efficiency may be improved in LHP NCs with the confinement effect, facilitating the development of bright light-emitting devices.

As the degree of quantum confinement increases, quantum wire and QD structures are formed. Two-dimensional and three-dimensional confinement bring out more interesting optical properties and their density of states varies greatly (Figure 2.3). In a QD, electron and hole states are completely quantized. Theoretically, its absorption spectrum consists of a series of discrete lines. However, individual transitions in traditional semiconductors are difficult to distinguish due to low confinement energies originating from heavy excitons (a large effective hole mass). LHP QDs are intrinsically advantageous at this point. The inverted band structure of LHPs leads to light excitons and thus large confinement energies. This makes individual transitions in perovskite QDs easier to distinguish compared to conventional semiconductors.

In practice, inhomogeneous broadening in perovskite QD ensembles limits the resolvability of individual transitions. Precise control over the size of QDs with a narrow size distribution is highly desirable. Significant efforts have been devoted to reducing the size deviation of LHP QDs below 5% and progress has been made with $CsPbX_3$ (X = Cl, Br, or I).[56,57] More recently, a novel synthetic strategy—based on the separation of nucleation and growth—has enabled the production of highly monodisperse, spherical LHP QDs with finely tunable sizes in the sub–10 nm range.[9] Later, Barfüßer et al.[10] reported the clear observation of several distinct confined excitonic transitions of monodisperse spherical-like $CsPbBr_3$ QDs.

2.1.4 Problems and Limitations

Instability

Despite the exceptional performance of LHPs in photovoltaics, their susceptibility to ambient factors, such as humidity, oxygen, light and heat, gives rise to the well-recognized stability issue and deteriorates device performance.[16,17] Among these factors, humidity has been demonstrated as the most aggressive cause of instability in materials and devices due to the formation of the intermediate hydrated perovskite phases such as from $CH_3NH_3PbI_3$ to $CH_3NH_3PbI_3{\cdot}H_2O$ and $(CH_3NH_3)_4PbI_6{\cdot}2H_2O$, which subsequently decompose into solid-state PbI_2 and volatile gases (e.g., HI and CH_3NH_2). On the other hand, it is reported that a meticulous amount of moisture has a positive effect on photovoltaic performance.[58] Hence, the manupulation of the ambient environment is vital for their device efficiencies. By careful operation, superior performance of perovskite photovoltaic devices can be achieved.

However, the water-instability issue devastatingly limits their deployment in water-mediated applications, such as photocatalytic hydrogen evolution and electrocatalysis. LHPs degrades fast in aqueous solution, as well as in polar solvents such as methanol, ethanol. It is a great regret especially for photocatalysis, as LHPs with extrodinary optoelectric properties and defect tolerance are promising photocatalyst candidates.[59] Currently, several strategies have been developed to address the issue. Encapsulation is a straightforward way to improve the stability of LHPs by coating NCs with a robust and inert shell.[60] It has been demonstrated that the stability of LHPs is successfully improved by the encapsulation of SiO_2,[61,62] TiO_2,[63] Al_2O_3,[64] or polyhedral oligomeric silsesquioxane.[65] However, NCs after post synthesis tend to aggregate within one shell. Moreover, the existence of the shell limits the mass transfer of inner cores, such as proton adsorption and reactant desorption for photocatalytic reactions, which leads to low activities. Another solution is to employ hydrohalic acid solutions (such as HBr, HI) for halide perovskite catalysis. However, this method is undesirable due to its environmental unfriendliness and high transportation cost. Long-term exposure to halo acids still leads to phase segregation, defect formation, and irreversible decomposition.

Based on the principles of physical chemistry, the interaction between LHPs NCs and water molecules is strongly related to the amount of water or the molar ratio of water to perovskites.[66,67] As the number of water molecules increases, the reactions proceed through different stages, including hydration, phase transformation, decomposition, and dissolution. In some cases, the hydration process for the rapid formation of hydrogen bonds between water and organic cations is reversible when water is removed from the system.[15] Inspired by this, it is believed that LHPs NCs could survive in the atmosphere of water if the water molecule concentration is controlled within a specific range.

In my thesis, conversion from an aqueous solution to a water-steam system is proposed for LHPs in photocatalytic hydrogen evolution. To be specific, 1 mL of water (or methanol)

contains 55.6 (or 24.7) mmol of water (or methanol) molecules, driving LHPs NCs to decompose abruptly. However, the concentration of water (or methanol) in their vapor phase (g) is 1.28 μmol/mL (or 6.79 μmol/mL) at room temperature. Such a dilute atmosphere of polar molecules alleviates the intensive interaction of LHPs NCs with water molecules, which prevents their decomposition and dissolution. In addition, the surface-adsorbed water (methanol) molecules are timely consumed as a proton source in reactions. Eventually, the adsorption and desorption process will reach an equilibrium in a constant system. In this case, I anticipate that the ionic structure of LHPs can be stable in polar environments, such as vapor of, e.g., water and methanol, and steadily generate hydrogen under solar light illumination. The idea will be presented in detail in Chapter 4.

Toxicity

Besides water solubility, the presence of lead (Pb) in LHPs raises significant environmental and health concerns. Particularly, possible lead leaching during material degradation and disposal can lead to bioaccumulation and toxicity.[68] These concerns have prompted the search for less toxic, environmentally benign alternatives that retain the desirable properties of lead-based perovskites.

In light of the toxicity associated with lead, replacing lead ions with other metal cations possessing similar electronic configurations presents a promising alternative. Homovalent ions are firstly considered. Tin (Sn) and germanium (Ge), which belong to the same group in the periodic table as lead, have been identified as potential substitutes. However, Tin- and germanium-based LHPs exhibit reduced structural stability compared to their lead-based counterparts as the +2 valence states of Sn and Ge are easily oxidized into their +4 valence states.[69] In addition, a variety of metal cations with stable divalent valence states—such as Ca^{2+}, Pd^{2+}, Cd^{2+}, Hg^{2+}, Ba^{2+}, Be^{2+}, Pt^{2+}, Ni^{2+}, Co^{2+}, Zn^{2+}, Mn^{2+}, Fe^{2+}, and Sr^{2+}—have been explored as lead substitutes.[70] However, some metal ions are not environmentally friendly (Cd^{2+}, Hg^{2+}) or not suitable for photovoltaic applications because of their high band gap (Be^{2+}, Ca^{2+}, Ba^{2+}, Sr^{2+}).[71] Taking these factors into account, cobalt (Co), nickel (Ni), manganese (Mn), and zinc (Zn) among divalent ions emerge as the most promising candidates for the development of environmentally friendly lead-free perovskite materials. Nevertheless, synthesis of these metal ions-based perovskite NCs in ABX_3 format is still challenging.[72] The heterovalent substitution of lead in perovskites can give rise to a variety of structural dimensionalities, and new optical properties. Lead can be replaced by tetravalent metal cations (B^{4+}), such as Sn^{4+} and Pd^{4+}, resulting in the formation of A_2BX_6-type perovskites.[73] Additionally, trivalent metal cations like Bi^{3+} and Sb^{3+} can substitute for three lead ions to produce layered $A_3B_2X_9$ compounds.[74]

Recently, lead-free double perovskites have gained significant attention with a general formula of $A_2BB'X_6$, where two trivalent (Bi^{3+}, In^{3+}, Sb^{3+}) and monovalent cations (Ag^{+},

Cu^+) replace two divalent lead cations, resulting in a stable and less toxic structure. This heterovalent substitution maintains overall charge neutrality within the perovskite lattice. Among DPs, bismuth (Bi)-based double perovskites—such as $Cs_2AgBiCl_6$—stand out for their excellent stability under ambient conditions and promising optoelectronic properties, making them strong candidates for next-generation optoelectronic applications..[8,75] In 2016, Slavney et al. reported a $Cs_2AgBiCl_6$ single crystal with long carrier recombination lifetime of ca. 660 ns.[20] In 2021, Wright et al. observed rapid decays in optical-pump-terahertz probe transients, which are attributed to small polarons.[76]

Despite their promise, the photophysical behavior and underlying electronic structure of Bi-based double perovskites are not yet fully understood. Their optical absorption spectra often show indirect band gaps and complex excitonic features, which are not straightforward to interpret using conventional models. Additionally, intrinsic defects, sub-bandgap states, and strong spin–orbit coupling contribute to the complexity of their spectral signatures. These unresolved questions hinder the precise tuning of material properties for targeted applications. Therefore, further experimental and theoretical investigations are necessary to elucidate the origin of their optical transitions and to optimize their performance in next-generation optoelectronic devices. In Chapter 5, I will demonstrate that silver (Ag) plays a role in the emission of $Cs_2AgBiCl_6$ NCs.

In the following two subsections, I will discuss the current state of research on bismuth-based DPs (Section 2.2) and the fundamental principles of photocatalytic hydrogen evolution (Section 2.3), providing the necessary background to support the understanding of my experiments.

2.2 Bismuth-Based Double Perovskites

2.2.1 An Overview of Bismuth-Based Double Perovskites

Given the high toxicity of lead, bismuth—an environmentally benign heavy metal with a similar ionic radius and electronic configuration—offers a viable pathway to mimic some of the advantageous features of Pb-based perovskites while improving environmental safety. Bismuth-based hybrid halides, such as $MA_3Bi_2I_9$ and $(NH_4)_3Bi_2I_9$, have been reported to possess two-dimensional structures; however, they exhibit low electrical conductivity.[77,78] To accommodate trivalent Bi^{3+} into a three-dimensional (3D) perovskite structure, a combination with a monovalent cation is necessary to form DPs with the formula of A_2BBiX_6.[71]

The name "DPs" refers to the ordering of two distinct B-site cations, effectively doubling the B-site sublattice within the perovskite structure. Radius-ratio rules guide the selection of monovalent cations with appropriate sizes to stabilize octahedral halide coordination in bismuth-based DP structures. To date, various monovalent cations—including potassium (K^+), sodium (Na^+), silver (Ag^+), thallium (Tl^+), copper (Cu^+), gold (Au^+), as well as organic cations—have been explored in combination with bismuth within DP frameworks both experimentally and theoretically.[79,80] While the first bismuth-based halide DPs were proposed as potential photovoltaic absorbers in 2016,[20] related compounds have long been known as "elpasolites"—a name derived from the mineral K_2NaAlF_6. An article in 1982 summarized that at least 210 halide elpasolites with either cubic and/or tetrahedral structures had already been identified, including bismuth-containing composites.[81] However, these composites, such as $Cs_2NaBiCl_6$, drew interest at that time due to their potential for ferromagnetic phase transition.[82] In 2016, Slavney et al.[20] investigated the optical properties of $Cs_2AgBiCl_6$ single crystals, followed shortly thereafter by McClure et al.,[83] who described the band structure of Cs_2AgBiX_6 (X = Cl, Br). These highlighted their potential for photovoltaic applications. The first hybrid inorganic–organic DP, MA_2KBiCl_6, was crystallized by Wei et al. via a hydrothermal technique.[84] Subsequently, they introduced silver cations to synthesize $MA_2AgBiCl_6$, which exhibited a small band gap of 2.02 eV and good environmental stability.[85]

Among the family of bismuth-based DPs, Cs_2AgBiX_6 has emerged as the most extensively studied compound. This prominence is largely attributed to its intriguing optoelectronic properties related to its indirect bandgap, calculated to be 2.06 eV for $Cs_2AgBiBr_6$ and 2.62 eV for $Cs_2AgBiCl_6$.[83] At present, large single crystals, NCs, and thin films of Cs_2AgBiX_6 have been fabricated.[86] In addition to its optical properties, Cs_2AgBiX_6 demonstrates exceptional thermal and environmental stability across different morphologies, with strong resistance to heat, moisture, and oxygen. These attributes make it a promising candidate for lead-free and durable photovoltaic and optoelectronic devices.

Both theoretical and experimental investigations have been performed to gain insight into its electronic band structure, carrier effective masses, defect tolerance, and excitonic behavior of Cs_2AgBiX_6.[21,76,83,87] These studies have provided critical understanding of its limitations and potential in energy conversion and optoelectronic applications. In the following sections, I will describe the band structure and optical properties of Cs_2AgBiX_6 DPs.

2.2.2 The Band Structure of Cs_2AgBiX_6 Double Perovskites

Optical measurements and electronic structure calculations suggest that Cs_2AgBiX_6 exhibits an indirect bandgap due to the hybridization of frontier orbitals from Ag and Bi. Take $Cs_2AgBiCl_6$ as an example, its electronic band structure is depicted in Figure 2.6 based on literature.[70,83] Notably, the dispersion characteristics of the CB and VB are anisotropic at the X point of the Brillouin zone. The CB is relatively flat along the X–W direction with a minor curvature toward the Γ point. In contrast, the CB shows a strong dispersion along the X–Γ direction, which results in a low hole effective mass. Studies have revealed that the effective electron mass along the L–W direction for $Cs_2AgBiCl_6$ is approximately $0.53m_0$, and the effective hole mass along the X–Γ direction is about $0.15m_0$, assuming a parabolic band approximation.[83,88] In contrast, $CsPbCl_3$ shows an effective electron mass of $0.41m_0$, and an effective hole mass along the same direction is $0.35m_0$. While these values are given qualitatively without accounting for carrier scattering rates, it is encouraging that the estimated effective hole masses for DPs are lower than their lead counterparts.

It is noted that the degenerate states at the Γ-point in the CB are split when SOC is considered. This results in the formation of a narrow, heavy electron band that is energetically

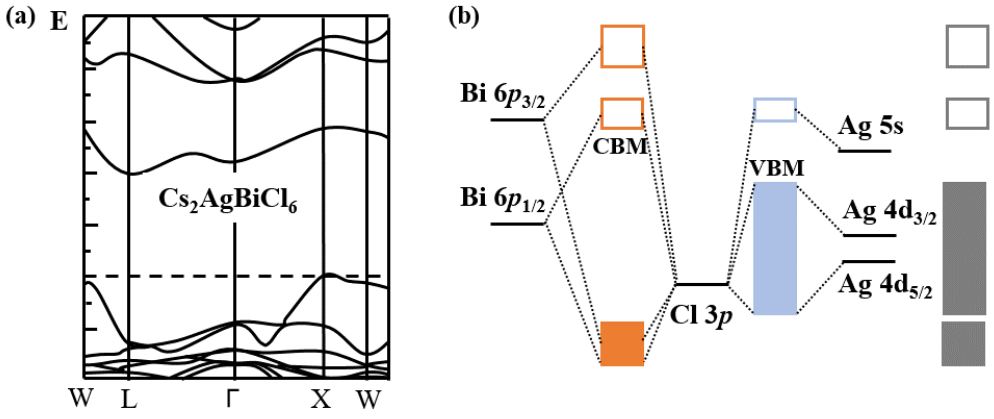

Figure 2.6: The Electronic Band Structure of $Cs_2AgBiCl_6$ (a) Electronic band structure of bulk $Cs_2AgBiCl_6$. (b) The molecular orbital diagram of $Cs_2AgBiCl_6$. The atomic energy levels are indicated by black lines. Orange rectangles represent the Bi-Cl hybrid bands, while light blue rectangles denote the Ag-Cl hybrid bands. The grey rectangles correspond to simplified energy bands of $Cs_2AgBiCl_6$.

isolated by approximately 1 to 1.5 eV from the next higher CBs. This isolated CB originates primarily from the splitting of Bi $p_1/_2$ and Bi $p_3/_2$ states. The CB minimum is composed mainly of Bi p and halogen p antibonding states. The VB maximum is dominated by hybridized Ag 4d and halogen p orbitals. The Ag 4d orbitals significantly influence the electronic structure by lowering the band gap and contributing to the indirect transition observed in these DPs. Additionally, a minor Bi s/halogen p antibonding contribution appears near the top of the VB.

The quaternary composition of Bismuth-based DPs brings out more intrinsic point defects compared to LHPs. It has been demonstrated that the trap density in the bulk of Cs_2AgBiX_6 is in the order of 10^{16} cm^{-3}, which is approximately three orders of magnitude higher than the values reported for lead-based perovskite single crystals.[89,90] Figure 2.7 shows various intrinsic defects and their calculated transition levels. These intrinsic defects modify the electric band structure via introducing transition levels, which strongly affect carrier density and transport. Vacancies are typically significant in halide perovskites due to their low formation energies. In contrast, metal interstitials generally exhibit high formation energies, unless the metal ion exists in a low oxidation state, such as +1.[91] In DPs, antisite defects arising from cation disorder between the B and B' sites are prevalent, because of the similar octahedral environment for both sites. T. Li et al. employed density-functional theory to investigate the defect landscape of $Cs_2AgBiCl_6$, providing insights into its intrinsic defect chemistry.[92] The study indicates that the silver vacancy V_{Ag}^{-} is the most important acceptor defect whereas the halogen vacancy V_{Cl}^{+}, the antisite defect Bi_{Ag}^{2+}, and the interstitial Ag_i^{+} are primary donor defects in $Cs_2AgBiCl_6$.[92]

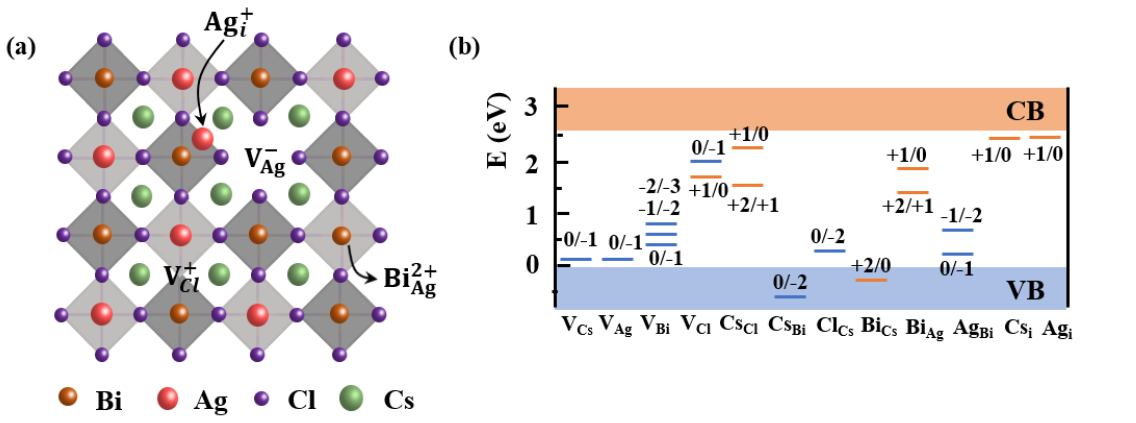

Figure 2.7: Intrinsic defects in $Cs_2AgBiCl_6$ (a) Several dominant intrinsic defects in the $Cs_2AgBiCl_6$ crystal lattice include V_{Ag}^{-}, Ag_i^{+}, V_X^{+}, and Bi_{Ag}^{2+}. (b) The energy diagram illustrates the transition levels of various intrinsic defects in $Cs_2AgBiCl_6$. Blue levels represent acceptor defects, while orange levels indicate donor defects. For each defect, the transition levels vary based on transitions between different charge states (e.g., 0/-1, -1/-2).

2.2.3 Optical Properties of Cs_2AgBiX_6 Double Perovskites

Owing to the indirect bandgap nature, the charge carrier lifetime of Cs_2AgBiX_6 can reach the microsecond range. In 2016, Slavney et al. demonstrated PL in $Cs_2AgBiCl_6$ single crystals with an average lifetime of approximately 660 ns at room temperature, which is very promising for photovoltaic applications.[20] In the following year, Greul et al. reported the first $Cs_2AgBiBr_6$ solar cell, with power conversion efficiencies close to 2.5%.[93] In 2018, Hoye et al. observed a mono-exponential photocarrier decay with a lifetime of 1.4 µs.[21] However, concerns remain regarding their indirect band gaps, which inherently limits optical absorption and thus photovoltaic performance. It was predicted that the spectroscopic limited maximum efficiency of Cs_2AgBiX_6 solar cells is below 10% for both bromides and chlorides, taking into account the optical absorption strength and the bandgap nature in the overall theoretical efficiency of an absorber material.[94,95]

Nevertheless, it has been shown that alloyed Cs_2AgBiX_6 is of particular interest for single-emitter-based white-light-emitting phosphors and diodes for next-generation lighting and display technologies. Although pure Cs_2AgBiX_6 exhibits a low PL quantum yield, its luminous properties can be remarkably enhanced by alloying/doping with alkali metal ions,[96] transition metal ions,[97] or rare earth metal ions.[98] Luo et al. reported that $Cs_2(Ag_{0.6}Na_{0.4})(In_{0.96}Bi_{0.04})Cl_6$ emitted warm-white light with 86 ± 5% quantum efficiency for over 1,000 hours.[22] Moreover, DPs have demonstrated a strong potential for X-ray and UV detectors.[99]

Despite these promising developments, a deep understanding of the fundamental photophysical processes in Cs_2AgBiX_6 remains essential. Studies have shown that both bulk and NCs of Cs_2AgBiX_6 exhibit an exceptionally broad PL spectrum centered around 650 nm.[22] However, the origin of the red emission remains a topic of ongoing debate. Multiple mechanisms have been proposed, including the involvement of self-trapped excitons,[76,100] color centers,[101] and defect-bound excitons,[88] with each offering a distinct interpretation of the observed spectral features. Wright et al. discovered rapid decay features in optical pump–terahertz probe measurements, attributing the broad and strongly red-shifted PL of $Cs_2AgBiBr_6$ to the diffusion of self-trapped charge carriers into color centers.[76] Zelewski et al. demonstrated that the PL of $Cs_2AgBiBr_6$ originates from color centers rather than band-to-band transitions, and explained it using a Franck–Condon model.[101] Several studies have investigated the influence of intrinsic defects on charge carrier dynamics in Cs_2AgBiX_6.[89,102] For example, Bartesaghi et al. attributed the rapid depletion of photoexcited charges to surface recombination, while the prolonged decay over several microseconds was ascribed to trap-assisted recombination within the bulk.[89] Further investigation is required to provide a clearer picture of charge recombination processes in Cs_2AgBiX_6, which is also crucial for optimizing its performance in a variety of optoelectronic applications.

In my thesis, $Cs_2AgBiCl_6$ colloidal NCs show dual-peak PL, characterized by a spectrally broad red emission centered around 650 nm and a narrower blue emission band centered at 425 nm (Figure 5.1d). In Chapter 5, I will systematically discuss the origin and nature of these two distinct PL bands through a step-by-step physical interpretation, supported by a theoretical model.

2.3 Photocatalytic H_2 Evolution with Pt-Decorated Semiconductors

As introduced in Subsection 2.1.4, a vapor-based strategy is proposed to mitigate the solution (polar solvent)-induced degradation of LHPs in catalysis. Building upon this concept, Chapter 5 will explore the use of the solid–vapor interface for photocatalytic hydrogen evolution, offering a novel pathway for improving the performance and durability of perovskite-based systems under aqueous conditions. To establish a comprehensive understanding, the fundamental mechanisms of hydrogen generation are first introduced in Subsection 2.3.1, with a focus on key reaction steps, electron transfer processes, and relevant thermodynamic considerations. Following this, Subsection 2.3.2 reviews recent advances in the development of colloidal NCs for photoinduced hydrogen evolution. Finally, Subsection 2.3.3 is dedicated to a critical discussion of the current state of LHPs in this field. The section aims to provide a cohesive framework for understanding the role of LHPs in photocatalytic hydrogen production and highlight ongoing challenges and opportunities for future research.

2.3.1 Principles of Photocatalytic H_2 Evolution

Hydrogen offers a clean and sustainable energy solution with high energy capacity and zero carbon emissions at the point of use. It can be produced via photo- or electro-catalysis—environmentally friendly approaches that utilize renewable solar light or low-cost electricity, to drive water splitting reactions on semiconductor surfaces. The first example of photo/electrocatalytic H_2 production was reported by Fujishima and Honda in 1972.[103] A photoelectrochemical cell was employed with oxygen evolution at the TiO_2 electrode and hydrogen evolution at the platinum black electrode. Later, Bard extended this concept to develop a purely photoinduced reaction system based on semiconductors.[104]

Photocatalysis refers to a series of photoinduced catalytic reactions with the participation of solar light, semiconductors, and reactants. As discussed in Section 2.2, when a semiconductor absorbs a photon with energy equal to or greater than its bandgap, an electron is excited into the CB leaving a hole in the VB. It creates a free electron–hole pair or an exciton, which may recombine rapidly with the emission of a photon. However, some of them diffuse within the crystal and reach the semiconductor surface. At surface sites, these charge carriers can initiate redox reactions with molecules absorbed on the photocatalyst surface. Specifically, an excited electron can reduce an oxidant, while a hole can oxidize a reductant. Take water as an example, a H_2O molecule can be oxidized to O_2 or reduced to H_2 through separate half-reactions:

$$H_2O + 2h^+ \rightarrow \frac{1}{2}O_2 + 2H^+, \quad E_{ox} = -1.23\ \text{eV} \tag{2.20}$$

$$2H^+ + 2e^- \rightarrow H_2, \quad E_{red} = 0 \text{ eV} \tag{2.21}$$

The reduction and oxidation reactions occurring on the photocatalyst surface form the fundamental basis of photocatalytic processes. By combining the half-reactions discussed in Equation 2.20 and Equation 2.21, the overall reaction for water splitting can be written as follows:

$$H_2O \rightarrow \frac{1}{2}O_2 + H_2, \quad \Delta G = +237 \text{ kJ/mol} \tag{2.22}$$

This process is known as photocatalytic full water splitting, and a schematic representation is provided in Figure 2.8. Water splitting into H_2 and O_2 is a thermodynamically uphill reaction. In this reaction, solar energy absorbed by the semiconductor–analogous to the role of sunlight in plant photosynthesis–is stored in chemical bonds in the form of energy-rich products. The standard Gibbs free energy increase ΔG for this reaction is +237 kJ/mol (or 1.23 eV). As a result, the bandgap energy of photocatalysts must exceed 1.23 eV (< 1000 nm) to achieve full water splitting. Moreover, for both oxidation and reduction to be thermodynamically feasible on a single photocatalyst, its band extrema must straddle the oxidation and the reduction potentials. It means that the CB must be more negative than the reduction potential of H^+/H_2, and the VB must be more positive than the oxidation potential of H_2O/O_2.

However, more energy than the Gibbs free energy change (ΔG) is required to overcome the activation energy (E_a) for redox reactions on the photocatalyst surface (Figure 2.8c). In the Arrhenius model, the activation energy (E_a) defines the minimum energy required for a chemical reaction to occur. Suitable cocatalysts are able to lower the activation energy by

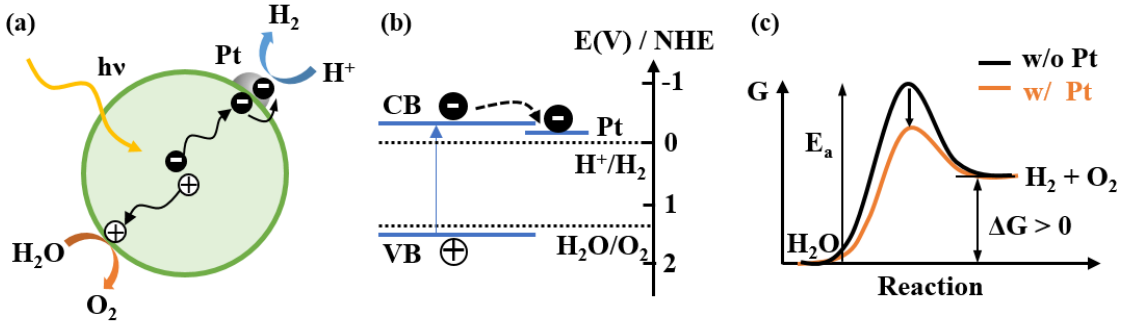

Figure 2.8: Full Water Splitting with Pt-Decorated Semiconductors (a) Schematic showing the principle of photocatalytic overall water splitting with Pt-decorated semiconductors. Photoexcited charge carriers diffuse to the semiconductor surface. On the surface, a photoexcited electron is trapped by Pt clusters and reduces two proton into H_2. Simultaneously, a photoexcited hole oxidize H_2O molecules to generate O_2. (b) Schematic illustrating the thermodynamic requirements for photocatalytic overall water splitting: the reduction potential of H^+/H_2 and the oxidation potential of H_2O/O_2 must lie within the bandgap of the photocatalyst. The presence of Pt metal serves as an electron acceptor with a low Fermi level. NHE denotes that all potentials are measured relative to the normal hydrogen electrode. (c) variation of the Gibbs free energy (G) during the water splitting process. The reaction is endothermic, requiring a positive ΔG. The presence of the Pt cocatalyst reduces the energy barrier of the reaction.

facilitating the formation of a more favorable transition state. These cocatalysts are typically metals, metal oxides, or organic molecules that serve as electron or hole acceptors. Common electron-accepting cocatalysts include Pt, Au, Ni, Pd, and Rh, while hole-accepting materials include Ag, RuO_2, and IrO_2. In addition to reducing activation energy, cocatalysts play a critical role in promoting the separation and transfer of photogenerated charge carriers—factors essential for effective photocatalytic water splitting. Typically, the recombination of photoexcited charges occurs on the picosecond to microsecond timescale, whereas surface reactions with adsorbed species take place over microseconds to seconds. The transfer and localization of charge carriers at cocatalyst sites reduce the probability of radiative recombination, thereby enhancing overall photocatalytic efficiency. Furthermore, cocatalysts provide abundant surface active sites, which accelerate catalytic reactions and enhance performance.

[105] Among them, Pt is particularly effective with its Fermi level close to the reduction potential of H^+/H_2, making it an ideal electron acceptor widely used for photocatalytic hydrogen evolution.[105] Figure 2.8 illustrates the role of Pt as an electron acceptor in the water-splitting process. Numerous studies have demonstrated that the co-loading of both reduction and oxidation cocatalysts on semiconductor surfaces significantly enhances photocatalytic activity for hydrogen and oxygen evolution, as well as for overall water splitting.[106] A notable example highlighting the importance of dual cocatalysts is the Pt–PdS/CdS photocatalyst reported in 2009.[107]

However, achieving overall water splitting with a H_2/O_2 molar ratio of 2:1 remains challenging. The generation of molecular oxygen from water is thermodynamically and kinetically more demanding than hydrogen evolution, as it requires the participation of four photoexcited holes and proceeds through a series of complex intermediates. Additionally, back reactions further contribute to the low oxygen production efficiency. In comparison, hydrogen production is more efficient and considered more promising in the field of photocatalysis. Therefore, it is a practical and strategic approach to focus on the hydrogen evolution half-reaction, rather than complete water splitting. Photogenerated holes are often scavenged directly or indirectly by a sacrificial agent. In the following text, the focus is placed specifically on hydrogen generation.

Besides water, many organic compounds can readily donate protons for hydrogen evolution shown in Equation 2.20. Alcohols containing hydroxyl groups, such as inexpensive and widely available methanol and ethanol, are good choices. Proton sources are not limited to liquids; they can also exist in gaseous or solid forms. The solid-gas or solid-solid interface avoids solvent-induced side reactions or the degradation of sensitive photocatalysts. In 1977, Schrauzer and Guth reported the first water vapor splitting using TiO_2 and Fe-doped TiO_2 with a stoichiometric ratio $H_2/O_2 = 2$.[108] Suguro et al. offered a historical overview of photocatalytic water splitting under vapor feeding, and discussed the principles of water

adsorption on the surface of semiconductors.[109] Till now, more gasous proton sources such as H_2S, methanol are explored for hydrogen evolution.[110] In addition, hydrogen evolution from photocatalytic biomass (cellulose, lignin, chitosan et al.) and biomass-derived substrates (including ethanol, glycerol, formic acid, glucose, and polysaccharides), is gaining popularity due to their abundance and renewability in nature.[111]

2.3.2 Colloidal Nanocrystals for Photocatalytic H_2 Evolution

The past decades have witnessed an explosion of interest in photocatalytic H_2 evolution. Since the landmark discovery by Honda and Fujishima in 1972 that titanium dioxide can split water under ultraviolet light.[103] It is generally accepted that a hydrogen production system achieving a solar-to-hydrogen conversion efficiency of approximately 10% would be considered viable for commercial application.[112] Despite significant progress, artificial photosynthesis of hydrogen remains inefficient for industry with solely robust and earth-abundant materials. Improving the performance of sustainable solar-to-fuel conversion demands a deeper understanding of photocatalytic mechanism with advanced scientific techniques. Conventional synthetic techniques (solid-state reactions, hydrothermal reactions, sol–gel processing, et al.) yield heterogeneous materials that are suboptimal for precise spectroscopic investigation.[113] Thus, the rational design and precise engineering of photocatalysts are essential for elucidating the structural and optoelectronic properties that govern their catalytic behavior.

Colloidal semiconductor NCs have been at the forefront of these efforts owing to their size-tunable optical and electronic properties as well as advances in their synthetic methods that produce monodisperse, well-defined structures. They have been shown to be very effective for hydrogen evolution, particularly when coupled with noble metal cocatalysts.[114–116]

Among these, metal chalcogenide NCs stand out, as they combine visible-light absorption with efficient charge transfer properties, and favorable band alignment with water redox potentials. For instance, H_2 production with CdS nanorods can reach a 7% power conversion efficiency (90% quantum efficiency) when a Pt nanoparticle is placed at the tip of a nanorod.[117] This configuration enables good spatial separation between electrons transferring to the Pt nanoparticles and a short pathway for hole collection in the radial direction.[117]

For photocatalytic hydrogen evolution, holes can be confined within specific regions of the nanostructure that act like a trap, in addition to scavenging them with a chemical agent. The use of heterostructured nanointerfaces, such as those in CdSe/CdS and ZnSe/CdS core-shell NCs, has been shown to further enhance hydrogen production efficiency by promoting spatial separation of charge carriers across distinct domains.[118] In CdSe/CdS/Pt NCs, for instance, photoexcited holes are localized in the CdSe core for oxidation reactions while electrons migrate to the CdS shell and subsequently to Pt domain, facilitating efficient hydrogen evolution.

Besides metal chalcogenides, metal oxide nanocrystals (e.g., TiO_2, ZnO, WO_3, $BiVO_4$) have been extensively studied for photocatalytic hydrogen evolution due to their high stability and low toxicity. However, their large bandgaps limit visible-light absorption, and they often exhibit poor colloidal dispersibility. Carbon dots, composed of polyaromatic hydrocarbons functionalized with various surface groups, have recently gained significant attention in the field of photocatalysis.[119] The appeal lies in their versatility, excellent photostability, absence of toxic heavy metals, ease of synthesis, and highly tunable optical and electronic properties. While the application potential is impressive, a detailed understanding of their structure and the mechanisms underlying photocatalytic reactions is required in the future.

2.3.3 What about Pb-Based Perovskites?

As previously discussed, there is a strong demand for the development of efficient photocatalysts for hydrogen production that meet several key criteria: (1) a bandgap energy within the visible light range to ensure maximum utilization of solar energy; (2) CB band minima appropriately positioned to drive proton-reduction half reactions; and (3) well-defined nanostructures that allow for precise spectroscopic characterization and mechanistic understanding.

LHPs have risen through the ranks to become one of the most promising photocatalysts. They exhibit exceptional light absorption capabilities, long charge-carrier diffusion lengths, and high extinction coefficients. These indicate that they enable efficient absorption of sunlight and transport of photoinduced charge carriers over micrometer-scale distances to active surface sites for redox reactions.[31] Moreover, their compositional and size versatility allows for precise band structure tailoring to fit specific applications.

However, LHPs are well known to be highly unstable in the presence of moisture, which limits their direct application in photocatalytic water splitting. As a result, most advances in hydrogen production using LHPs have been achieved through a process called acid splitting, involving a series of reactions. In 2017, Park et al. demonstrated that methylammonium lead iodide can stabilize in an aqueous hydroiodic acid (HI) solution by maintaining a precipitation–solubility equilibrium.[13] Under these conditions, it is capable of reforming HI into hydrogen (H_2) and triiodide (I_3^-), extending the large interest in HPs from photovoltaics to heterogeneous photocatalysis:

$$3HI \rightarrow H_2 + I_3^- + H^+ \tag{2.23}$$

Wu et al. enhanced the photocatalytic performance of a mixed-halide perovskite with platinum cocatalyst, $MAPbBr_{3-x}I_x$/Pt, proposing a band gap funneling mechanism driven by a halide gradient that directs charge carriers toward the surface.[120] The inclusion of Pt nanoparticles effectively suppresses charge recombination, resulting in a hydrogen evolution rate of $2605\,\mu mol\,g^{-1}\,h^{-1}$ with stable activity over six cycles and 30 hours of operation. However, in HX acid solutions, the oxidation of X^- to X_3^- takes priority over water oxidation, rendering

overall water splitting unfeasible. To sustain the photocatalytic cycle, additional reducing agents such as hypophosphorous acid (H_3PO_2) are required to convert X_3^- back to X^-. Moreover, the strong acidity of HX limits the choice of cocatalysts, as many are unstable or degrade under such harsh conditions.

A straightforward approach to stabilizing LHPs is encapsulating them within a protective shell in core–shell structures. This shell acts as a barrier, preventing direct contact between LHPs with polar molecules. For example, Xu et al. employed amorphous TiO_2 as the encapsulating layer to synthesize $CsPbBr_3$@TiO_2 core–shell particles, which demonstrated significantly improved stability—retaining over 90% of their initial photocatalytic activity after 15 hours of operation.[121] However, the shell materials may partially obstruct light absorption by the MHP core. An alternative strategy involves coating the LHP nanocrystal surface with hydrophobic ligands to create a waterproof barrier. Mu et al. applied this method to their $CsPbBr_3/Cs_4PbBr_6$ nanocrystals, using hexafluorobutyl methacrylate, a highly hydrophobic ligand. This modification conferred exceptional water resistance: after 100 hours of immersion in water, 90% of the PL intensity was preserved.[122] However, such ligand-based encapsulation is less suitable for photocatalytic applications that demand fast adsorption of reactants and efficient desorption of products, due to the diffusion-limiting nature of the hydrophobic coating.

Recently, water vapor at 100% humidity was employed as a reactant in photocatalytic water splitting using the $MA_2CuCl_2Br_2$ catalyst, achieving continuous operation for 24 hours.[123] However, the hydrogen production of LHPs was significantly lower in this work, reaching only 0.11 μmol g^{-1} h^{-1}. In this thesis, the hydrogen generation activity of LHPs is significantly enhanced using LHPs/Pt nanostructures under methanol vapor. The charge carrier transfer mechanism is also investigated in detail, as shown in Chapter 4.

3

Materials and Experimental Methods

This chapter provides a detailed overview of the experimental techniques used, including material synthesis and analysis methods, which underpin the results presented in this thesis. Two synthesis approaches for halide perovskite nanocrystals (NCs), the tip sonication and hot injection methods, are introduced in Section 3.1. They are employed in Chapter 4 and Chapter 5 to meet specific demands, respectively. The tip sonication method offers an efficient and cost-effective way for synthesizing lead halide perovskite (LHP) nanoplatelets (NPls), as well as their large-scale application in photocatalysis. However, the hot injection synthesis guarantees high quality and a small size distribution of double perovskite (DP) NCs, which is beneficial for manipulating their optical transitions. Subsequent characterization of these NCs requires a variety of optical techniques, such as time-resolved photoluminescence (PL) and transient absorption spectroscopy (TAS), which are discussed in detail in Section 3.2. Finally, the generation and detection of hydrogen from photocatalytic reactions are described in Section 3.3.

3.1 The Synthesis of Halide Perovskite Nanocrystals

Colloidal semiconductor NCs, are semiconductor crystallites smaller than 100 nm in at least one dimension, suspended colloidally in a liquid solution.[124] They are synthesized at temperatures ranging from room temperature to 400℃, with the involvement of surface capping ligands (usually organic ligands with long carbon chains) to control the nucleation, growth, and colloidal stability. The synthesis of the first perovskite NCs in 2014[6] brought them back to the forefront of research, following the groundbreaking discovery of perovskite films in photovoltaics in 2012.[31] Over the past decade, remarkable control of colloidal perovskite NCs has been achieved over composition, size, morphology, surface chemistry, and self-assembly. For example, one can prepare perovskite nanospheres,[10] nanocubes,[88] NPls,[54] nanosheets,[125] and nanowires.[126] The sizes of these nanostructures can be tuned from a monolayer of perovskite unit cells with strong quantum confinement, to NCs with sizes close to the exciton Bohr radius (in the weak quantum confinement regime), and up to bulk-like NCs whose sizes are large enough to exhibit optical properties similar to those of their bulk crystals or films.

The synthetic methods of perovskite NCs are summarized into "bottom-up" and "top-down" strategies.[127] Traditional "top-down" methods, such as physical exfoliation or chemical etching, offer limited precision and control over the size and shape of NCs.[128,129] Manipulations of optical properties of perovskite NCs require decent samples with precisely defined size and shape. "Bottom-up" methods, which start with small atomic-scale fragments growing into well-designed NCs, are advantageous over "top-down" approaches at this point and have gained overwhelming popularity.[8]

Hot injection synthesis is one of the most developed methods among liquid-phase "Bottom-up" approaches.[127] It offers NCs with high quality and crystallinity, as well as a small size distribution. As a result, NCs obtained from hot injection synthesis are ideal for researchers to investigate their photophysical properties. However, this method increases the cost for large-scale applications due to the high-temperature inert atmosphere required.

A facile, room-temperature method, known as the tip sonication method, has been developed to achieve high convenience and productivity of NC synthesis for various applications.[130] In my thesis, I have employed both the large-scale tip sonication method and the precise hot injection method to meet specific demands, photocatalysis in polar vapor (Chapter 4) and investigation of broad white-light emission (Chapter 5), respectively.

3.1.1 Lead Halide Perovskite Nanoplatelets via the Tip Sonication Method

It is reported that high intensity ultrasound can be employed to produce novel materials and offers an alternative route to known materials, without exerting high temperatures, high

pressures, prolonged reaction times, or laborious reaction steps.[131] Compared to traditional energy sources, ultrasonic irradiation provides a pulse of extremely high temperatures and pressures in liquids, which cannot be achieved by other methods.[132]

The chemical and physical effects of ultrasound do not originate from a direct interaction between chemical species and sound waves, but from the physical phenomenon of acoustic cavitation—the formation, growth, and implosive collapse of bubbles.[132,133] Under ultrasound irradiation, sound waves propagate through the liquid and simultaneously create microbubbles from dissolved gases such as O_2, N_2 or Ar, and other existing impurities. With accumulating energy, these microbubbles experience a fast inertial overgrowth through a series of cavitation stages, until they collapse catastrophically inward. This bubble implosion occurs in less than one microsecond, generating local 'hot spots' with high local temperatures of up to 10,000 K and pressures as high as 10,000 atm. The combination of extreme local conditions and rapid cooling creates a unique environment for driving high-energy chemical reactions under these intense conditions.

With tip sonication, a careful selection of controlled and optimized parameters is necessary for minimal defect formation and higher NC homogeneity. The sonication intensity influences the frequency of cavitation events per unit volume occurring within the solvent. The higher the intensity, the more frequently cavitation activities occur. This results in stronger collapses. The sonication time is an indicator of the total energy input to disperse and monitor defect progression.

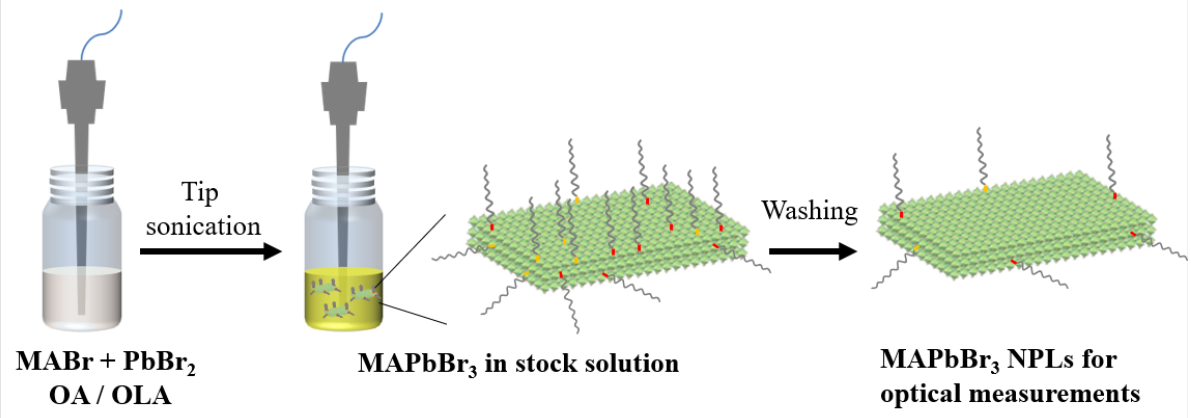

Figure 3.1: Tip Sonication Synthesis of $MAPbBr_3$ NPls The schematic diagram illustrates the synthesis of $MAPbBr_3$ NPls. The reaction is carried out using a sonicator under a power of 15 W for 10 minutes. After the reaction, the stock solution is cooled in an ice bath and washed several times with ethyl acetate and hexane. The NPls are then redispersed in hexane for further use.

The tip sonication method applied to LHP NCs was developed by Tong et al..[130] Since then, perovskite NCs with different shapes, such as nanowires,[134] NPls,[130] and nanocubes,[135] have been reported. This is realized by a variation of ligands with different functional groups, ligand-to-precursor ratios, sonication intensity, and sonication time. In Chapter 4, I use

this method to prepare $MAPbBr_3/CsPbBr_3$ NPls with a large surface-to-volume ratio, which is beneficial for abundant active sites in photocatalytic reactions. Taking $MAPbBr_3$ as an example (Figure 3.1), acoustic cavitation activates the formation of methylammonium–oleate complexes in the mixture of octedecene (ODE), oleic acid (OA) and oleylamine (OLA). The complexes react with $PbBr_2$ dissolved in the solvents—nucleate and grow with the inducing of surface surfactants, yielding a mixture of $MAPbBr_3$ NPls and their precursors in a one-pot process. Further purification is carried out to remove unreacted precursors and excess ligands, including anti-solvent washing and precipitation procedures. The NPls are redispersed in hexane, and the colloidal suspension is ready for further characterization. The morphology characterized by transmission electron microscopy (TEM) of these NPls is shown in Figure 4.4b and c. They indicate a two-dimensional platelet shape with variable lateral sizes of several hundred nanometers.

3.1.2 $Cs_2AgBiCl_6$ Nanocrystals via the Hot Injection Method

The hot injection approach is referred to as the rapid injection of a precursor into a hot solution containing the remaining precursors, ligands, and a solvent with a high boiling point.[8,136] The method typically enables the synthesis of small NCs with a narrow size distribution by separating the nucleation and growth stages, as described by the LaMer mechanism.[136,137] To achieve this, a quick injection of the precursor must be ensured. Immediately after the injection of the external reagent into the hot solvent, a rapid nucleation burst occurs with the simultaneous formation of small nuclei. Injection also initiates a sudden drop in

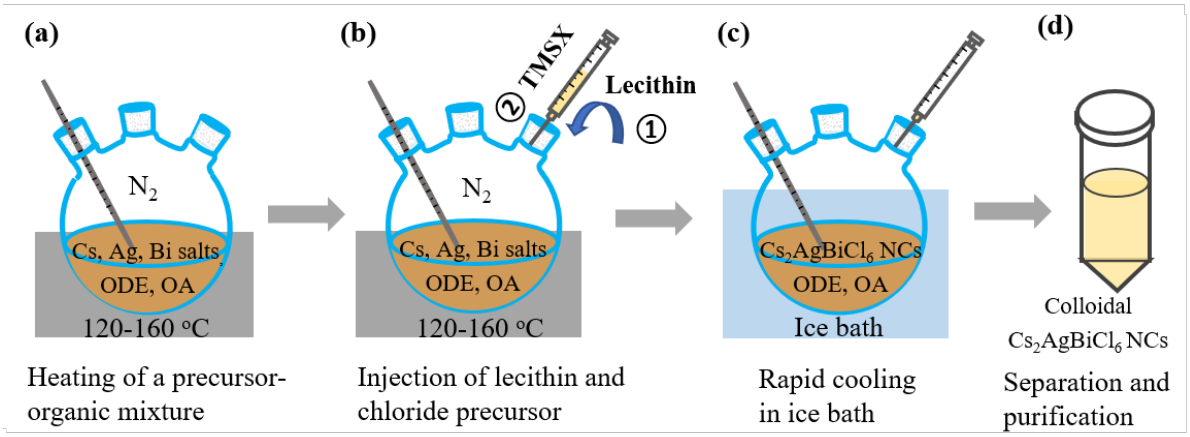

Figure 3.2: Hot Injection Synthesis of $Cs_2AgBiCl_6$ NCs The schematic diagram illustrates four steps for the synthesis of $Cs_2AgBiCl_6$ NCs, which are written at the bottom. The reaction occurs under a N_2 atmosphere. The reaction temperature is tuned from 120 ˚C to 160 ˚C to regulate crystal sizes. In the second step, the chloride source termed trimethylsilyl chloride (TMSCl) is added to the hot solution immediately, following the addition of lecithin. In the last step, ethyl acetate is used to isolate the NCs from the stock solution. After centrifugation, the NCs are redispersed in toluene to form a $Cs_2AgBiCl_6$ colloidal suspension.

temperature. Together with the temperature decrease, a fast depletion of monomers terminates the nucleation stage, following the nucleus growth stage with monomers diffusing to their surface. In this stage, typical processes called size focusing (NCs grow uniformly) and Ostwald ripening (larger NCs grow at the expense of smaller ones) take place subsequently with the decrease of monomer concentration, which results in a narrow or a broad size distribution, respectively.

Stopping the reaction at the precise moment in the size-focusing regime, just before ripening becomes significant, allows for the formation of NCs that are small, monodisperse, and highly uniform.[127] Therefore, careful management of reaction time and temperature is essential to maintain size control and prevent the dominance of Ostwald ripening.

To prepare $Cs_2AgBiCl_6$ NCs in Chapter 5 (Figure 3.2), an organic chloride is injected into a hot solution (120–160℃) of ODE and OA with dissolved cesium, silver and bismuth salts.

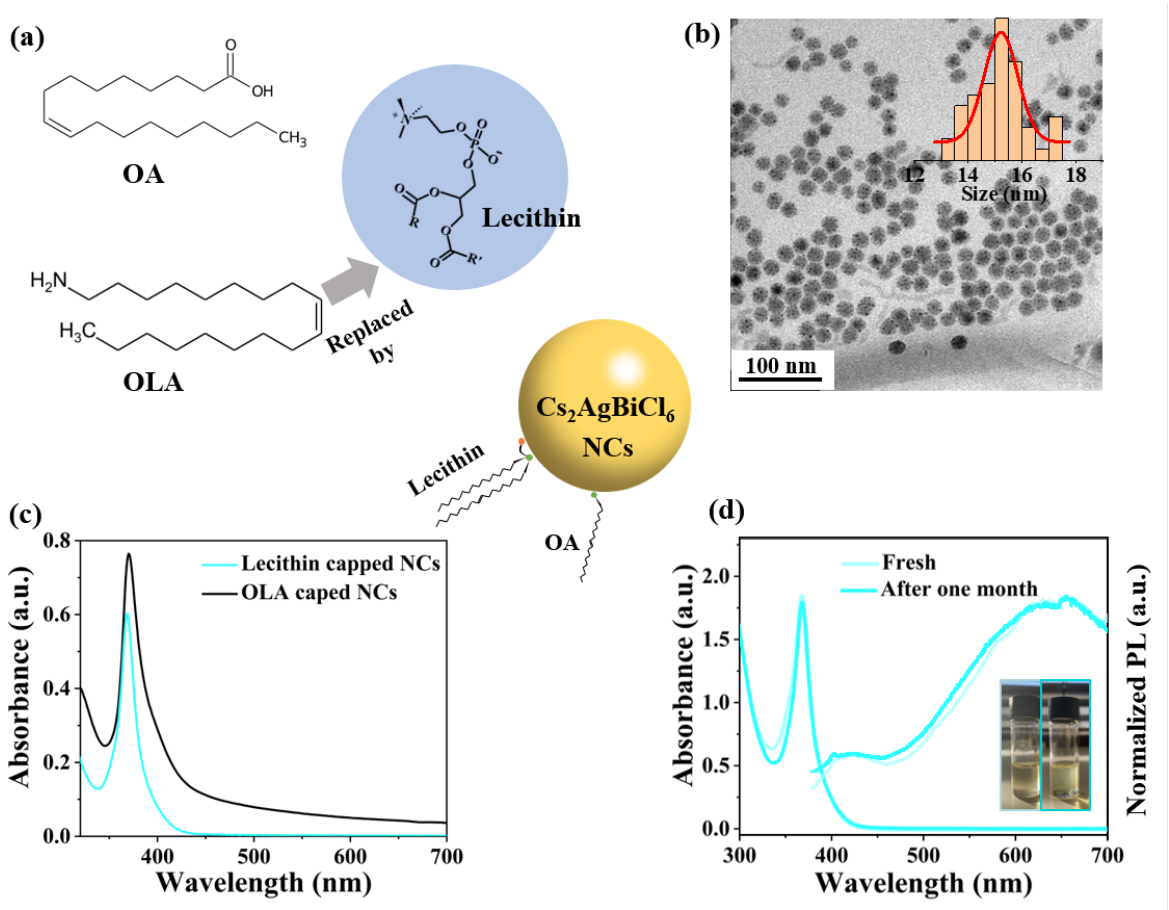

Figure 3.3: Colloidal Stability of $Cs_2AgBiCl_6$ NCs The central sketch depicts a $Cs_2AgBiCl_6$ NC attached with a lecithin molecule and an OA molecule, which indicates its colloidal stability. (a) shows molecular structures of OA, OLA, and lecithin. OLA is replaced by lecithin in the hot injection synthesis. (b) TEM image of $Cs_2AgBiCl_6$ NCs. The insert shows a size distribution centered at 15 nm. (c) Absorption spectra of fresh NCs with lecithin and OLA. (d) Comparison of absorption spectra of $Cs_2AgBiCl_6$ NCs for fresh samples and those after one month, as well as PL. The insert displays their colloidal suspension before and after one month.

The whole reaction is protected by an inert gas—N_2. Lecithin is added to the hot solution several seconds before the injection of the chloride source. An ice bath brings the reaction to an abrupt halt to control the reaction time. Post-synthesis procedures are performed for purification and colloidal stability of NCs. After the reaction, NCs are isolated from unreacted precursors with the help of antisolvents and a centrifugal force, then re-dispersed in nonpolar solvents.

It is noted that the long-chain amine—OLA, which is commonly used in combination with OA for a hot injection synthesis, is not employed here. Alternatively, I demonstrate that soy lecithin, a mass-produced natural phospholipid, serves as a surface-capping ligand for the better colloidal stability of $Cs_2AgBiCl_6$ NCs (12–22 nm) with a high yield (Figure 3.3a). Additionally, the use of lecithin prevents the facile reduction of silver ions in the presence of OLA. Figure 3.3b shows as-prepared $Cs_2AgBiCl_6$ NCs with a size distribution centered at 15 nm. Unlike typical nanocubes acquired from a hot injection synthesis with OLA, these NCs are spherical. It is known that surfactant molecules play a key role in modulating the kinetics of nucleation and growth, which dynamically and selectively adhere to specific surfaces of growing crystals, thus influencing NC shapes. Compared to OLA, long-chain lecithin molecules show less facet preference, allowing for the growth of all the crystal facets. This results in the formation of a spherical shape.

Figure 3.3c displays the absorption spectra of $Cs_2AgBiCl_6$ NCs capped with OLA and lecithin commonly together with OA. The OLA-attached NC solution shows much light scattering and worse colloidal stability. The NCs protected with lecithin do not exhibit this issue. Moreover, lecithin decoration ensures long-term retention of the colloidal and structural integrity of $Cs_2AgBiCl_6$ NCs in ultraconcentrated colloidal solutions. As shown in Figure 3.3d, the NCs with this long-chain zwitterionic ligand remain stable without degradation and precipitation for at least one month. This stability arises from increased particle-particle repulsion, due to the presence of abundant branched chains and ligand polydispersity.[138,139]

3.2 Optical Spectroscopy of Halide Perovskite Nanocrystals

Optical transitions and carrier recombination have been introduced in Chapter 2. In this section, I will introduce characterization techniques, including absorption and PL spectroscopy of halide perovskite NCs.

3.2.1 Absorption Spectroscopy

Linear Absorption Spectroscopy

When a light beam encounters an optical medium, several phenomena arise due to light-matter interactions, which can be categorized into three main types: reflection, propagation, and transmission. As light propagates through the medium, several processes may take place, including refraction, absorption, luminescence, and scattering. Nonlinear optical effects, which occur under high-power conditions, are not discussed here. In the case of colloidal NC suspensions, it is assumed that light scattering, reflection, and refraction by the NCs is negligible when the NC sizes are much smaller than light wavelengths. Background effects from a cuvette and solvent are counteracted through reference measurements. In this case, light absorption by the NC ensemble can be measured with good precision by the reduction of transmitted light intensities compared to incident light intensities. The transmittance T is related to the absorption coefficient α, and the light pathlength through the sample d, or the absorbance or optical density OD:

$$T_\nu = \frac{I}{I_{0\,\nu}} = e^{-\alpha_\nu \cdot d} = 10^{-OD_\nu} \tag{3.1}$$

where I_0 is the intensity of the incident light and I is the intensity of the transmitted light. OD can be related to the extinction coefficient ε, the light pathlength through the sample d, and the sample concentration c in the Bouguer-Lambert-Beer law. It provides the mathematical and physical basis of light absorption measurements for gaseous and aqueous samples from ultraviolet to infrared light regions:[140]

$$OD_\nu = -\lg(\frac{I}{I_0})_\nu = \varepsilon_\nu \cdot c \cdot d \tag{3.2}$$

$\varepsilon_\nu = \frac{OD_\nu}{c \cdot d}$ is the molar decadic extinction coefficient, which is an inherent property of substances and varies with frequencies/wavelengths. The variation of ε_ν versus frequencies/wavelengths is termed as the "absorption spectrum" of a substance. As it may span several orders of magnitude for a single material, we usually use its logarithmic value $lg(\varepsilon)$ to plot an absorption

spectrum. The Bouguer-Lambert-Beer law only applies to dilute solutions, as the extinction coefficient ε is no longer constant for concentrated solutions but depends on the refractive index of the solution. A quartz cuvette is utilized to measure the UV-Vis spectra of solutions, which may decrease the incident light intensity by reflection at the front and back cuvette surfaces. To eliminate the error from the cuvette as well as the solvent, a blank measurement is usually employed with the standard cuvette containing the pure solvent.

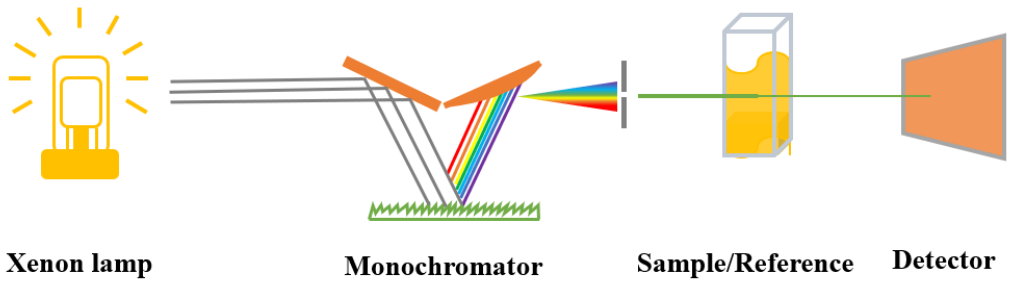

Figure 3.4: Working Principle of Cary 60 UV-Vis Spectrophotometer A simplified schematic diagram shows how a *Cary 60* UV-Vis Spectrophotometer works. A Xenon Flash Lamp emits a short, intense pulse of light covering the UV to visible spectrum. The light is separated into different wavelengths of light by a monochromator, which will pass through a sample/reference. The transmitted light is collected and converted into electrical signals by a detector.

In my thesis, all steady-state absorption spectra were acquired with a *Cary 60* UV-Vis spectrophotometer (*Agilent Technologies*). It is capable of fast measurements at room temperature over a broad spectral range with easy operation. In Figure 3.4, it contains a Xenon Flash Lamp (80 Hz) generating a broadband of electromagnetic radiation spanning 190-1100 nm wavelength range. White light is directed into a Czerny-Turner monochromator, where it is dispersed by a diffraction grating. A narrow wavelength band is then selected using an exit slit, allowing specific wavelengths to be isolated for measurement. The light coming out from the monochromator illuminates a sample/reference in the sample chamber. The transmitted light is collected via the detector. Other optical components, such as lenses, mirrors, or fiber-optics, which relay light through the instrument, are neglected in the schematic diagram. Moreover, it is flexible to set up the scanning wavelength range and the scanning speed by changing the average wavelength interval of every point. Here, baseline correction can be introduced by uploading a file or carrying out a preliminary measurement with a standard sample. All samples are contained in quartz cuvettes with 1 cm light pathway.

Transient Absorption Spectroscopy

TAS is a pump-probe spectroscopic technique using the absorbance/transmittance variation upon a second laser pulse to investigate short-lived and transient electronic states. With time-resolved absorption spectroscopy, the evolution of non-emissive and dark states can

be investigated, which is not achievable with time-resolved fluorescence.[141] For transient absorption measurements, NC are partially excited to an electronically excited state under a pump pulse. A second laser pulse, referred to as a probe pulse, is imparted in the same place of the sample with a time delay of τ compared to the pump pulse. It is usually white light with a low power intensity to avoid multiple processes. When both a pump and a probe laser pulse are applied, the sample absorbs less light than it does with only the probe pulse, because photoexcited charge carriers are already occupying some of the excited states. To eliminate the specific absorption of the sample in the ground state, the absorbance difference with and without the pump pulse excitation is calculated and recorded, referred to;

$$\begin{aligned}\Delta OD &= OD_{\text{pump}} - OD_{\text{no pump}} \\ &= -\lg\left(\frac{I_{\text{pump}}}{I_0}\right) - \left(-\lg\left(\frac{I_{\text{no pump}}}{I_0}\right)\right) \\ &= \lg(I_{\text{no pump}}) - \lg(I_{\text{pump}}) \\ &= \lg\left(\frac{I_{\text{no pump}}}{I_{\text{pump}}}\right)\end{aligned} \tag{3.3}$$

It is influenced by the time delay τ between the probe and pump pulses. By varying the delay time τ and the detection wavelength λ, we monitor a ΔOD profile with respect to τ and λ—that is $-\Delta OD(\tau, \lambda)$.

Transient absorption spectra presented in my thesis are acquired by a custom-built transient absorption spectrometer by *Newport*. The pump and probe beams originate from the same laser source, which is a 800 nm laser created by a *Libra-HE+ Ti:Sapphire* amplifier system (*Coherent Inc.*). The laser pulses have a duration of 100 fs and a repetition rate of 1 kHz. It is split into pump and probe beams with a power ratio of 98:2 by a beam splitter. Passing through a BBO crystal, the pump laser frequency is doubled to 400 nm based on second-harmonic generation. In my thesis, a pump laser with a 400 nm wavelength was used. For a pump beam with different wavelengths, an optical parametric amplifier (190 nm-12 μm, *OPerA Solo*, built by *Light Conversion* and distributed by *Coherent*) is applied. The pump beam is directed through a chopper wheel, which works with half of the laser repetition rate (500 Hz) to block every alternate pulse. Therefore, the optical densities with and without the pump laser excitation are recorded. The pump pulse passes through a gradient ND filter and is then guided into samples in a cuvette (1 mm) or on a substrate. Before the sample, a power meter (*Newport*, *919E-20U-10-20K*) is mounted on the pathway via a flip mirror.

For the probe beam, the laser is directed through a retroreflector mounted on a linear delay stage to control its pathlength, thereby allowing precise tuning of the time difference τ between the probe and pump pulses (maximum 3 ns). When τ is zero, it indicates that the pump pulse and the probe pulse arrive at the sample simultaneously. The position of the

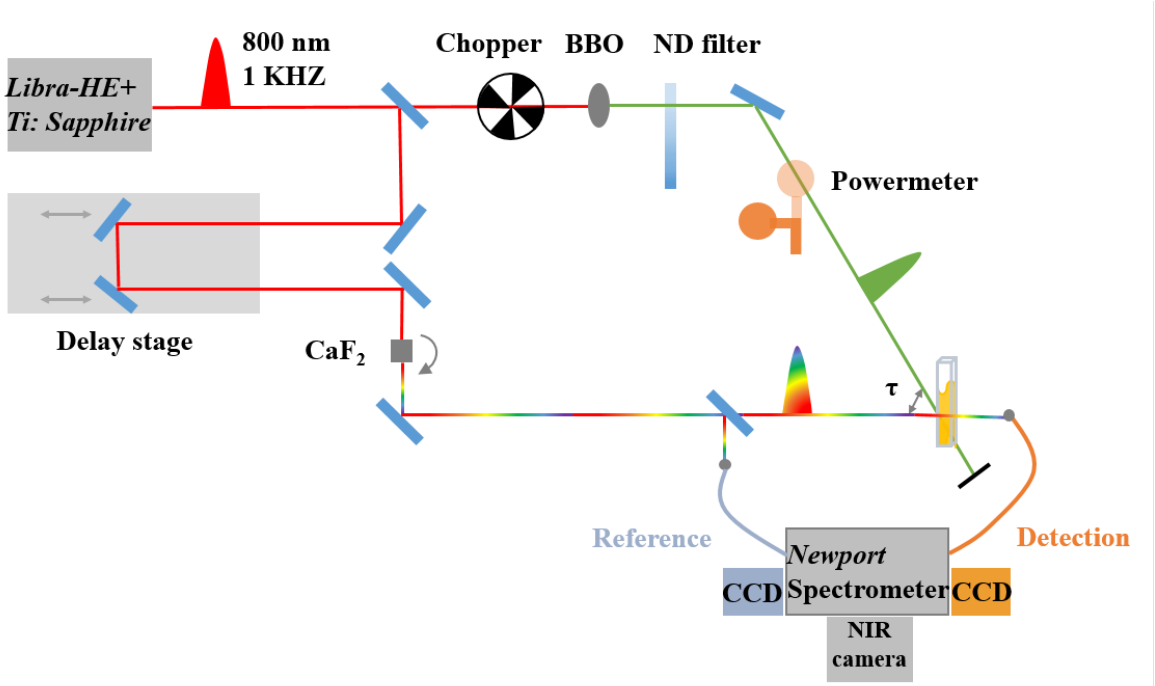

Figure 3.5: TAS Setup Originating from *Libra-HE+* amplifier, a laser pulse with its wavelength of 800 nm and its repetition rate of 1 KHZ is split into two beams via a beam splitter. One is referred to as a pump pulse, the other acts as a probe pulse. The pump pulse is directed through a chopper with a repetition rate of 500 HZ for alternative detection with and without the pump beam. The laser frequency is then converted to the second harmonic (corresponding to 400 nm wavelength) with the help of a β-Barium borate (BBO) crystal. A gradient neutral density (ND) filter and a flip power meter are mounted on the pathway to monitor the laser energy. After multiple mirrors, the pump beam illuminates the sample in a cuvette of 1 mm thickness. For the probe beam, it goes through a translation stage which controls the arrival time difference τ between the pump and the probe beams at the sample. When τ is zero, both beams illuminate the sample at the same time. The probe pulse passes through a CaF_2 crystal, converted into a white pulse. The white probe beam is split into a detection beam and a reference beam before the sample. The detection pulse excites the sample overlapping the excitation spot of the pump beam. Its transmitted light is coupled into a dual optical fiber, which connects a spectrometer and a charge-coupled device (CCD). The white light pulse before the sample is also detected with a separate CCD for reference.

retroreflector where τ is zero is calibrated according to the spectral variation. The laser beam is then focused on a CaF_2 crystal to generate white-light laser pulses. To prevent damage to the crystal, a translation stage is used to move the crystal within the plane. The white light beam is collimated via parabolic mirrors and directed to overlap the illumination spot of the pump beam (650 µm). The excitation spot of the pump beam on the sample is larger than that of the probe beam, ensuring that the probed samples are in their excited states.

The samples in solution or film are placed on a manual XYZ-stage, which enables spatial translation in three directions. The absorbance of the samples is maintained at approximately 0.1 to reduce scattering and other optical losses. The transmitted light is coupled into an optical fiber, which has dual channels: one is an experimental channel accepting transmitted

white light, the other is a reference channel coupling a part of the white light before the sample. The fiber is connected to a spectrometer (*Newport*, *MS260i*) with three gratings. After the spectrometer, two light beams are directed into two CCDs, separately. With the help of reference detection of the original white light, fluctuations in the white light are eliminated. Moreover, a near-infrared camera is attached to the spectrometer for long-wavelength light detection.

3.2.2 Photoluminescence Spectroscopy

In the last section, I have introduced the mechanisms of absorption spectral measurements based on how a monochromatic light beam with a particular photon energy transmits through a colloidal suspension. The energies of the reflected and transmitted photons are the same as those of the incident photons. For PL spectral measurements, however, a light beam with photon energies relatively larger than (nonresonant) or equal to (resonant) material bandgaps is utilized to impinge a sample and then collect photons with different energies emitted from the sample. Typically, the band maxima of the emission spectrum are red-shifted in energy relative to those of the absorption spectrum for the same electronic transition—a phenomenon known as the Stokes shift. In rare cases, the emission band maxima appear at higher energy than the absorption maxima, which is referred to as an anti-Stokes shift.

The optical path configuration of PL setup is quite similar to that of absorption measurements. For PL measurements, emitted photons from all directions can be detected, such as the front of a cuvette where the light incidents, or the back, and the side. We could also collect emitted photons from all different angles with the help of an integrating sphere, which is carried out for the quantum yield measurement. Normally, the geometric alignment of PL detection with the light incidence is avoided, to prevent the impingement of the strong incident light which may saturate or even damage the photodetector. To avoid this, optical filters (such as long pass or short pass filters) can be added to block the probing photons from reaching the photodetector.

In my thesis, partial PL spectra were acquired from *Horiba Scientific Fluorolog-3-22*. The layout of basic components and available accessories for the system are customized for the needs of our group. In Figure 3.6, a 450 W Xe lamp produces photons with different energies, filtered by a double-grating excitation spectrometer. It allows for choosing a specific wavelength of light λ_{ex} (or narrow bands of light) to reach the sample. The second parameter that can be customized is the excitation slit width, which influences the spectral width as well as the excitation light intensity. The excitation light reaches samples in the compartment module. With different sample holders, PL of solutions in cuvettes or films on silicon substrates can be detected from two angles. That is: a right angle perpendicular to the excitation beam or a ”front-face” location whose angle with the excitation beam is smaller than 90°. The emitted

photons are isolated by an emission spectrometer and converted to electrical signals in a *R928P* photomultiplier detector. Here, the emission slit width is tunable to control emission intensities. An appropriate integration time is required for a good signal-to-noise ratio (0.05-2 s). The wavelength range of emission should be set between $\lambda_{ex} + \lambda_0$ to $2\lambda_{ex} - \lambda_0$ with a minimum λ_{ex} value of 15 nm, to avoid oversaturation by scattered light and the second order reflection. The variation of signal intensities (at a specific excitation) as a function of detection wavelength is recorded, and plotted as a PL spectrum. Fluctuations in excitation power are

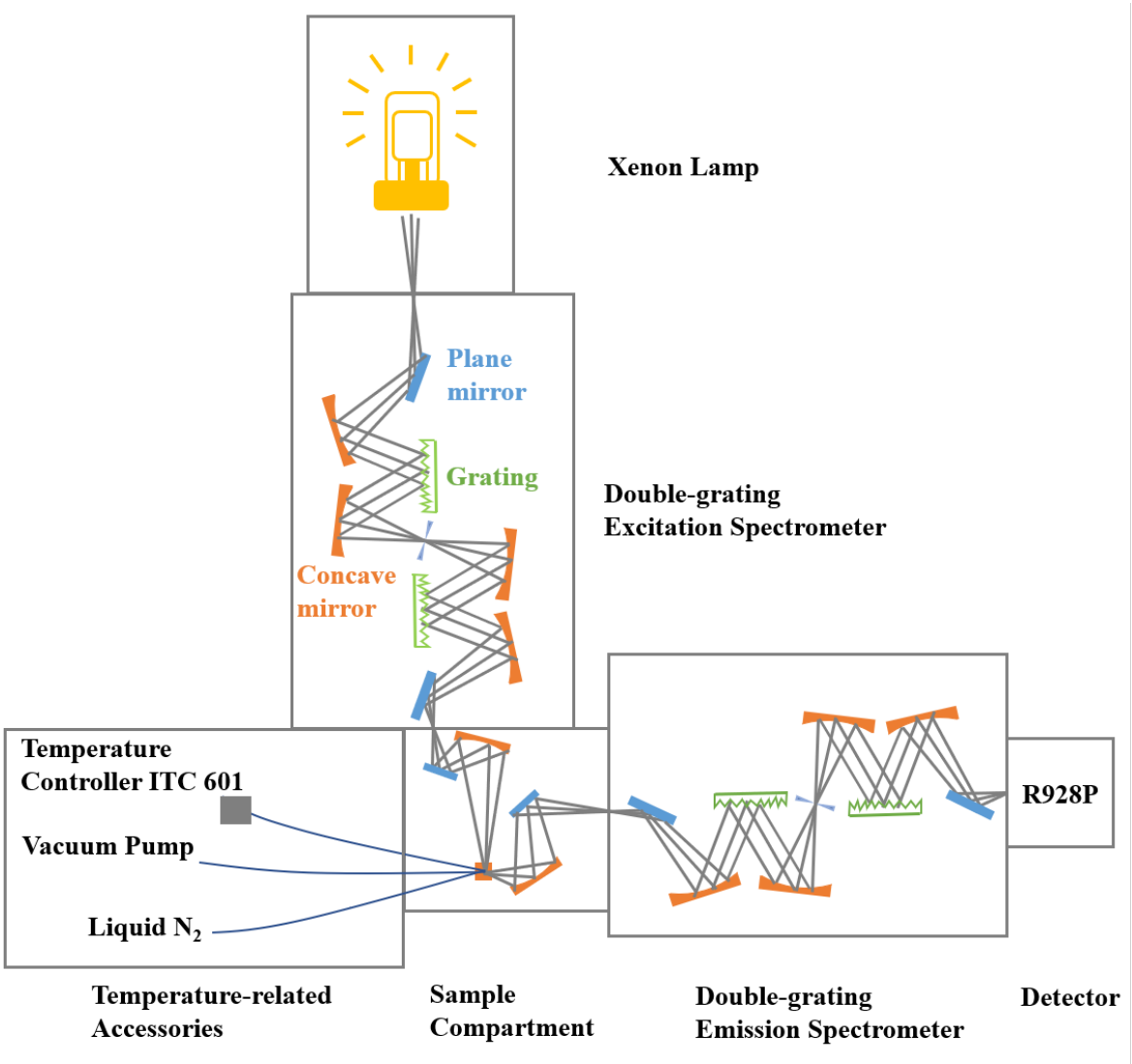

Figure 3.6: Working Principle of Horiba Fluorolog-3-22 A Xe lamp as a light source produces white light, which is filtered by a double-grating excitation spectrometer that selects a particular wavelength of light to illuminate the sample in the sample compartment. The emitted photons are partially collected and reach a double-grating emission spectrometer. Here, photons with different energies are isolated. The optical signals are converted into electronic signals in a photomultiplier detector *R928P* and recorded. Low-temperature measurements (77 K) are realized by attaching accessories to the system, including a temperature controller, vacuum pump, and liquid nitrogen.

accounted for to eliminate data errors via calibration. The data is plotted with the software *FluorEssence*.

Photoluminescence Excitation Spectroscopy

The setup allows for observing the variation of PL intensities detected at a specific wavelength in terms of excitation energies. It is referred to as photoluminescence excitation (PLE) measurements. During measurements, the excitation wavelength is scanned over the desired range using a monochromator, while the detection wavelength is kept fixed. For a PLE experiment, a prior knowledge of PL spectra, particularly emission peaks, is required to choose an emission wavelength for the detector to monitor. An appropriate excitation wavelength range is also required for acquiring information as well as avoiding oversaturating the detector. The other parameters for a PLE measurement setup are similar to those for PL measurements.

The signal intensity detected at a specific wavelength is proportional to the carrier density, which varies with the excitation energies. The carrier density is determined by the absorption coefficient. Therefore, PLE spectra of NCs usually follow their absorption spectra, but differentiate for specific processes. The differences highlight other competing decay processes, including non-radiative decay channels such as trapping, or charge carrier/energy transfer to different species. Hence, PLE spectra reflect how efficiently excitation at various higher-energy states contributes to emission from the lowest-energy state, providing insight into excitation and relaxation pathways.

Temperature-Dependent Photoluminescence

Temperature-dependent PL measurements are performed to investigate the influence of temperature on charge carrier recombination dynamics, which provides insights for trap-mediated recombination. The measurements can be performed using specific built-in attachments of the *Fluorolog-3-22* system. A vacuum pump, liquid nitrogen or helium, and a temperature controller are necessary to cool the samples to desired temperatures. The sample on a silica substrate is placed on a sample holder via silver lacquer. The holder is stuck into a self-designed chamber instead of a common sample compartment with a specific angle. The chamber is connected to a *Pfeiffer* vacuum pump, which creates a high vacuum inside the cryostat with pressures down to 10^{-6} hPa. Liquid nitrogen is sucked into the chamber to cool the sample down to 77K. An intelligent temperature controller (*ITC 601*) from *Oxford* Instruments is connected to acquire real-time temperatures through a sensor attached to the sample holder. With this setup, PL and PLE from room temperature to 77 K can be realized. The setup is schematically shown in Figure 3.6.

Micro-PL

Time-resolved PL and partial steady-state PL measurements are performed by a homemade so-called μ-PL spectroscopy setup, based on the method of time correlated single photon counting (TCSPC). The name originates from the fact that the spatial resolution of this setup is in the micrometer range. Compared to *Horiba* PL introduced on the last page, the setup is advantageous over single-molecule spectroscopy, which avoids spectral broadening of QD assemblies. It enables the detection of PL images and spectra by switching between a mirror and a reflection grating with a grating terret inside a spectrograph, as well as the observation of PL decay traces with nanosecond resolution. With accessories, low temperature PL and PL anisotropy measurements are achievable.

Figure 3.7 shows the schematic diagram of the TCSPC setup. A supercontinuum white light laser (*SuperK EXTREME EXR-20*, *NKT Photonics*) is employed with a repetition rate of 0.12-78 MHz (30-90 ps pulse length). Coupled with an acousto-optic modulator (*SuperK SELECT*, *NKT Photonics*) and an UV extension unit (*SuperK EXTEND-UV*), it allows for choosing a certain wavelength of light from 330-1100 nm. The switch, excitation wavelengths, repetition rates, and output power of laser are controlled by the software *CONTROL*. In my thesis, a 400 nm laser is used in Chapter 4 for both steady-state PL and time-resolved PL measurements. The laser beam output from a laser unit is aligned with the corresponding mirrors in its light path and spatially filtered by an iris aperture to remove other wavelengths of light. The beam intensity is tunable with a gray filter wheel in addition to the software. A flipable S120VC photodiode power sensor from Thorlabs is attached to measure the beam power. A longpass dichroic mirror is applied to direct the laser beam into a sample and cut it off after the illumination to avoid oversaturation of detection devices. To enhance these functions, an excitation filter and an emission filter are utilized together with the dichroic mirror. An *Attocube* objective *LT-APO/532-RAMAN/0.82* is installed to collimate the incoming beam and focus the excitation light inside the sample solution. The sample is mounted on a piezoelectric stage (*P-545 PI nano™XYZ*, *Physik Instrumente*), which is connected to a manual stage allowing movement in three directions. A small shift of 1 nm guarantees the precise adjustment of the focus position and detection spots. The emitted photons are collected by the objective, transmit through the emission filter, directed by a lens (*AC 254-300-A-ML*, f = 300 mm, *Thorlabs*) to a spectrograph (*Acton SpectraPro SP-2300*, *Princeton Instruments*) and a CCD camera (*PIXIS 400BR eXcelon*, *Princeton Instruments*). With these two devices, an image detection mode and a spectrum detection mode can be switched freely by the software *Light Field*.

Time-resolved PL decay measurements are achievable via a single photon counting module from *Excelitas*. To achieve this function, an optical multimode fiber (*AMS Technologies*) is connected to the spectrograph with a flip mirror. The fiber positioned at the center pixel of the CCD, which could couple in all light focusing on its entrance because of a larger numerical aperture. To choose single-wavelength detection or full-spectrum detection, one

could select grating mode or mirror mode in *TimeHarp*. The fiber is parallelly connected to two single-photon detectors (*SPCM-AQRH-16-FC*, *Excelitas Technologies*) with a detection range of 400–1060 nm. They are APDs with a time resolution of 350 ps and a low dark count rate of 25 cps, which ensures that weak signals can also be detected. In short, time-correlated single photon counting (TCSPC) works on the basis of correlating the detection of a laser trigger pulse with the detection of individual emitted photons. Upon the trigger of a laser pulse, a laser photon will experience some time in the optical and electrical pathways to be detected. A timer is set to characterize the time difference. It starts when a laser pulse triggers and stops as a PL photon is detected. The start/stop process repeats many times, and the time delays are acquired in a histogram with a bin width of 25 ps. The histogram corresponds to the instrument response function (IRF), which represents the actual response of the setup,

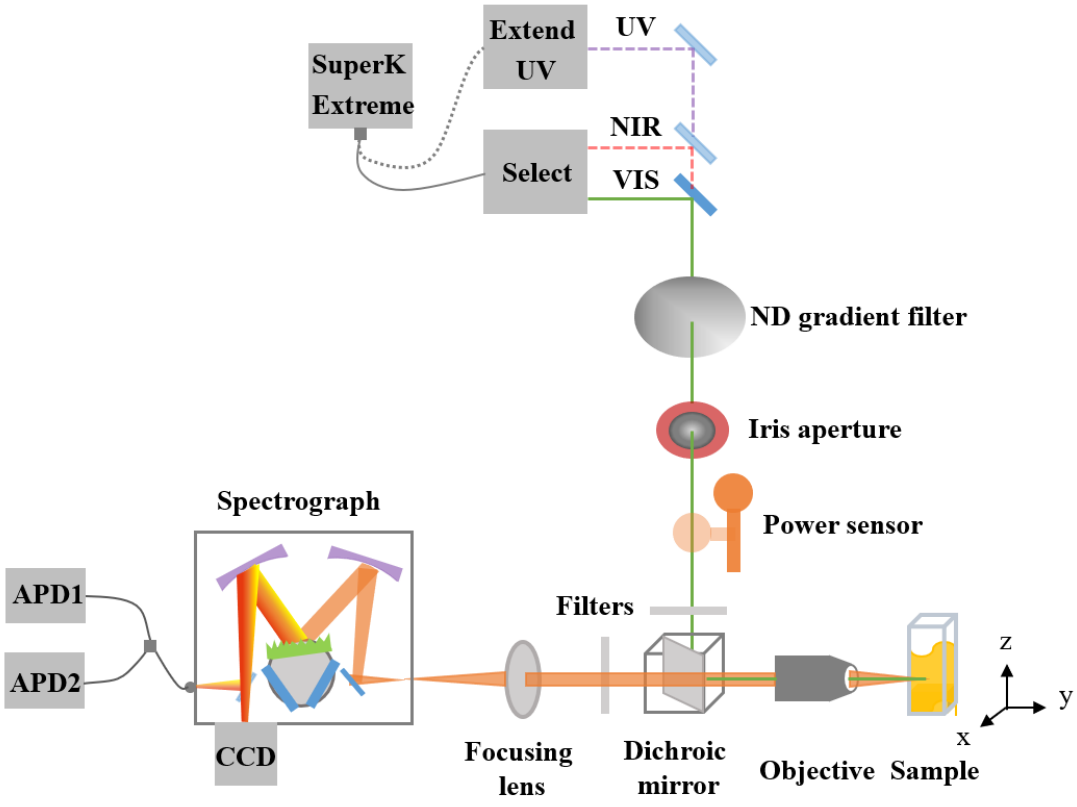

Figure 3.7: Working Principle of μ-PL Setup The laser beam with a selected wavelength outputs either from a *SuperK Extend-UV* or a *SuperK Select* modulator. It is directed by plane mirrors through a gradient ND filter and an iris aperture to modulate its purity and intensity. A power sensor fixed on a flip mount is connected to measure the laser power. Filtered by an excitation filter and a dichromic mirror, the light beam is focused via an objective on the sample. The position of the sample is tunable with a three-dimensional manual stage. The emission light is collected by the same objective, and passes through the dichroic mirror and an emission filter. Finally, the emitted photons enter a spectrograph. Here, a grating or a mirror are switchable with the grating turret to realize spectral detection and image acquirement, respectively. The observation of PL decay is achievable with a flip mirror directing the light beam to a fiber. The fiber is splited into two avalanche photodiodes (APDs) by a beamsplitter.

including contributions from the laser, detector, and other components. During the pulse duration, individual emitted photons from a sample are detected by an APD, and their time of arrival is correlated to the trigger of laser pulse. By counting many single-photon events, a histogram of the photon distribution over time is built up. Overall, the timing at the peak maximum of the IRF refers to the starting (zero) point of the time axis for the sample's decay curve.

To satisfy the precision of measurement, the repetition rate of laser needs to be controlled so that all charge carriers recombine within the laser period. Therefore, charge carrier recombination with lifetimes in the microsecond range can't be monitored. High excitation powers are not preferable which may cause more than one photon to be detected per excitation pulse. In this case, the second photon from the sample will not induce a second start/stop delay, and the overall decay process will be monitored with inaccuracy. To decrease possible errors, the laser beam is blocked before arriving at an APD to make sure that the count rate of detected laser photons is around 1% of the laser repetition rate (rule of thumb). It is noted that the IRF with a pulse width around 1 ns is incorporated in the overall PL decay, which is broader than the desired laser pulse width below 100 ps. For a sample whose lifetime is within several nanoseconds, the IRF needs to be considered. A deconvolution procedure is required to remove the instrument interference. In the thesis, the as-prepared LHP NPls own quite long lifetimes. Consequently, I omitted this step.

3.3 Photocatalytic Characterization

For the detection of photocatalytic products, an enclosed photoreactor with high light transmittance is required. Photocatalytic reactions are carried out inside the reactor, whose gaseous products are collected and detected by a gas chromatograph (GC). The collection of generated gases is divided into two ways. One is manual collection after accumulation for a certain period, and the average productivity is calculated on the basis of the reaction time. The other solution is real-time collection with a reactor connected to a GC. In my thesis, I used the first method with the help of a manual injector and a GC. The design of the employed photoreactors in my thesis, which I will describe in detail, is simple but exquisite.

3.3.1 Photocatalytic Setup

Preparation of a Pt-A(MA, Cs)$PbBr_3$ Specimen

A Pt-A(MA, Cs)$PbBr_3$ specimen is prepared for photocatalytic reactions and spectral characterization. I choose two different Pt sources, hexachloroplatinic acid hexahydrate ($H_2PtCl_6 \cdot 6H_2O$) and Platinum (II) bis(acetylacetonate) ($Pt(acac)_2$) to be chemically reduced or photo-reduced into Pt metal, respectively. For the photoreduction approach, $Pt(acac)_2$ dissolved in perovskite NPl colloidal solution is reduced into Pt nanoclusters by photogenerated electrons of perovskite NPls, forming Pt-A(MA, Cs)$PbBr_3$ mixture. The mixture is used for spectral characterization. The chemical reduction method utilizes ascorbic acid as a reductant. It is

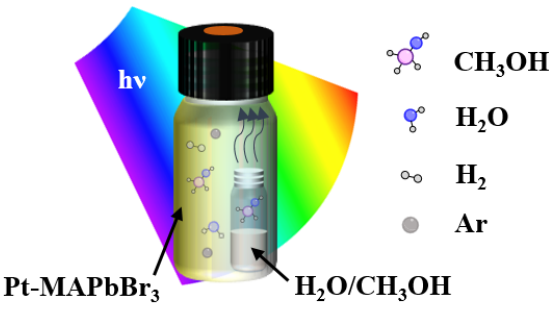

Figure 3.8: The Photocatalytic Reactor The schematic diagram shows how the reactor is designed for photocatalytic H_2 evolution of Pt-$MAPbBr_3$ NPls in H_2O/CH_3OH vapor. The reaction is carried out in an enclosed glass bottle of 20 mL, with a screwed plastic cap filled with a septum. Pt-$MAPbBr_3$ NPls are spread on the inner side wall of the bottle by spinning. A small glass vial containing a mixed solution of water and methanol is positioned inside the bottle. The reactor is purged with Argon inert gas to remove oxygen in case of side reactions. Under illumination, the solution inside the glass vial evaporates, forming an atmosphere of Ar, CH_3OH, H_2O mixture inside the big bottle. For detection, a needle is manually inserted into the bottle to extract gas through the septum for further analysis.

dissolved in methanol together with $H_2PtCl_6{\cdot}6H_2O$ and reacts with each other under sonication. The reaction products containing Pt nanoclusters and residual ascorbic acid are mixed with A(MA, Cs)$PbBr_3$ NPls colloidal solution, ready for photocatalytic activity measurements.

Design of a Photocatalytic Reactor

The study of photocatalytic hydrogen production reactions is performed in a cylindrical glass bottle of 20 mL with a screwed lid. Between the reactor and the lid is a silicon septum for sampling the gaseous products by a gas-tight syringe. A Pt-A(MA, Cs)$PbBr_3$ specimen is prepared in advance and evenly coated on the inner wall of the glass bottle by spinning. A glass vial containing a mixture (1 mL) of methanol and water is placed inside the reactor. It evaporates into steam under irradiation, which works as a proton source. Before illumination, the system is flushed with inert gas—Argon to remove air, in case of side reactions. A solar simulator (*LOT*, AM1.5) is used as a light source. A glass container filled with water is put between the reactor and the solar simulator to block infrared light, which removes the disturbance of heat. The reaction starts when the light source is activated to irradiate the surface of the reactor. A scheme of the photocatalytic setup is presented in Figure 3.8.

The volume ratio of methanol/water is tuned while keeping the total solution volume constant. For two-component solution systems in an enclosed space under vacuum, the partial pressures in vapor are influenced by their volume ratios. The concentration of methanol/water vapor in the reactor varies with its partial pressure. It is assumed that the temperature of the reactor is constant under irradiation, and the gas inside the reactor behaves sufficiently like an ideal gas (not taking into account the cross-association). The concentrations of methanol and water vapor under different conditions were calculated on the basis of the ideal gas law, shown in Table 3.1.

Table 3.1: Vapor-Liquid Equilibrium Data for Mixtures of Methanol and Water (Room Temperature). Calculated Using the Data of Ref.[142]

Methanol amount / mL	Methanol percentage (l) / %	Total pressure (v) / kPa	Partial pressure of methanol (v) / kPa	Methanol concentration (v) / μmol/mL	Partial pressure of water (v) / kPa	Water concentration (v) / μmol/mL	Methanol percentage (v) / %
0	0	3.17	0	0.00	3.17	1.28	0
0.25	25	8.18	5.66	2.28	2.52	1.02	69.2
0.5	50	11.15	9.28	3.75	1.87	0.75	83.2
1	100	16.85	16.85	6.79	0	0.00	100

3.3.2 Hydrogen Detection

For detection, gas aliquots from the headspace are sampled every hour once the process is initiated. A gas-tight syringe with a scale of 10 µL is inserted inside the reactor headspace, and an aliquot of 10 µL reactant gas is taken after purging the syringe several times. The reactant gas is quickly injected into a GC (*GC2014*, *Shimadzu*) through its injector by vertically pushing the syringe plunger to the end.

A GC is a common type of chromatography, for the isolation and analysis of vaporized compounds carried by a continuous gas flow. A GC system has three main components: a sample injection unit for heating and vaporizing the analyte gas; a column for separating each component; a detector for qualitative and quantitative analysis. The mobile phase, referred to as the carrier gas, passes by the sample injection unit, the column and the detector in sequence under heating.

For the *GC2014* system in our lab, argon as a carrier gas is stored in a cylinder and connected to the GC via valves. A carrier gas flow controller is set inside the GC system for adjusting the flow speed. Through a dual-packed sample injection unit, the analyte gas is manually injected into the machine by a syringe. It is heated and vaporized at 80 ℃, transported by the carrier gas to a column. The column is made of a narrow tube containing a stationary phase, which can be particulate packing material or liquid. The column is enclosed by a column oven for heating (40 ℃). The column tube has a small internal diameter (2-4 mm

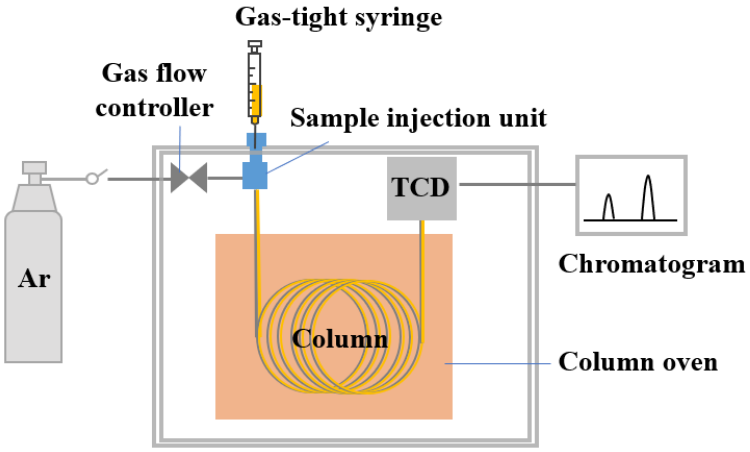

Figure 3.9: A GC system The schematic diagram shows the main components of our *GC2014* system. When analyte gas is injected into the chromatography via a gas-tight syringe, it is heated and vaporized within the sample injection port. The analyte gas is carried by Argon as a carrier gas, enters the column heated by a column oven. The column comprises a extralong and thin tube filled with solid or liquid stationary phase. In the column, various components of the target gas are separated due to different thermal conductivities. They arrive at the thermal conductivity detector (TCD) at different retention times, which is a signal for identification. The TCD converts temperature variation into electrical signals, and sends these signals to a data processing unit for quantitative analysis.

for packed column; 0.1-0.53 mm for capillary column) and a large length (0.5-5 m for packed column; 5-100 m for capillary column). Here, different components from the analyte gas are isolated because of their physicochemical properties and different interaction effects with the column lining or filling. Finally, the components exit the column at different time points, which is then monitored by a TCD. The TCD converts the fluctuation of thermal conductivity of analyte molecules to electrical signals, which are output for data processing.

The result is presented by a chromatogram, with the retention time as x-axis and the detector response as y-axis. The retention time defines the time interval since the analytes are injected until they are detected after eluting from the column at different times. It is a parameter used to identify analytes. Under the method conditions in our lab, the retention time of H_2 is around 1.4 minutes, O_2 is around 2.0 minutes, and N_2 is around 2.5 minutes. The peaks of these gas analytes show up in sequence at different retention times. The peak area is proportional to the amount of the corresponding analyte. For quantitative analysis, a calibration curve (usually in the form of $y = ax + b$) is built to determine the response factor (a) by testing the peak areas of a standard analyte with known amounts. The concentration of the analyte is determined by integration and calculation based on the calibration curve.

4

$MAPbBr_3$ Nanoplatelets for Photocatalytic H_2 Evolution: in Polar Vapor

The outstanding physicochemical properties of lead halide perovskite (LHPs) have made them a hotspot among optoelectronic applications,[8] including solar cells,[143] light-emitting diodes (LEDs),[143,144] photodetectors,[145] as well as photo- and electrocatalysis.[146] However, their instability in polar solvents limits their application in photocatalytic hydrogen production.[13,147] In this chapter, a "polar vapor" concept is proposed to investigate whether halide perovskites can remain stable and potentially generate hydrogen in a polar vapor environment under simulated solar irradiation.

In this chapter, methanol and water vapor are employed as proton sources for photocatalytic hydrogen evolution on lead bromide perovskites. In Section 4.1, I demonstrate successful photoinduced hydrogen generation from methanol/water vapor using Pt decorated $MAPbBr_3$ nanoplatelets (NPls), which exhibit superior hydrogen evolution rates (HERs). The activity is further optimized by tuning the vapor constituents. Additionally, the performance of Pt-$CsPbBr_3$ NPls is evaluated for comparison with different perovskite systems. In Section 4.2, I investigate the electron transfer dynamics from $MAPbBr_3$ NPls to their surface-attached Pt clusters using time-resolved photoluminescence (PL) and transient absorption spectroscopy (TAS). A model describing the distribution of charge carrier diffusion times is developed. Finally, in Section 4.3, I present the long-term stability of hydrogen production and the regeneration characteristics of $MAPbBr_3$ NPls under polar vapor conditions.

4.1 The “Polar Vapor” Concept Works

Photoinduced-hydrogen generation of LHPs in methanol/water vapor has been investigated in this section. A(MA, Cs)$PbBr_3$ NPls are used due to their facile scalable synthesis and large specific-surface-areas. The preparation of A(MA, Cs)$PbBr_3$ NPls and their specimens for photocatalytic reactions is described in Subsection 3.3.1. Control experiments are prerequisites for photocatalytic measurements to ensure that the observed results originate solely from photocatalytic reactions, not from side reactions. In the absence of $APbBr_3$/Pt/methanol and water, no hydrogen was detected through *GC-2014*. This demonstrates that photocatalysts/cocatalysts/proton sources are necessary for hydrogen evolution in the reactions under simulated solar light.

4.1.1 Vapor Constituents Influencing Hydrogen Evolution Rates

As shown in Figure 4.1, hydrogen evolution rates (HERs) of Pt-$MAPbBr_3$ NPls in methanol/water vapor have been evaluated. When Pt-$MAPbBr_3$ NPls are exposed to water vapor (1.3 µmol/mL, v/v), a tiny amount of hydrogen is detected over four hours, with a stable HER of 23 $\mu mol \cdot g^{-1} \cdot h^{-1}$. Methanol as a promising proton source is also tested because of its high saturated vapor pressure. In pure methanol vapor (6.7 µmol/mL, v/v), a significantly higher HER of 424 $\mu mol \cdot g^{-1} \cdot h^{-1}$ is obtained. The results suggest that classical polar proton sources, such as methanol and water, can be applied for hydrogen production **in vapor** on LHPs. Methanol/water mixtures are also employed to investigate the influence of vapor constituents on HERs. When the methanol volume ratio ($V_{methanol}/V_{mixture}$) in the liquid phase increases

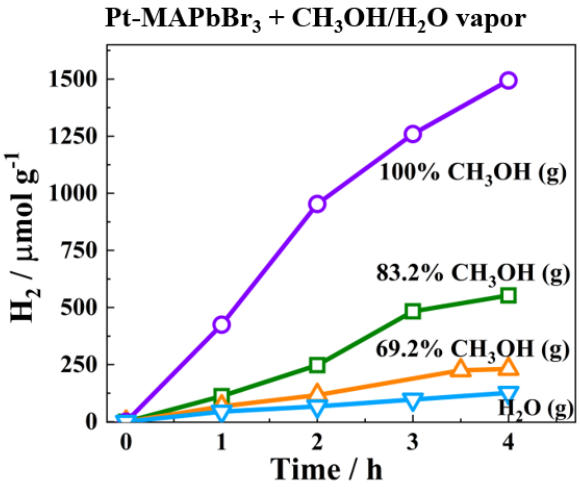

Figure 4.1: HERs of Pt-$MAPbBr_3$ in Methanol/Water Vapor The legends show the proportion of methanol in the vapor phase. The corresponding concentrations could be found in Section 3.3. The data is acquired from *GC-2014* after calibration. The samples are illuminated under a stimulated solar light with Air Mass 1.5.

from 0% to 25%, 50%, and 100%, its corresponding volume ratio in steam inside the reactor increases from 0% to 69.2%, 83.2%, and 100%, respectively. With $V_{methanol}/V_{mixture}$ in vapor rising (Figure 4.1), the HERs on Pt-$MAPbBr_3$ improves from 64 $\mu mol \cdot g^{-1} \cdot h^{-1}$ at 69.2% (v/v, 2.3 µmol/mL methanol) to 164 $\mu mol \cdot g^{-1} \cdot h^{-1}$ at 83.2% (v/v, 3.7 µmol/mL methanol). The result shows that methanol reforming reactions are advantageous over water splitting reactions under the conditions employed. This may be attributed to methanol's high saturated vapor pressure and its dual role in the reactions. Methanol acts as both a proton source and a sacrificial agent.

Figure 4.2 illustrates the mechanism of methanol reforming at the solid-gas interface. Upon illumination, electrons are excited to the CB of perovskite NPls, which subsequently transfer to surface-attached Pt clusters due to the overpotential between them. Electrons trapped in the Pt clusters react with surface-adsorbed CH_3OH molecules and reduce their protons into H_2. Simultaneously, holes in the CB of perovskites diffuse to the surface of NPls. The holes oxidize surface-adsorbed CH_3OH molecules or intermediates into formaldehyde after a series of reactions. Combining two half reactions, the full reaction is obtained:

$$CH_3OH \xrightarrow{\text{photocatalysis}} HCHO + H_2 \tag{4.1}$$

The solid-gas interfaces mitigate the limitations associated with the use of fragile perovskite materials in photocatalytic hydrogen production. This concept can also be applied to other halide perovskites. In the following subsection, I will investigate the photocatalytic activity of cecium-based LHPs for comparison.

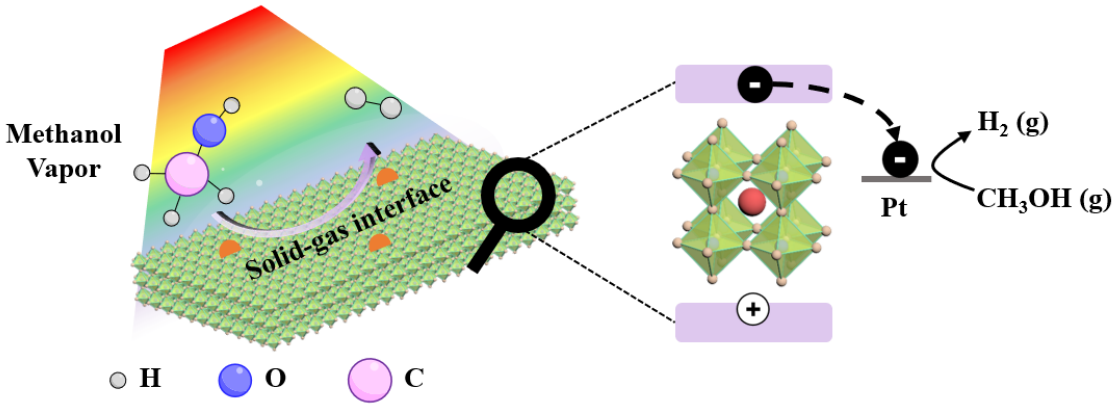

Figure 4.2: Illustration of Photocatalytic Hydrogen Production of LHP NPls in Methanol Vapor On the left, the diagram illustrates methanol reforming at the solid-gas interface. The two molecules represent methanol (CH_3OH) and hydrogen (H_2), respectively. On the right, the reaction mechanism is depicted. The black and white spheres represent an electron and a hole, respectively. The purple lines indicate the minimum of the CB and the maximum of the VB for the perovskite. The gray line represents the potential of the Pt clusters.

4.1.2 Nanoplatelet Thicknesses Influencing Hydrogen Evolution Rates

$CsPbBr_3$ NPls are synthesized and decorated with platinum for hydrogen evolution, following a similar procedure to that used for $MAPbBr_3$ NPls (Chapter 3). In Figure 4.3a, Pt-$CsPbBr_3$ NPls exhibits a stable HER of 28 $\mu mol \cdot g^{-1} \cdot h^{-1}$ over four hours in the vapor containing 69.2% methanol, which is lower than the 63 $\mu mol \cdot g^{-1} \cdot h^{-1}$ observed for Pt-$MAPbBr_3$ NPls under the same conditions.

To elucidate the activity differences between Pt-$MAPbBr_3$ and Pt-$CsPbBr_3$ NPls, steady-state spectroscopy is conducted on their pristine materials. Figure 4.4a shows UV-Vis and PL spectra of $MAPbBr_3$ and $CsPbBr_3$ NPls. The UV-Vis spectra display an absorption onset at 544 nm for $MAPbBr_3$ NPls and at 537 nm for $CsPbBr_3$ NPls, which are attributed to optical transitions at the direct bandgap extrema in their bulky phases. It is followed by a continuous increase in signal intensity and several absorption peaks. The multiple excitonic peaks are attributed to NPls with 1, 2, etc., monolayers whose thicknesses are smaller than the corresponding Bohr radii (2 nm $MAPbBr_3$, 3.1 nm for $CsPbBr_3$). The thickness of these NPls is quantized and a multiple of one monolayer thickness, leading to discrete excitonic peaks. As reported, the absorption peaks of $MAPbBr_3$ at 430, 451, and 470 nm correspond to 1, 2, and 3 monolayers, respectively.[54] For $CsPbBr_3$ NPls, the absorption peaks at 456 and 476 nm correspond to 3 and 4 monolayers, respectively.[55] The results indicate that as-synthesized $MAPbBr_3$ and $CsPbBr_3$ nanostructures consist of a mixture of thick plates and thin NPls. From absorption spectra, it is concluded that $MAPbBr_3$ owns a larger proportion of thinner NPls overall compared to $CsPbBr_3$. Moreover, the PL spectra exhibit prominent bands centered at 531 nm for $MAPbBr_3$ NPls and at 520 nm for $CsPbBr_3$ NPls, which is attributed to excitonic recombination of thicker NPls.

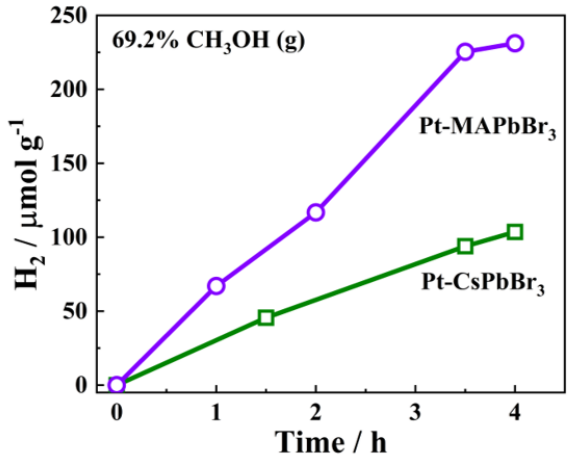

Figure 4.3: HERs of Pt-$CsPbBr_3$ and Pt-$MAPbBr_3$ NPls in Vapor The hydrogen evolution performance is evaluated under the same conditions. The reactions occur in the vapor containing 69.2% methanol under a stimulated solar light with Air Mass 1.5. The data is acquired from *GC-2014* after calibration.

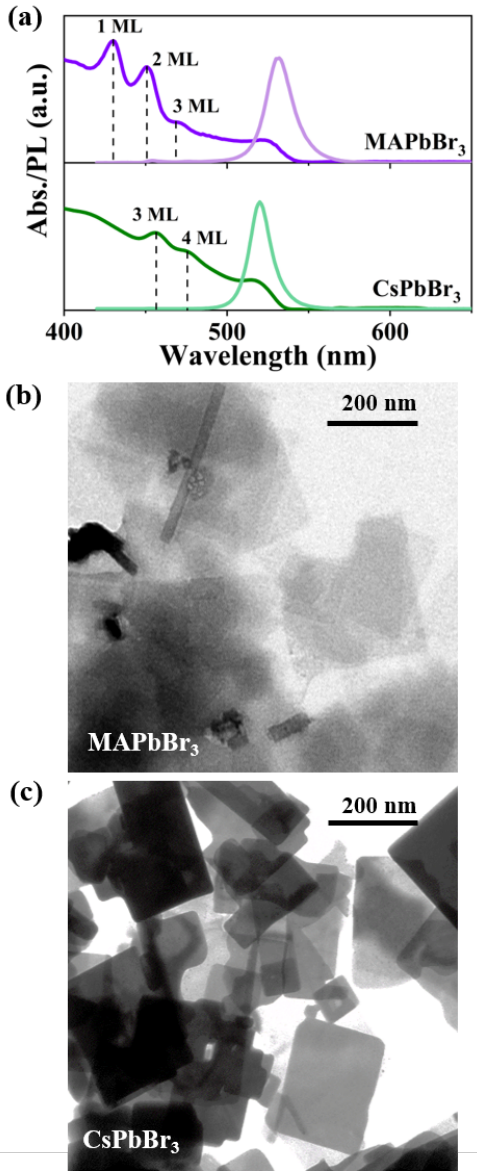

Figure 4.4: Comparison of $MAPbBr_3$ and $CsPbBr_3$ NPls (a) UV-Vis and PL spectra (365 nm laser excitation) of $MAPbBr_3$ and $CsPbBr_3$ NPls dispersed in hexane. **(b)** and **(c)** show their TEM images with a scale bar representing a length of 200 nm .

The conclusion is further supported by TEM characterization. Figure 4.4b and c display NPls with large lateral sizes. Based on the contrast of TEM images, it is apparent that the NPls of $MAPbBr_3$ are generally thinner than those of $CsPbBr_3$. The thinner NPls possess a larger surface-to-volume ratio, leading to more surface active sites for phtotcatalytic reactions. This explains the better mass-specific hydrogen evolution performance observed for Pt-$MAPbBr_3$ NPls compared to Pt-$CsPbBr_3$ NPls.

In this section, it has been demonstrated that, with the "vapor" concept, LHPs can be applied for photocatalytic hydrogen generation. The HERs of Pt-$MAPbBr_3$ NPls are influenced by their vapor constituents. Besides, photocatalytic activity varies among lead bromide

perovskites with different “A site” cations in the perovskite structure, owning to their NPl thickness differences. In the next section, I will look into the solid-gas interface to investigate the charge carrier transfer dynamics.

4.2 Exciton Diffusion to Pt Dominates Electron Transfer Dynamics

In our case, control experiments have demonstrated that Pt cocatalyst is essential for hydrogen evolution at the solid-gas interface. Pt, a noble metal with a low Fermi level, forms the Schottky junction with a semiconductor at their interface. It typically acts as an electron acceptor from the semiconductor under illumination. In this section, I will investigate electron transfer dynamics from $MAPbBr_3$ NPls to Pt nanoclusters over different time scales.

4.2.1 Electron Transfer on the Nanosecond Time Scale

The Pt decoration method is described in Section 3.3. In Figure 4.5, steady-state and time-resolved PL of $MAPbBr_3$ NPls with and without Pt decoration are compared. In the presence of Pt nanoclusters, the PL of $MAPbBr_3$ NPls experiences a significant reduction in intensity, with no shape and position changes observed. Notably, approximately one-tenth of the PL intensity is retained, suggesting efficient electron transfer from NPls to Pt metal.

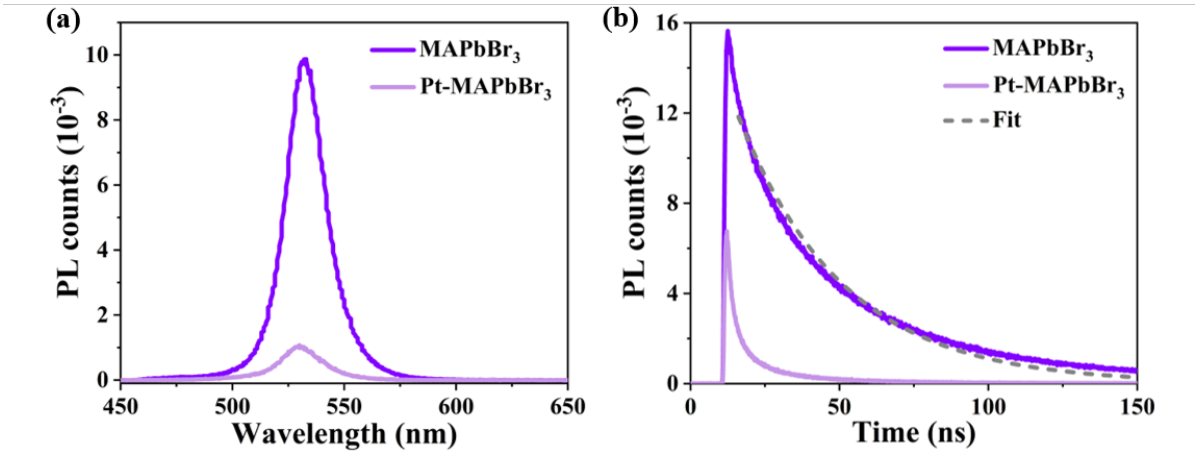

Figure 4.5: Steady-State and Time-Resolved PL of $MAPbBr_3$ and Pt-$MAPbBr_3$ NPls (a) Steady-state PL spectra (400 nm excitation) of $MAPbBr_3$ and Pt-$MAPbBr_3$ NPls with the same optical density. The NPls were dispersed in hexane. **(b)** PL recombination dynamics were recorded by TCSPC upon excitation at 400 nm. The grey dashed curve was the fiiting results to model the monoexponential PL decay (purple line).

In Figure 4.5b, the time-resolved PL of pristine $MAPbBr_3$ NPls displays a mono-exponential decay. After fitting (as shown by the grey dashed line in Figure 4.5a), an average lifetime

τ_{rec} of 35.3 ns is obtained. The PL decay of Pt-$MAPbBr_3$ NPls is much faster than that of the pristine NPls. In addition, the spectrum initially loses a significant amount of intensity due to the limited time resolution of the -PL setup. It is well-established that electron transfer from a semiconductor to its attached Pt nanoclusters typically occurs on a picosecond or sub-picosecond timescale,[148] much faster than what is observed in this measurement.

4.2.2 A Distribution of the Diffusion Time

Considering the two dimensional NPl structure and the sparse distribution of Pt nanoclusters on the surface, the observed PL behavior is attributed to the combination of longer-lasting exciton diffusion and subsequent rapid electron transfer. As shown in Figure 4.6, excitons photoexcited in the vicinity of a Pt cluster will experience an electron transfer in a short time. However, for excitons photoexcited far away from a Pt cluster, it will take time to reach such a cluster. Furthermore, as excitons diffuse within the NPls, they may recombine radiatively or nonradiatively, in addition to undergoing an electron transfer. Two other processes are schematically illustrated in Figure 4.6: ① An exciton recombines radiatively, emitting a photon; ② An exciton is trapped by a defect. Hence, exciton diffusion may dominate the dynamics of electron transfer to Pt clusters, thus the decay dynamics of PL.

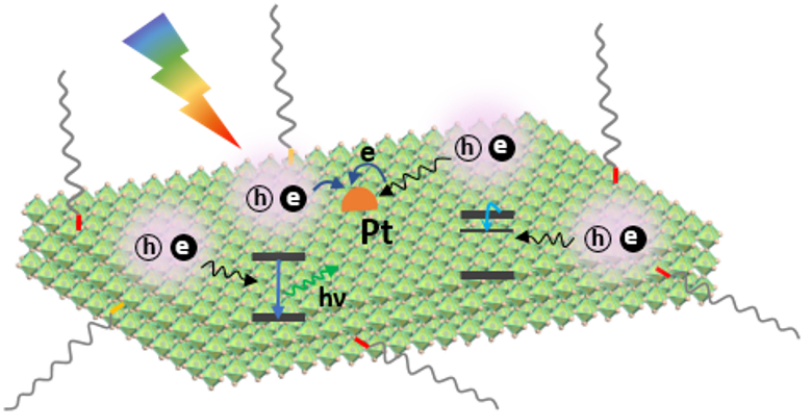

Figure 4.6: Illustration of the Pathways for Photoinduced Excitons The diagram shows different pathways of photoexcited excitons within $MAPbBr_3$ NPls. From left to right, four processes are schematically depicted: ① An exciton recombines radiatively, emitting a photon; ② An exciton photoexcited near a Pt cluster, has its electron rapidly trapped by the cluster; ③ An exciton located far from the Pt cluster diffuses within the NPl and is eventually trapped by the Pt cluster; ④ An exciton is trapped by a defect.

Accordingly, I assume a distribution of diffusion times $G(\tau_D)$ with a maximum diffusion time $\tau_{D,\,max}$ given by the size and geometry of the NPl and/or the concentration of Pt clusters. It is assumed that the distribution function $G(\tau_D)$ for diffusion times τ_D decays exponentially

with increasing τ_D values:

$$G(\tau_D) = \exp(-\frac{\tau_D}{\tau_{D,\,max}}) \tag{4.2}$$

As discussed previously, this function models the loss of excitons during their migration to Pt clusters. An upper limit for the diffusion time is given by the recombination time of excitons τ_{rec} in $MAPbBr_3$ NPls. Once excitons have reached the direct vicinity of a Pt cluster, an ultrafast electron transfer to the Pt cluster is assumed with a time constant $\tau_{transfer}$. Based on these assumptions, the time-resolved PL of Pt-$MAPbBr_3$ can be effectively modeled using the following equation:

$$PL(t) \propto \exp(-\frac{\tau}{\tau_{rec}}) \cdot \int_{\tau_{transfer}}^{\tau_{rec}} G(\tau_D) \cdot \exp(-\frac{\tau}{\tau_D}) d\tau_D \tag{4.3}$$

Here, τ_{rec} is determined as 35.3 ns from the time-resolved PL of $MAPbBr_3$ NPls without Pt decoration. The ultrafast electron transfer time $\tau_{transfer}$ is assumed as 3 ps.[148] Therefore, the integration range for the diffusion integral in Equation 4.3 is from $\tau_{transfer}$ = 0.003 ns to τ_{rec} = 35.3 ns. The only fitting parameter left for the $PL(t)$ curve of Pt-modified $MAPbBr_3$ NPls is $\tau_{D,\,max}$.

As illustrated in Figure 4.7, a $\tau_{D,\,max}$ value of 7.7 ns results in a near-quantitative agreement between the experimentally obtained $PL(t)$ curve and the one calculated using Equation 4.3. Specifically, an R-squared value of 0.996 is obtained from the fitting procedure. The obtained value for the maximum diffusion time ($\tau_{D,\,max}$ = 7.7 ns) is smaller than the recombination time τ_{rec} = 35.3 ns for excitons in pristine $MAPbBr_3$ NPls. The exciton diffusion length is

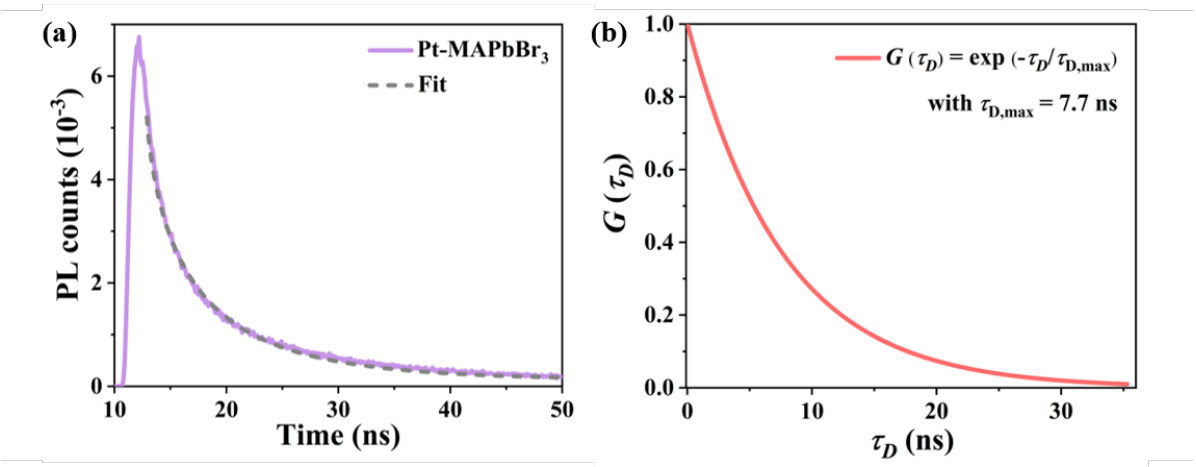

Figure 4.7: Fitting of the PL Decay for Pt-$MAPbBr_3$ NPls (a) The PL decay of $MAPbBr_3$ NPls was measured using TCSPC under 400 nm excitation. The grey dashed curve represents the fitting results based on Equation 4.3 with the distribution of diffusion time shown in Figure 4.7b. **(b)** The distribution funtion $G(\tau_D)$ with respect to diffusion time τ_D with the maximun diffusion time $\tau_{D,\,max}$ as 7.7 ns. It is acquired from modeling and fitting using *Python 3.7* and *Spyder IDE 5.5.0*.

estimated to be around 300 nm. It shows that the maximum diffusion time must be limited by the size/geometry of the NPls and/or the Pt deposition concentration.

4.2.3 Electron Transfer on the Picosecond Time Scale

To elucidate the ultrafast electron transfer process, femtosecond TAS is performed as the time-resolved PL setup has a limited time resolution. Figure 4.8a shows transient absorption spectra of $MAPbBr_3$ under the excitation of 400 nm with time delays ranging from 1 ps to 2 ns. It is observed that there are multiple positive and negative peaks for every spectrum trace. The negative differential absorption signals (bleaching) are attributed to phase-space filling of excitons in NPls with various thicknesses as well as the bulk phase,[149] which are consistent with their absorption spectra. Apart from the bleaching signal, several positive

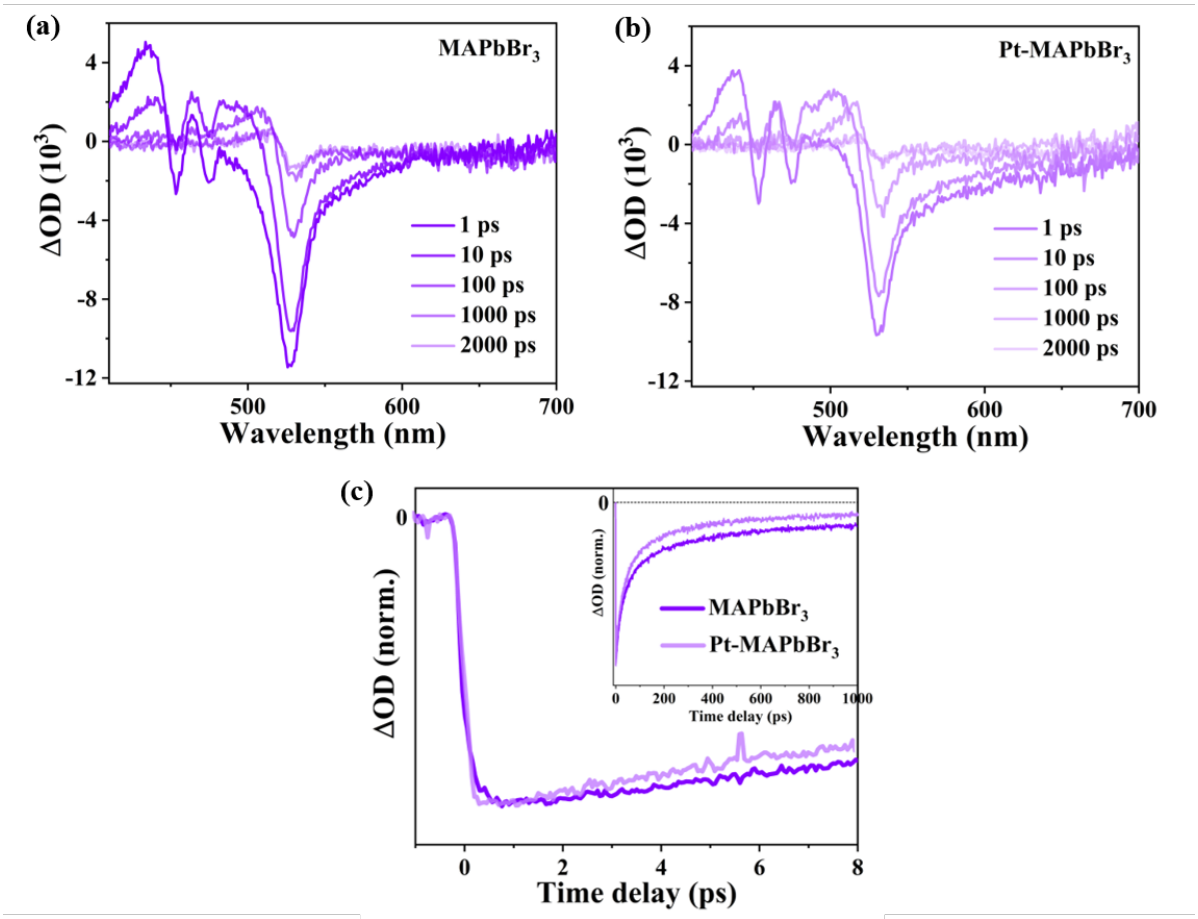

Figure 4.8: Transient Absorption Spectra of $MAPbBr_3$ and Pt-$MAPbBr_3$ NPls Transient absorption spectra of **(a)** $MAPbBr_3$ and **(b)** Pt-$MAPbBr_3$ NCs upon excitation at 400 nm under different delay times (1 ps, 10, ps, 100 ps, 1 ns, 2 ns). **(c)** Comparasion of the bleach dynamics at the bleach maxima of the bulk phases (527 nm for $MAPbBr_3$ and 530 nm for Pt-$MAPbBr_3$) during the first 8 ps, after normalization. The insert shows the same bleach decay curves over a longer time scale (1 ns).

signals (induced absorption) at different energies are observed. Figure 4.8b displays transient absorption spectra of Pt-$MAPbBr_3$ NPls, which closely resemble those of pristine $MAPbBr_3$ NPls.

To compare the bleach decay dynamics, the transient traces at the bleaching maxima (around 528 nm) of the bulk phases in Figure 4.8a and b are plotted in Figure 4.8c. As shown in the inset, Pt-$MAPbBr_3$ NPls exhibits a faster bleach decay within 1 ns compared to $MAPbBr_3$ NPls. The faster decay of charge carriers in Pt-$MAPbBr_3$ NPls is consistent with the time-resolved PL results and provides complementary insight on a shorter timescale. To further investigate the charge carrier decay dynamics, the initial few picoseconds of the transient traces are enlarged in Figure 4.8. Within the first picosecond after pump-pulse excitation, both spectra display an ultrafast bleach growth, which is attributed to hot carrier cooling from higher excited states.[150] This is followed by a continuous bleach decay, leading to the appearance of a transient maximum. Compared to pristine $MAPbBr_3$ NPls, the bleach growth in Pt-$MAPbBr_3$ NPls reaches its maximum in a shorter time. It indicates ultrafast electron transfer from CB energy levels of $MAPbBr_3$ to Pt, occurring on a picosecond or even sub-picosecond timescale.

In summary, time-resolved PL and TAS demonstrate that the overall process of exciton diffusion and subsequent electron transfer from NPls to Pt takes place on different time scales, spanning from picoseconds to nanoseconds. The efficient electron transfer from $MAPbBr_3$ to Pt cocatalysts significantly enhances the utilization of photoexcited electrons, thereby promotes the photocatalytic HER process.

4.3 Photocatalytic Stability and Versatility of $MAPbBr_3$ Nanoplatelets

4.3.1 Photocatalytic Stability of $MAPbBr_3$ Nanoplatelets

Photocatalysis stability is a key factor in evaluating a superior photocatalyst, and it is even more crucial when assessing fragile halide perovskite photocatalysis. In the last section, I have demonstrated that LHPs are stable in methanol/water vapor, exhibiting good HERs. Now, a question arises: how stable are they while maintaining the activity?

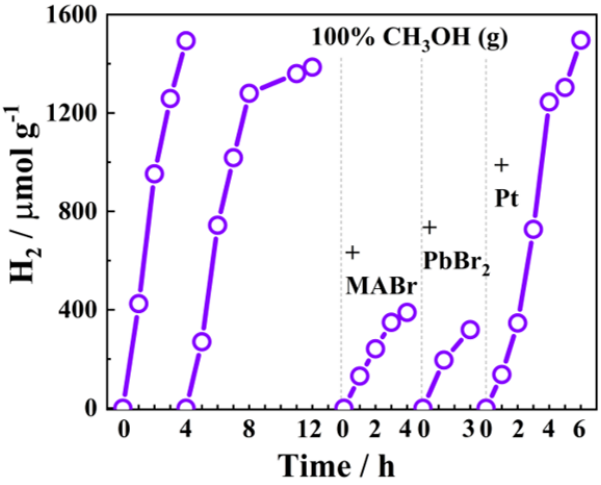

Figure 4.9: Photocatalytic Stability of Pt-$MAPbBr_3$ NPls Photocatalytic stability was assessed through repeated measurements under the same conditions. Every six hours, the reactor was re-purged with argon to remove H_2 and other products. Regeneration experiments were performed by adding MABr, $PbBr_2$ or a Pt precusor to the collected reactants. The mixture was coated inner wall of the reactor again, and the specimen was placed under light after purging. The experiments were conducted in a pure methanol stream.

Repeated experiments on hydrogen production of Pt-$MAPbBr_3$ NPls were conducted every six hours in pure methanol vapor. As shown in Figure 4.9, a robust activity of around 400 $\mu mol \cdot g^{-1} \cdot h^{-1}$ is maintained until the 10th hour. After 10 hours, the activity begins to decrease. Ths decline could be attributed to several factors, such as surface degradation or ion migration, which result in the formation of surface defects.

It has been reported that introducing 'A' or 'B' cation-containing salts can help repair surface defects, such as bromide and lead vacancies in the NPls.[55,151] I collected the reactants and coated it inner the reactor again after adding a certain amount of MABr salt. The activity improves, although only a quarter of the original HER (100 $\mu mol \cdot g^{-1} \cdot h^{-1}$) is recovered. $PbBr_2$ salt was also employed for regeneration. Silimar to MABr, its effect is not as significant. Moreover, additional Pt nanoclusters were added to the reactant for repeated measurements. Surprisingly, the HER fully recovers to 360 $\mu mol \cdot g^{-1} \cdot h^{-1}$ and remains stable for six hours.

This suggests that the detachment or reduced contact of Pt with NPls is one contributing factor for their long-term instability. With effective recycling techniques, LHPs can potentially be employed for long-term hydrogen evolution in polar environments.

4.3.2 Photocatalytic Versatility of $MAPbBr_3$ Nanoplatelets

Instead of employing a solid-liquid interface, a solid-gas interface for perovskite photocatalysis has been utilized and found to be effective. Solid-solid interface reactions also present potential alternatives for perovskite photocatalysis. The use of a solid proton source not only enhances charge separation at the interface but also improves photocatalytic stability.

Biomass is a renewable resource that can be harvested sustainably from plants, algae, and agricultural or forestry residues. Using biomass for photocatalytic hydrogen production aligns with the principles of green chemistry, offering a more environmentally friendly alternative to fossil fuels. Biomass contains a variety of organic compounds, such as sugars, lignin, and cellulose, which can be utilized in photocatalytic systems to generate hydrogen. For example, biomass-derived organic molecules can serve as electron donors, participating in light-driven hydrogen production reactions.

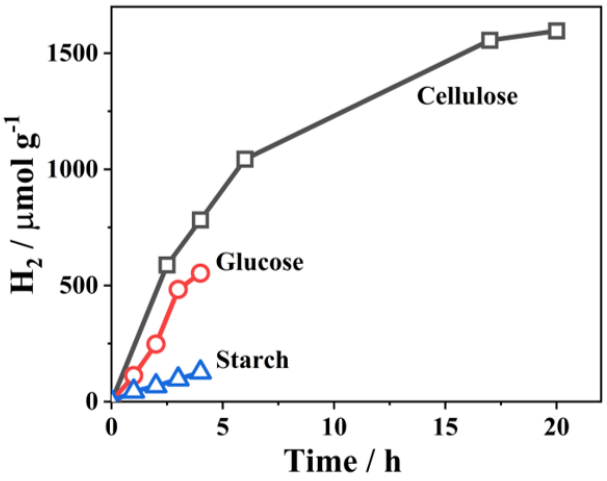

Figure 4.10: Photocatalytic Hydrogen Production of Pt-$MAPbBr_3$ NPls from Biomass
The experiments were carried out under the same conditions. Instead of using a glass vial containing methanol/water solvents, a certain amount of biomass (cellulose, glucose, starch) was added to a Pt-$MAPbBr_3$ mixture. The mixture was evenly spread as a film on the inner surface of a glass bottle and the reactor was then placed under light.

In this work, several biomass materials, including cellulose, glucose, and starch, have been tested on Pt-$MAPbBr_3$ NPls for hydrogen production (Figure 4.10). It is observed that all three proton sources work, indicating that LHPs with tunable bandgaps and high charge carrier densities are promising for solar-to-hydrogen conversion with the proposed non-liquid strategy. Specifically, hydrogen is produced at a rate of 266 $\mu mol \cdot g^{-1} \cdot h^{-1}$ from cellulose,

138.2 µmol · g^{-1} · h^{-1} from glucose, and 31.6 µmol · g^{-1} · h^{-1} from starch on Pt-$MAPbBr_3$ NPls.

It is noted that the biomass used here functions not only as a proton source but also as a sacrificial agent for photoexcited holes. The reaction mechanism with glucose as an example is schematically shown in Figure 4.11. Upon excitation, electrons in the VB of the perovskite rapidly transfer to Pt, where they reduce a glucose molecule at the interface to H_2 through series of reactions. Holes left in the VB oxidize the intermediate products into carbon-based products with low formation energies. With this approach, perovskites are suitable not only for reforming of gas-phase proton sources but also for solid ones. The observed HER using solid glucose is 63% of that achieved with methanol vapor (424 µmol · g^{-1} · h^{-1}). In the all-solid-state system, poor mass transfer between proton sources and catalysts limits their activity compared to the gas-solid-state system.

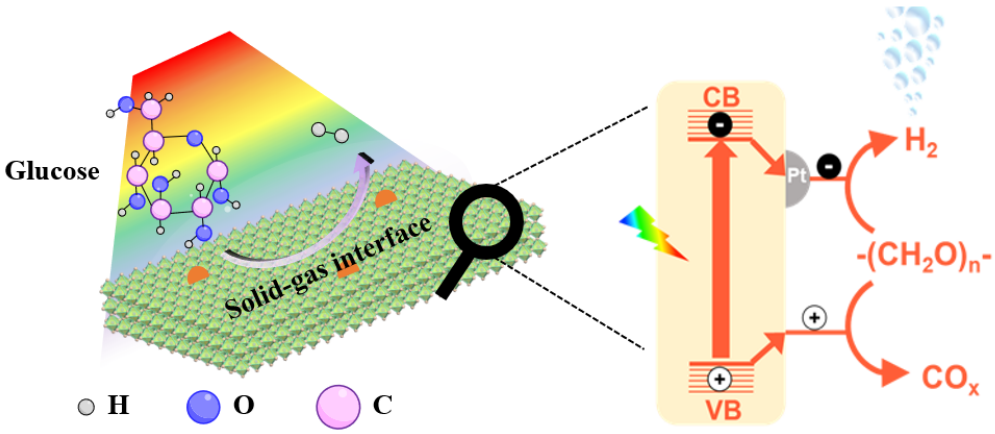

Figure 4.11: Illustration of Photocatalytic Hydrogen Production of LHP NPls from Biomass The diagram illustrates hydrogen generation from glucose at the solid-solid interface. The two molecules represent glucose and hydrogen (H_2), respectively. The reaction mechanism is enlarged and depicted on the right side. The black and white spheres represent an photoexcited electron and hole, respectively. The orange lines indicate energy levels of the CB and the VB for perovskites. The gray half sphere represents Pt clusters, where the reduction half-reaction occurs. The arrow at the bottom indicates the other half reaction-glucose is oxidized into carbon products.

In summary, it is demonstrated for the first time that LHP NPls decorated with a Pt cocatalyst can produce hydrogen from polar vapor (methanol, water) and biomass under light, even without specific encapsulation. This reaction could proceed robustly in the methanol vapor for 20 hours, achieving an optimized HER of 424 µmol · g^{-1} · h^{-1}. The HERs are influenced by vapor constituents and NPl thickness among different perovskites. Time-resolved spectroscopic investigation suggests that the diffusion-limited feeding of electron-hole pairs towards Pt clusters dominates the dynamics of charge transfer. This study provides a fundamental understanding of halide perovskite photocatalysts and outlines steps towards

their direct application in stable light-driven reactions in the non-liquid phase, promising advancements in photocatalysis through ingenious designs.

5

$Cs_2AgBiCl_6$ Nanocrystals with a Spectrally Broad Emission: the Role of Silver

Halide double perovskites (DPs) are emerging semiconductors for optoelectronic applications since they offer less toxic alternatives compared to lead halide perovskites (LHPs).[19] Cs_2AgBiX_6 (X = Br, Cl) as one of the first demonstrated bismuth-based DPs, has shown potential applications in photovoltaics,[20] X-ray detection,[152] and photocatalysis.[153] Although exhibiting an indirect bandgap, $Cs_2AgBiCl_6$ colloidal DP nanocrystals (NCs) show bright photoluminescence (PL) spectra characterized by a spectrally broad red emission centered around 650 nm and a narrower blue emission band centered at 425 nm. However, the origin of both emission bands is still under debate.

In this chapter, it is shown that silver plays a crucial role in both emission bands observed in $Cs_2AgBiCl_6$ DP NCs. In Section 5.1, I explain the presence of silver vacancy-bound excitons with an extralarge binding energy, which is fundamental for understanding the optical properties of $Cs_2AgBiCl_6$ NCs. In Section 5.2, the red emission is investigated in depth using temperature-dependent PL measurements. A model has been developed to extract the activation energy of silver vacancies. Section 5.3 reveals the nature of blue PL, which is related to surface additives of NCs. The surface chemistry of perovskite NCs is demonstrated to play a vital role in determining their optoelectronic properties as well as their stability.

5.1 Defect Bound Excitons with a Large Binding Energy

Spheroidal $Cs_2AgBiCl_6$ NCs with variable sizes (12 nm, 15 nm, 22 nm) have been synthesized based on the hot injection method described in Subsection 3.1.2. The optical properties of as-synthesized $Cs_2AgBiCl_6$ NCs are discussed here. Figure 5.1a shows the linear absorption spectrum of 15 nm DP NCs. Three different optical transition regions are identified based on the energy diagram in Figure 5.1b. The absorption spectrum starts with an onset at 445 nm, ascribed to indirect optical transitions, followed by a pronounced excitonic peak at 369 nm. Toward shorter wavelengths, it continues with an increasing signal corresponding to direct optical transitions. It is noted that the size of these DP NCs is larger than their exciton Bohr

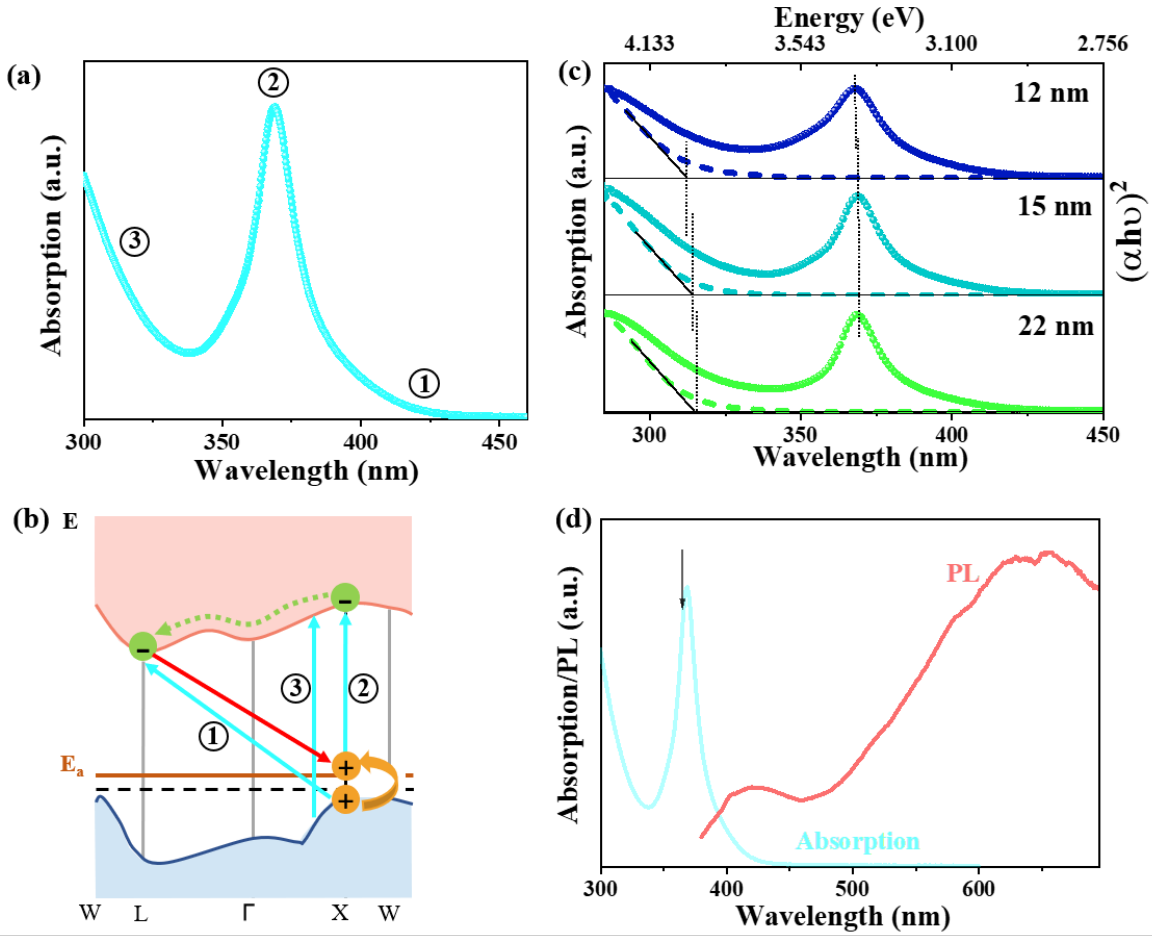

Figure 5.1: Linear Spectroscopy of 15 nm $Cs_2AgBiCl_6$ DP NCs (a) The linear absorption spectrum of 15 nm DP NCs in toluene. It is composed of three parts: ① indirect optical transitions, ② the strong excitonic resonance and ③ direct optical transitions. **(b)** Band structure of $Cs_2AgBiCl_6$ DP. The orange horizontal line depicts the hole acceptor level E_a. The blue and red arrows indicate different optical transitions and radiative recombination, respectively. The green dashed arrow indicates intervalley scattering of photoexcited electrons. **(c)** The linear absorption spectra and their corresponding Tauc plots of DP NCs with different sizes (12 nm, 15 nm and 22 nm). **(d)** PL of 15 nm DP NCs excited at 365 nm (the black arrow).

Table 5.1: Exciton Peak Position, Direct Bandgap Energies E_g Determined from Tauc Plots and Exciton Binding Energies of NCs with Different Sizes.

Size (nm)	Exciton peak position (eV)	E_g (eV)	Exciton binding energies (eV)
12	3.36	3.97	0.61
15	3.36	3.94	0.58
22	3.36	3.92	0.56

radius, which is between 3-4 nm.[88] Accordingly, the strong quantum confinement effect is not applicable. In this case, a small exciton binding energy of a few meV is expected in these bulk-like NCs due to the dielectric screening of the Coulomb interaction. In addition, the VB of $Cs_2AgBiCl_6$ shows a strong dispersion along the X to Γ direction. It leads to a comparably small effective hole mass, and thus a small reduced mass of excitons. Accordingly, it further supports the conclusion that the excitons have a relatively small binding energy. However, this is in contrast to the extralarge exciton binding energies around 600 meV irrespective of the NC size, which is obtained from the energetic difference of direct bandgap energies and the corresponding exciton peak position (Figure 5.1c and Table 5.1).

The prominent absorption resonance was explained as defect-bound excitons reported by Dey et.[88] In halide DPs, there are a large number of intrinsic point defects such as halogen vacancies, cesium interstitials, and antisite substitutions. Based on the calculated formation energy of intrinsic defects in $Cs_2AgBiCl_6$, silver vacancies are the most stable shallow defects near the VB.[63] The silver vacancies act as hole acceptors, introducing a shallow trap level that leads to hole localization. The holes localized in the silver vacancy energy level have an infinite effective mass, leading to bound excitons with giant oscillator strength. Due to the localized nature of the bound excitons, one can expect a fixed spectral position in $Cs_2AgBiCl_6$ DP NCs irrespective of their size, as long as they are larger than the Bohr radius. In fact, the spectral position of the exciton resonance remains fixed at 369 nm for all sizes of NCs studied here (Figure 5.1c).

Under an excitation of 365 nm (close to the exciton resonance), a broad emission with two distinct PL bands is observed (Figure 5.1d). The high-energetic one (blue PL) centers at 425 nm, and the low-energetic one (red PL) is located at 650 nm. In the following sections, the origin of the two emission bands will be explained together with spectroscopic measurements. I will show that the silver defect-bound excitons play an important role on the optical properties of $Cs_2AgBiCl_6$ DP NCs.

5.2 Red Emission

PLE spectroscopy of the red and blue PL, performed by tuning the excitation wavelength, has been conducted to investigate their origins. In this section, I will focus on the low-energetic red emission. The PLE spectrum detected at 650 nm (as indicated by the orange arrow) is shown in Figure 5.2. It nicely follows the absorption spectrum of the NCs, especially the excitonic resonance. It suggests that excitation at the exciton resonance can lead to the red emission. In the following section, I will testify that the broad red emission originates from the recombination between electrons at the CB minimum (the L point) and holes in trapping levels above the VB (Figure 5.1b).

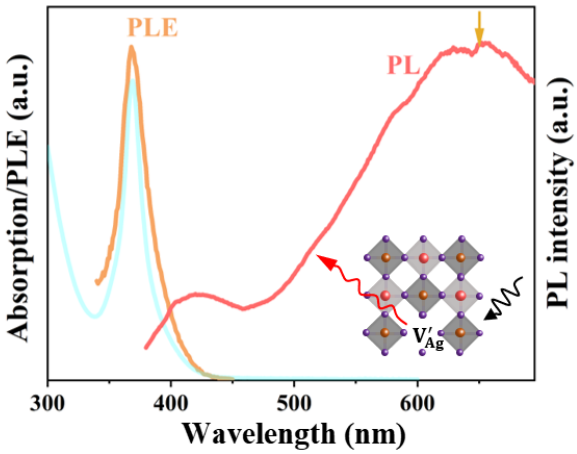

Figure 5.2: PLE of the Red Emission for 15 nm $Cs_2AgBiCl_6$ DP NCs The Figure shows the PLE spectrum (the orange curve) of 15 nm DP NCs in toluene detected at 650 nm (the orange arrow). It follows well the corresponding absorption spectrum (the light blue curve). The insert indicates that the red emission originates from silver vacancies.

5.2.1 Temperature Dependence of Red Emission

When the temperature decreases, defect-related carrier recombination exhibits a thermally activated behavior distinct from free charge carrier recombination.[154] To further testify the trap-mediated recombination nature of the red PL, temperature-dependent PL measurements are carried out.

Figure 5.3a shows a significant increase in the intensity of the red PL as the temperature decreases from 294 K to 65 K. For $Cs_2AgBiCl_6$ with an indirect bandgap, free electron-hole pairs at the band extrema recombine with the assistance of phonons. In this case, one would expect a decrease in emission under low temperatures because of a smaller phonon population. The result in Figure 5.3a is the opposite, demonstrating the defect-related nature of red PL. Optical transitions at the direct band edge create electrons and holes at the X point. The electrons subsequently relax to the CB minimum (L point) after intervalley scattering within

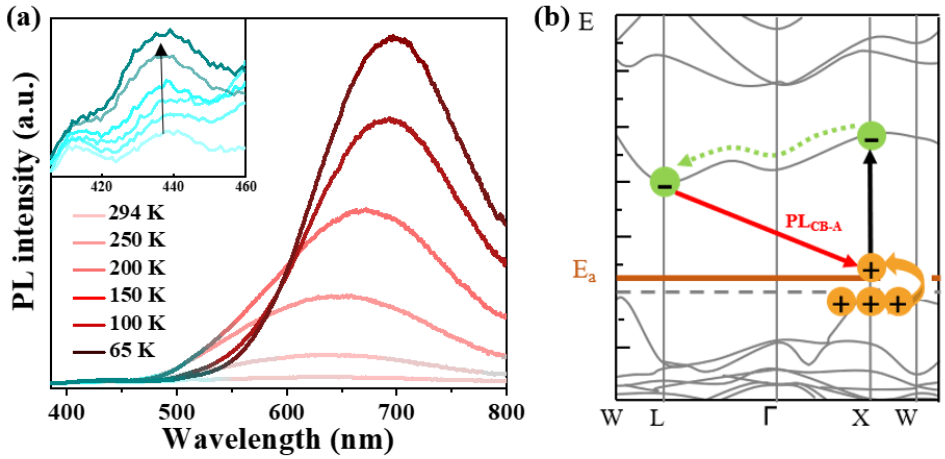

Figure 5.3: Temperature-Dependent PL (a) PL of 15 nm DP NCs at different temperatures (from 294 K to 65 K) under 365 nm excitation. The inset shows the enlarged the blue emission under different temperatures. The arrow shows the lower temperature direction. The small hump at 410 nm originates from Raman scattering from toluene. **(b)** Scheme showing hole populations in the the VB maximum and the defect level E_a(the orange flat line), which is influenced by temperature. The black indicates direct optical transitions. The red arrow shows excitonic recombination between electrons at L point and holes in the defect level. The green dashed arrow shows intervalley scattering of electrons.

sub-picoseconds (Figure 5.3b). Holes in the VB maximum are trapped by the defect level. The localized hole wave function offers large k-values, resulting in nonzero overlap integrals with electrons at the L point, thereby enabling finite optical transition strengths. This allows for recombination between electrons at the CB minimum and holes localized at the defect level. Therefore, a broad red emission is observed in this indirect semiconductor. The localization-delocalization process of holes is dynamic. Under low temperatures, holes have less thermal energy (k_BT) to de-trap from the localized state. In other words, the silver defect state has a larger hole population at low temperatures. These trapped holes recombine with electrons and lead to an increased PL intensity as the temperature decreases. In summary, the temperature-dependent behavior testifies the defect-mediated carrier recombination as the origin of the red PL.

In addition, the red PL peak undergoes a redshift of approximately 60 nm (175 meV), moving to lower energies under low temperatures(Figure 5.4). The significant redshift of the red PL in these DPs at low temperatures remains under debate.[155,156] The displacement of atoms from equilibrium perturbs the periodic potential exerted on charge carriers, resulting in carrier-phonon interactions. In DPs with two B-site metals, this effect is even more pronounced than their single perovskite counterparts, which provides a complex environment for carrier-phonon interactions.

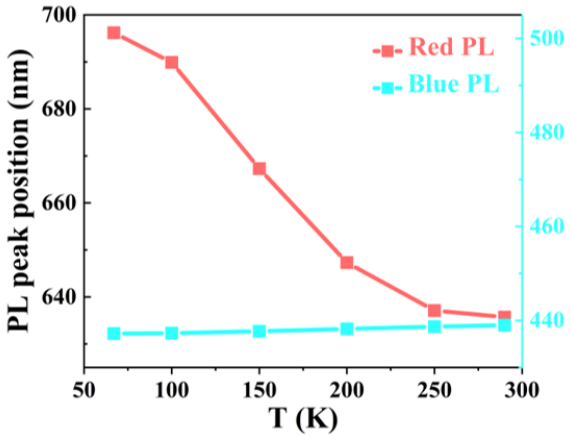

Figure 5.4: Peak Positions of the Red and Blue PL with Temperature The peak position values are taken from Figure 5.3a.

Compared with the red PL, the blue PL is more insensitive to temperature without obvious changes in both PL intensity and peak position (inset of Figure 5.3a anf Figure 5.4). I will explain it in detail in Section 5.3.

5.2.2 A Model for Photoluminescence at Low Temperatures

In the last subsection, the carrier dynamics at low temperatures upon photoexcitation has been studied. Based on it, I try to determine the PL intensity with respect to every temperature. To achieve this, a model is rquired to determine the energetic difference between the defect energy level and the VB maximum. The experimental values of red PL intensity under different temperatures are extracted and plotted against $\frac{1}{k_B T}$ in Figure 5.5.

To be quantitative, red PL intensity is proportional to the concentration of excitons bound to the silver vacancy state (n_h^A). The exciton concentration is determined by the concentration of holes in the defect state. The conclusion is drawn from the following hint. With decreasing temperature, red emission increases continuously. It follows with the growing population of holes in the defect state, rather than the typical decrease in the electron concentration. The concentration of holes trapped in the defect state is expressed by the Fermi-Dirac distribution function. Then the PL intensity could be written as:

$$PL_{CB \rightarrow A} \propto n_h^A(T) = \frac{N_A}{1 + \frac{1}{2}\exp^{\frac{\mu - E_A}{k_B T}}} \tag{5.1}$$

Here, N_A represents the density of silver vacancies, which is constant at different temperatures. The exponential term is multiplied by $\frac{1}{2}$ because one silver vacancy can only be occupied by one hole. μ is the chemical potential. N_A is the energy level of the defects. ΔE is set as the energy difference between the defect level E_A and the chemical potential μ. Then Equation 5.1

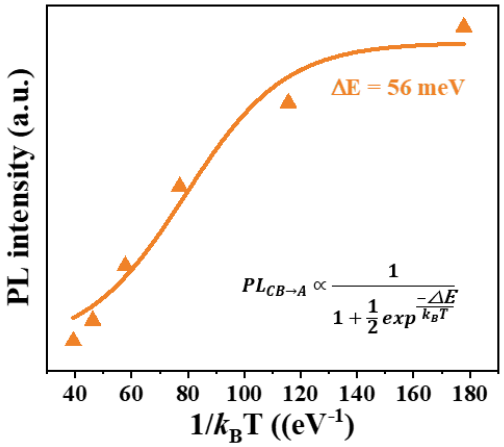

Figure 5.5: Fitting of Temperature-Dependent PL The scatters show red PL intensities at different temperatures. The x axis is converted to $\frac{1}{k_B T}$ from T. The curve shows the fitting result based on Equation 5.2 (the inset).

is written as:

$$PL_{\mathrm{CB}\to\mathrm{A}} \propto \frac{1}{1+\frac{1}{2}\exp^{\frac{-\Delta E}{k_B T}}} \tag{5.2}$$

$Cs_2AgBiCl_6$ exhibits p-type semiconductor behavior with the chemical potential pinned near the VB maximum as a result of the presence of abundant defects including Ag vacancies.[63] It is assumed that the chemical potential μ is quite close to the VB maximum. Therefore, ΔE is considered the energy difference between the defect level and the VB maximum , that is the activation energy of silver vacancies. On the basis of Equation 5.2, a temperature-dependent PL model is developed. The fitting curve matches the experimental data well. An activation energy of 56 meV is obtained from the PL of 15 nm DP NCs, which is consistent with the theoretically calculated values for that of Ag vacancies.

5.3 Blue Emission

5.3.1 Ligands Play a Role

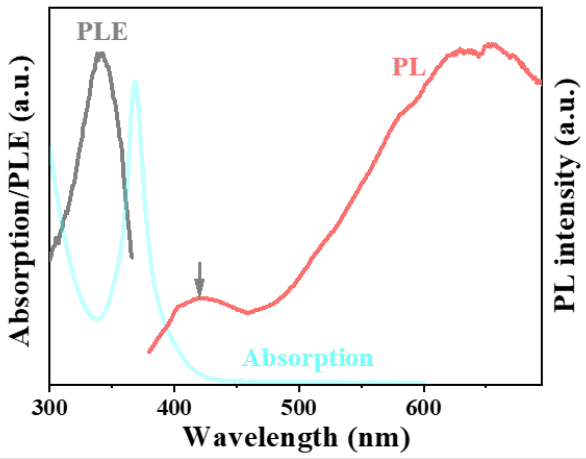

Figure 5.6: PLE of the Blue Emission The figure highlights the PLE spectrum of 15 nm DP NCs in toluene detected at the center of the blue emission (425 nm).

Apart from the red emission, the PL spectrum shows a high-energetic peak centered at 425 nm. To gain insights into its origin, PLE spectroscopy was performed by detecting emission at this wavelength. Surprisingly, the spectrum doesn't follow the excitonic absorption peak and exhibits a hump at its high-energetic side (around 340 nm). It signifies that the blue emission is not generated through excitation at the strong exciton resonance of NCs.

As reported, the blue emission appears in $Cs_2AgBiCl_6$ NCs,[88,157] but has never been observed in $Cs_2AgBiCl_6$ single crystals or polycrystalline films. Unlike traditional synthesis methods for single crystals or polycrystalline films, such as a hydrothermal method, the preparation of perovskite NCs requires the assistance of capping ligands to control their growth and maintain their stability. They are usually organic ligands with long carbon chains and functional groups such as carboxyl, thiol, amine, etc.. Oleic acid and oleylamine form a classic combination for the synthesis of colloidal quantum dots. They are reported to be blue emitters in addition to capping ligands, which may also interact with their matrices.[158,159]

To synthesize the NC, oleic acid is used together with lecithin in place of oleylamine to enhance their stability. To reveal the role of these ligands in the broad emission of these NCs, I have detected PL and PLE of the mixture of these two ligands with the same parameter as those of the DP NCs. In Figure 5.7, the ligands display an asymmetric PL band at 415 nm, attributed to optical transitions within the molecular orbitals ($\pi \longrightarrow \pi^*$ and/or $n \longrightarrow \pi^*$). The result is in agreement with the blue emission of DP NCs. The PLE spectrum of the ligands is also consistent with that of the NCs at the same detection wavelength. Consequently, it is concluded that the blue emission of the DP NCs originates from the ligands. As the

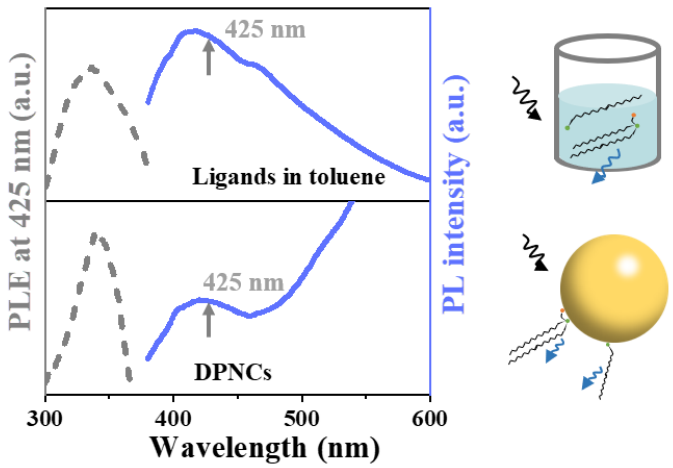

Figure 5.7: Comparasion of PL and PLE between NCs and Ligands The figure shows: (upper) PL (excited at 365 nm) and PLE (detected at 425 nm) of ligands; (lower) blue emission of NC, and PLE of NC detected at 425 nm. The right panel shows the schematic diagram of ligands (oleic acid, lecithin) in toluene and NCs decorated with the two ligands.

antisolvent washing procedure removes residual unattached ligands in toluene, the blue emission is mainly attributed to the ligands attached to NC's surface. The conclusion is supported by temperature-dependent PL results, where the blue emission shows a different feature (comparatively temperature stable) with the excitonic recombination of the NCs.

The blue emission has been further investigated with regard to NCs with different sizes. In Figure 5.8a, NCs with a diameter of 12 nm, 15 nm and 22 nm exhibit distinguished PL intensities. It is observed that the NCs with a smaller size exhibit a stronger blue emission. This phenomenon is attributed to a larger surface-to-volume ratio for smaller NCs, which indicates a larger ligand-to-NC ratio. The results reinforce the conclusion that the ligands attached to NC surface play a indispensable role on the high-energetic emission. It is noted that the blue emission of ligands may overlap with PL of lead-based perovskites with high quantum yields. Therefore, its presence was overlooked in many publications.

5.3.2 Plasmonic Enhancement Effects of Surface-Attached Ag

A closer examination of the NC surface using high-angle annular dark-field scanning transmission electron microscopy (HAADF-STEM) (Figure 5.8b) finds that there are abundant white dots decorating the NC spheres. From energy-dispersive X-ray spectroscopy (the inset of Figure 5.8b), these bright white dots are identified as Ag nanoclusters with an average size of 3 nm. The presence of these Ag nanoclusters on the surface of silver-based DP NCs is not surprising. However, their origins are under debate. Some metal ions, such as Ag^+, were reported to be reduced into their metal clusters ex situ via the electron beam during TEM characterization.[160] The presence of these Ag nanoclusters is regarded as a disadvantage to NC stability. Meanwhile, Ag nanoclusters have been documented to form in situ during

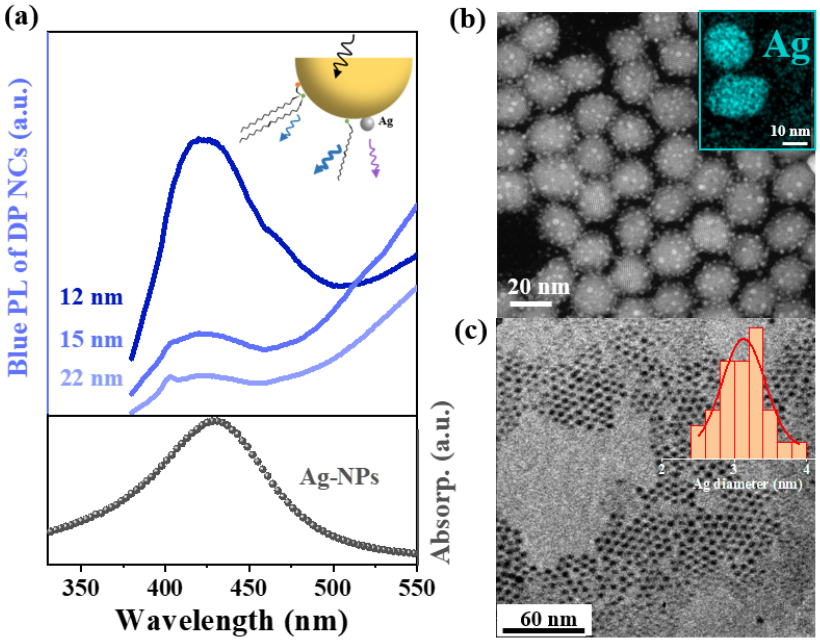

Figure 5.8: Plasmonic Enhancement Effects of Ag Nanoclusters (a) The upper figure shows blue emissions for NCs with a diameter of 12, 15 and 22 nm (excited at 365 nm). The lower figure exhibits the absorption spectrum of as-synthesized Ag NPs (3 nm) with a plasma resonance at 430 nm. The insert draws a NC decorated with ligands (lecithin and oleic acid) and an Ag nanocluster. The arrow indicates the mechanism of the blue emission. (b) An image of 15 nm DP NCs acquired from HAADF-STEM. The insert testifies the presence of Ag element in nanoclusters via energy-dispersive X-ray spectroscopy. (c) An image of as-synthesized Ag NPs obtained from TEM. The insert shows a size distribution centered at around 3 nm.

hot injection synthesis of Ag-based NCs.[161] They could act as nucleation centers for particle growth in the early stage. In fact, Ag nanoparticles (NPs) can be easily synthesized in the presence of Ag precursors and oleylamine at 120°C.[162] Based on the study, it is believed that the Ag nanoclusters on the surface of DP NCs are formed during synthesis. How does their existence influence the optical properties?

Ag NPs were synthesized via the hot injection method and their size is controlled to be the same as that of the nanoclusters on NC surface.[162] Figure 5.8c and its insert show uniform NPs with a size distribution centered at 3 nm. From their absorption spectrum (Figure 5.8a, lower panel), these Ag NPs exhibit a localized surface plasmon resonance (LSPR) at 430 nm. Coincidentally, their plasmon signal appears at the same energetic position as the ligand emission. That means that the surface plasmon of Ag nanoclusters attached to the surface of NC is resonant with the emission of ligands in the vicinity. Noble metals, such as Au and Ag, are well-investigated for inducing plasmonic enhancement effects on the emission of nearby dye molecules with comparable emission frequencies, particularly in the case of dimers and aggregated morphologies. Considering the coexistence of surface attached Ag nanoclusters

and ligands resonant at the same wavelength, it is reasonable to conclude that ligand emission is enhanced by the plasmonic effects of surface-decorated Ag nanoclusters.

In conclusion, this work has revealed the origins of the broad PL spectrum (including blue and red emission peaks) from $Cs_2AgBiCl_6$ DP NCs. It is the first time that silver (silver vacancies and surface-attached silver nanoclusters) is testified to play an important role in the optical properties of Ag-based DPs. The results are helpful for in-depth spectral investigations of $Cs_2AgBiCl_6$ DPs, as well as their stability and optoelectronic applications.

6

Conclusions and Outlook

This thesis seeks to address the two limitations of lead halide perovskites (LHPs)–the moisture instability and the high toxicity–for energy-related applications. The facile preparation, structural tunability, and unique optical properties of LHPs have led to great success in solar cells and light-emitting diodes (LEDs). However, due to their dissolution in polar solvents such as methanol and water, their application in photocatalysis has been limited. In this thesis, it has been demonstrated that halide perovskite ($MAPbBr_3$, $CsPbBr_3$) nanoplatelets (NPls) are stable for photocatalytic hydrogen production when water vapor and methanol vapor are used as proton sources. The charge carrier transfer mechanism is investigated with time-resolved photoluminescence (PL) and transient absorption spectroscopy (TAS).

Hydrogen evolution rates (HERs) from LHP NPls decorated by Pt cocatalyst are quantitatively monitored under simulated solar irradiation using a gas chromatography (GC). **In methanol vapor, an optimal $MAPbBr_3$ NPls film exhibits steady hydrogen evolution for 20 hours under solar irradiation**, reaching a marked hydrogen evolution rate of 424 $\mu mol \cdot g^{-1} \cdot h^{-1}$. The HERs are influenced by the vapor composition and concentration. More strikingly, the recoverable HER infers that the catalyst remains defect-tolerant during the reaction. Furthermore, the vapor idea works for different LHP NPls, demonstrating the general applicability of the method across various perovskite compositions.

Time-resolved spectroscopies reveal that **the diffusion-limited feeding of electron-hole pairs towards Pt clusters dominates the dynamics of charge transfer.** The PL decay of $MAPbBr_3$ NPls is much faster than that of the pristine NPls, which is attributed to the combination of longer-lasting exciton diffusion and subsequent rapid electron transfer.

Excitons photoexcited in the vicinity of a Pt cluster will experience an electron transfer in a short time. However, for excitons photoexcited far away from a Pt cluster, they may recombine radiatively or trapped by defects, in addition to undergoing an electron transfer. The diffusion time from NPls to Pt is influenced by the geometry of NPls and the concentration of Pt clusters. An exponential distribution function of the diffusion time is assumed, which is in good agreement with the experimentally obtained data with a maximum diffusion time extracted. TAS further elucidates the ultrafast electron transfer process with the advanced bleach growth maximum in the first few picoseconds.

The present study demonstrates a uniquely efficient and stable system using halide perovskite NCs for hydrogen production under methanol vapor, an environment that is polar and volatile. It shows the potential of directly using halide perovskites for light-driven reactions in polar environments. Further development is required to enhance halide perovskite photocatalysts for a benchmark HER, which is now underway. This study also provides a fundamental understanding of the electron transfer mechanism from LHPs to Pt metal across different time scales, providing valuable insights for optimizing their photocatalytic performance.

On the other hand, bismuth as an environmentally benign heavy metal, offers a promising alternative to mimic some of the desirable properties of lead-based perovskites due to its similar ionic radius and electronic configuration to lead, while enhancing environmental safety. To accommodate trivalent Bi^{3+} into a three-dimensional perovskite structure, a combination with a monovalent cation is required to form double perovskites (DPs) with the formula of A_2BBiX_6 (X = Br, Cl). Among them, Cs_2AgBiX_6 (X = Br, Cl) stands out as the most investigated DPs due to its intriguing optical properties and good stability. Although exhibiting an indirect bandgap, $Cs_2AgBiCl_6$ colloidal DP nanocrystals (NCs) show broad PL spectrum promising for white light emission application. The origin of the dual-peak emission, which has been a subject of extensive debate for decades, is examined in this study.

In Chapter 5, a bright PL spectrum characterized by a spectrally broad red emission centered around 650 nm and a narrower blue emission band centered at 425 nm is observed in $Cs_2AgBiCl_6$ colloidal DP NCs. The broad emission was attributed to self-trapped excitons, color centers, and indirect defect bound excitons. In the thesis, it is shown that silver (silver-nanoclusters and -vacancies) plays a crucial role in the explanation of both emission bands observed in these DP NCs.

The low-energetic red PL originates from defect-bound excitonic recombination associated with silver vacancies. Ag vacancies as a shallow donor defect are easily formed during the hot injection synthesis of $Cs_2AgBiCl_6$. The trapping of holes in Ag vacancies leads to a spatial localization of the hole wave function on the scale of the lattice constant. This provides k-values for the hole wave function at all boundaries of the Brillouin zone and thus favors the recombination with electrons at the L-point. A large exciton binding energy

of 0.6 eV acquired from UV-Vis absorption spectrum supports the picture of defect-related excitonic transitions. Moreover, this is confirmed by the photoluminescence excitation (PLE) spectrum monitored at the red peak maximum, which closely follows the excitonic absorption spectrum of the NCs. Trap mediated carrier recombination brings out thermally activated behavior in red PL intensity, characterized by a continuous increase in intensity and a red shift in energetic position as the temperature decreases down to 65 K. An activation energy of around 56 meV is extracted from the trapped-mediated PL model.

The high-energetic blue PL comes from surface-attached ligands of NCs, which may be enhanced by plasmonic effects of Ag nanoclusters. PLE detected at the blue peak maximum testifies that the high-energy blue emission cannot be excited via the strong exciton resonance of the NCs, but relates to ligands attached on the NC surface–OA and lecithin as a combination to increase NC stability and monodispersity. It is supported by the evidence from size-dependent blue emission. Surprisingly, their emission spectrum coincides exactly with the plasmon resonance of Ag nanoclusters, which are observed on the surface of the NCs by transmission electron microscopy (TEM) characterization. The blue emission may be enhanced by the plasmonic effects of these Ag nanoclusters in the vacinity. More characterization is required in the future for further investigation.

This work unveals the nature of both emission bands in $Cs_2AgBiCl_6$ DP NCs, and highlights the critical role of surface chemistry in colloidal Ag-based DP NCs. Colloidal halide perovskite NCs, especially those within strong/weak quantum confinement regimes, possess rich surface chemistry—an aspect that remains largely underexplored and underestimated. The investigation of the interaction between perovskite NCs and surface additives is of vital importance for improving their optical properties, stability, and optoelectronic application performance. Cs_2AgBiX_6 DP NCs with broad emission, represent a promising lead-free alternative for white light LEDs. Even though the emission efficiency for their pure phase is low, alloying with metallic ions like Na, In ions has been shown to significantly improve the PL quantum yield.[22] Overall, our findings on the optical properties of $Cs_2AgBiCl_6$ NCs are important to advance the development of silver-based lead-free DP family towards future optoelectronic applications.

References

[1] R. P. Feynman. "Caltech Engineering and Science." In: *23* 5 (1960), pp. 22–36 (cited on page 1).

[2] A. P. Alivisatos. "Semiconductor Clusters, Nanocrystals, and Quantum Dots." In: *Science* 271.5251 (1996), pp. 933–937. DOI: 10.1126/science.271.5251.933 (cited on page 1).

[3] Maksym V. Kovalenko, Loredana Protesescu, and Maryna I. Bodnarchuk. "Properties and potential optoelectronic applications of lead halide perovskite nanocrystals." In: *Science* 358.6364 (2017), pp. 745–750. DOI: 10.1126/science.aam7093 (cited on page 1).

[4] David J. Norris, Alexander L. Efros, and Steven C. Erwin. "Doped Nanocrystals." In: *Science* 319.5871 (2008), pp. 1776–1779. DOI: 10.1126/science.1143802 (cited on page 1).

[5] X. Michalet, F. F. Pinaud, L. A. Bentolila, J. M. Tsay, S. Doose, J. J. Li, G. Sundaresan, A. M. Wu, S. S. Gambhir, and S. Weiss. "Quantum Dots for Live Cells, in Vivo Imaging, and Diagnostics." In: *Science* 307.5709 (2005), pp. 538–544. DOI: 10.1126/science.1104274 (cited on page 1).

[6] Luciana C. Schmidt, Antonio Pertegás, Soranyel González-Carrero, Olga Malinkiewicz, Said Agouram, Guillermo Mínguez Espallargas, Henk J. Bolink, Raquel E. Galian, and Julia Pérez-Prieto. "Nontemplate Synthesis of CH3NH3PbBr3 Perovskite Nanoparticles." In: *J. Am. Chem. Soc.* 136.3 (2014), pp. 850–853. DOI: 10.1021/ja4109209 (cited on pages 1, 34).

[7] Akihiro Kojima, Kenjiro Teshima, Yasuo Shirai, and Tsutomu Miyasaka. "Organometal Halide Perovskites as Visible-Light Sensitizers for Photovoltaic Cells." In: *J. Am. Chem. Soc.* 131.17 (2009), pp. 6050–6051. DOI: 10.1021/ja809598r (cited on pages 1, 6).

[8] Amrita Dey, Junzhi Ye, Apurba De, Elke Debroye, Seung Kyun Ha, Eva Bladt, Anuraj S. Kshirsagar, Ziyu Wang, Jun Yin, Yue Wang, Li Na Quan, Fei Yan, Mengyu Gao, Xiaoming Li, Javad Shamsi, Tushar Debnath, Muhan Cao, Manuel A. Scheel, Sudhir Kumar, Julian A. Steele, Marina Gerhard, Lata Chouhan, Ke Xu, Xian-gang Wu, Yanxiu Li, Yangning Zhang, Anirban Dutta, Chuang Han, Ilka Vincon, Andrey L. Rogach, Angshuman Nag, Anunay Samanta, Brian A. Korgel, Chih-Jen Shih, Daniel R. Gamelin, Dong Hee Son, Haibo Zeng, Haizheng Zhong, Handong Sun, Hilmi Volkan Demir, Ivan G. Scheblykin, Iván Mora-Seró, Jacek K. Stolarczyk, Jin Z. Zhang, Jochen Feldmann, Johan Hofkens, Joseph M. Luther, Julia Pérez-Prieto, Liang Li, Liberato Manna, Maryna I. Bodnarchuk, Maksym V. Kovalenko, Maarten B. J. Roeffaers, Narayan Pradhan, Omar F. Mohammed, Osman M. Bakr, Peidong Yang, Peter Müller-Buschbaum, Prashant V. Kamat, Qiaoliang Bao, Qiao Zhang, Roman Krahne, Raquel E. Galian, Samuel D. Stranks, Sara Bals, Vasudevanpillai Biju, William A. Tisdale, Yong Yan, Robert L. Z. Hoye, and Lakshminarayana Polavarapu. "State of the Art and Prospects for Halide Perovskite Nanocrystals." In: *ACS Nano* 15.7 (2021), pp. 10775–10981. DOI: 10.1021/acsnano.0c08903 (cited on pages 1, 2, 6, 21, 34, 36, 53).

[9] Quinten A. Akkerman, Tan P. T. Nguyen, Simon C. Boehme, Federico Montanarella, Dmitry N. Dirin, Philipp Wechsler, Finn Beiglböck, Gabriele Rainò, Rolf Erni, Claudine Katan, Jacky Even, and Maksym V. Kovalenko. "Controlling the nucleation and growth kinetics of lead halide perovskite quantum dots." In: *Science* 377.6613 (2022), pp. 1406–1412. DOI: 10.1126/science.abq3616 (cited on pages 2, 18).

[10] Anja Barfüßer, Sebastian Rieger, Amrita Dey, Ahmet Tosun, Quinten A. Akkerman, Tushar Debnath, and Jochen Feldmann. "Confined Excitons in Spherical-Like Halide Perovskite Quantum Dots." In: *Nano Lett* 22.22 (2022), pp. 8810–8817. DOI: 10.1021/acs.nanolett.2c02223 (cited on pages 2, 18, 34).

[11] Joo Sung Kim, Jung-Min Heo, Gyeong-Su Park, Seung-Je Woo, Changsoon Cho, Hyung Joong Yun, Dong-Hyeok Kim, Jinwoo Park, Seung-Chul Lee, Sang-Hwan Park, Eojin Yoon, Neil C. Greenham, and Tae-Woo Lee. "Ultra-bright, efficient and stable perovskite light-emitting diodes." In: *Nature* 611.7937 (2022), pp. 688–694. DOI: 10.1038/s41586-022-05304-w (cited on pages 2, 6).

[12] Xiaolin Zhu, Yixiong Lin, Jovan San Martin, Yue Sun, Dian Zhu, and Yong Yan. "Lead halide perovskites for photocatalytic organic synthesis." In: *Nature Communications* 10.1 (2019), p. 2843. DOI: 10.1038/s41467-019-10634-x (cited on page 2).

[13] Sunghak Park, Woo Je Chang, Chan Woo Lee, Sangbaek Park, Hyo-Yong Ahn, and Ki Tae Nam. "Photocatalytic hydrogen generation from hydriodic acid using methylammonium lead iodide in dynamic equilibrium with aqueous solution." In: *Nature Energy* 2.1 (2016), p. 16185. DOI: 10.1038/nenergy.2016.185 (cited on pages 2, 31, 53).

[14] Micaela Crespo-Quesada, Luis M. Pazos-Outón, Julien Warnan, Moritz F. Kuehnel, Richard H. Friend, and Erwin Reisner. "Metal-encapsulated organolead halide perovskite photocathode for solar-driven hydrogen evolution in water." In: *Nature Communications* 7.1 (2016), p. 12555. DOI: 10.1038/ncomms12555 (cited on page 2).

[15] Shangjun Cheng and Haizheng Zhong. "What Happens When Halide Perovskites Meet with Water?" In: *The Journal of Physical Chemistry Letters* 13.10 (2022), pp. 2281–2290. DOI: 10.1021/acs.jpclett.2c00166 (cited on pages 2, 19).

[16] Zhaoning Song, Niraj Shrestha, Suneth C. Watthage, Geethika K. Liyanage, Zahrah S. Almutawah, Ramez H. Ahangharnejhad, Adam B. Phillips, Randy J. Ellingson, and Michael J. Heben. "Impact of Moisture on Photoexcited Charge Carrier Dynamics in Methylammonium Lead Halide Perovskites." In: *J. Phys. Chem. Lett.* 9.21 (2018), pp. 6312–6320. DOI: 10.1021/acs.jpclett.8b02595 (cited on pages 2, 19).

[17] Md Azimul Haque, Ahad Syed, Faheem Hassan Akhtar, Rahul Shevate, Simrjit Singh, Klaus-Viktor Peinemann, Derya Baran, and Tom Wu. "Giant Humidity Effect on Hybrid Halide Perovskite Microstripes: Reversibility and Sensing Mechanism." In: *ACS Appl. Mater. Interfaces* 11.33 (2019), pp. 29821–29829. DOI: 10.1021/acsami.9b07751 (cited on pages 2, 19).

[18] Loreta A. Muscarella and Eline M. Hutter. "Halide Double-Perovskite Semiconductors beyond Photovoltaics." In: *ACS Energy Letters* 7.6 (2022), pp. 2128–2135. DOI: 10.1021/acsenergylett.2c00811 (cited on page 2).

[19] Cuncun Wu, Qiaohui Zhang, Ganghong Liu, Zehao Zhang, Duo Wang, Bo Qu, Zhijian Chen, and Lixin Xiao. "From Pb to Bi: A Promising Family of Pb-Free Optoelectronic Materials and Devices." In: *Advanced Energy Materials* 10.13 (2020), p. 1902496. DOI: 10.1002/aenm.201902496 (cited on pages 2, 67).

[20] Adam H. Slavney, Te Hu, Aaron M. Lindenberg, and Hemamala I. Karunadasa. "A Bismuth-Halide Double Perovskite with Long Carrier Recombination Lifetime for Photovoltaic Applications." In: *J. Am. Chem. Soc.* 138.7 (2016), pp. 2138–2141. DOI: 10.1021/jacs.5b13294 (cited on pages 2, 21, 22, 25, 67).

[21] Robert L. Z. Hoye, Lissa Eyre, Fengxia Wei, Federico Brivio, Aditya Sadhanala, Shijing Sun, Weiwei Li, Kelvin H. L. Zhang, Judith L. MacManus-Driscoll, Paul D. Bristowe, Richard H. Friend, Anthony K. Cheetham, and Felix Deschler. "Fundamental Carrier Lifetime Exceeding 1 µs in Cs2AgBiBr6 Double Perovskite." In: *Advanced Materials Interfaces* 5.15 (2018), p. 1800464. DOI: 10.1002/admi.201800464 (cited on pages 2, 23, 25).

[22] Jiajun Luo, Xiaoming Wang, Shunran Li, Jing Liu, Yueming Guo, Guangda Niu, Li Yao, Yuhao Fu, Liang Gao, Qingshun Dong, Chunyi Zhao, Meiying Leng, Fusheng Ma, Wenxi Liang, Liduo Wang, Shengye Jin, Junbo Han, Lijun Zhang, Joanne Etheridge, Jianbo Wang, Yanfa Yan, Edward H. Sargent, and Jiang Tang. "Efficient and stable emission of warm-white light from lead-free halide double perovskites." In: *Nature* 563.7732 (2018), pp. 541–545. DOI: 10.1038/s41586-018-0691-0 (cited on pages 2, 25, 81).

[23] Guichuan Xing, Nripan Mathews, Shuangyong Sun, Swee Sien Lim, Yeng Ming Lam, Michael Grätzel, Subodh Mhaisalkar, and Tze Chien Sum. "Long-Range Balanced Electron- and Hole-Transport Lengths in Organic-Inorganic CH3NH3PbI3." In: *Science* 342.6156 (2013), pp. 344–347. DOI: 10.1126/science.1243167 (cited on page 6).

[24] Samuel D. Stranks, Giles E. Eperon, Giulia Grancini, Christopher Menelaou, Marcelo J. P. Alcocer, Tomas Leijtens, Laura M. Herz, Annamaria Petrozza, and Henry J. Snaith. "Electron-Hole Diffusion Lengths Exceeding 1 Micrometer in an Organometal Trihalide Perovskite Absorber." In: *Science* 342.6156 (2013), pp. 341–344. DOI: 10.1126/science.1243982 (cited on page 6).

[25] Martin A. Green, Anita Ho-Baillie, and Henry J. Snaith. "The emergence of perovskite solar cells." In: *Nature Photonics* 8.7 (2014), pp. 506–514. DOI: 10.1038/nphoton.2014.134 (cited on page 6).

[26] H. L. Wells. "Über die Cäsium- und Kalium-Bleihalogenide." In: *Zeitschrift für anorganische Chemie* 3.1 (1893), pp. 195–210. DOI: 10.1002/zaac.18930030124 (cited on page 6).

[27] Dieter Weber. "CH3NH3PbX3, ein Pb(II)-System mit kubischer Perowskitstruktur / CH3NH3PbX3, a Pb(II)-System with Cubic Perovskite Structure." In: 33.12 (1978), pp. 1443–1445. DOI: 10.1515/znb-1978-1214 (cited on page 6).

[28] Dieter Weber. "Das Perowskitsystem CH3NH3 [Pb,Sn1-nX3] (X = Cl, Br, I) / The Perovskite System CH3NH3[PbnSn1-nX3] (X = C1, Br, I)." In: 34.7 (1979), pp. 939–941. DOI: 10.1515/znb-1979-0712 (cited on page 6).

[29] M. Era, S. Morimoto, T. Tsutsui, and S. Saito. "Organic–inorganic heterostructure electroluminescent device using a layered perovskite semiconductor (C6H5C2H4NH3)2PbI4." In: *Applied Physics Letters* 65.6 (1994), pp. 676–678. DOI: 10.1063/1.112265 (cited on page 6).

[30] C. R. Kagan, D. B. Mitzi, and C. D. Dimitrakopoulos. "Organic-Inorganic Hybrid Materials as Semiconducting Channels in Thin-Film Field-Effect Transistors." In: *Science* 286.5441 (1999), pp. 945–947. DOI: 10.1126/science.286.5441.945 (cited on page 6).

[31] Michael M. Lee, Joël Teuscher, Tsutomu Miyasaka, Takurou N. Murakami, and Henry J. Snaith. "Efficient Hybrid Solar Cells Based on Meso-Superstructured Organometal Halide Perovskites." In: *Science* 338.6107 (2012), pp. 643–647. DOI: 10.1126/science.1228604 (cited on pages 6, 31, 34).

[32] Zhi-Kuang Tan, Reza Saberi Moghaddam, May Ling Lai, Pablo Docampo, Ruben Higler, Felix Deschler, Michael Price, Aditya Sadhanala, Luis M. Pazos, Dan Credgington, Fabian Hanusch, Thomas Bein, Henry J. Snaith, and Richard H. Friend. "Bright light-emitting diodes based on organometal halide perovskite." In: *Nature Nanotechnology* 9.9 (2014), pp. 687–692. DOI: 10.1038/nnano.2014.149 (cited on page 6).

[33] Zhenyang Liu, Hanjun Yang, Junyu Wang, Yucheng Yuan, Katie Hills-Kimball, Tong Cai, Ping Wang, Aiwei Tang, and Ou Chen. "Synthesis of Lead-Free Cs2AgBiX6 (X = Cl, Br, I) Double Perovskite Nanoplatelets and Their Application in CO2 Photocatalytic Reduction." In: *Nano Lett* 21.4 (2021), pp. 1620–1627. DOI: 10.1021/acs.nanolett.0c04148 (cited on page 6).

[34] Takayuki Chiba, Yukihiro Hayashi, Hinako Ebe, Keigo Hoshi, Jun Sato, Shugo Sato, Yong-Jin Pu, Satoru Ohisa, and Junji Kido. "Anion-exchange red perovskite quantum dots with ammonium iodine salts for highly efficient light-emitting devices." In: *Nature Photonics* 12.11 (2018), pp. 681–687. DOI: 10.1038/s41566-018-0260-y (cited on page 6).

[35] Lin Zhu, Hui Cao, Chen Xue, Hao Zhang, Minchao Qin, Jie Wang, Kaichuan Wen, Zewu Fu, Tao Jiang, Lei Xu, Ya Zhang, Yu Cao, Cailing Tu, Ju Zhang, Dawei Liu, Guangbin Zhang, Decheng Kong, Ning Fan, Gongqiang Li, Chang Yi, Qiming Peng, Jin Chang, Xinhui Lu, Nana Wang, Wei Huang, and Jianpu Wang. "Unveiling the additive-assisted oriented growth of perovskite crystallite for high performance light-emitting diodes." In: *Nature Communications* 12.1 (2021), p. 5081. DOI: 10.1038/s41467-021-25407-8 (cited on page 6).

[36] Chuanjiang Qin, Atula S. D. Sandanayaka, Chenyang Zhao, Toshinori Matsushima, Dezhong Zhang, Takashi Fujihara, and Chihaya Adachi. "Stable room-temperature continuous-wave lasing in quasi-2D perovskite films." In: *Nature* 585.7823 (2020), pp. 53–57. DOI: 10.1038/s41586-020-2621-1 (cited on page 7).

[37] Xiaobin Zhan, Xuning Zhang, Zhiyong Liu, Chen Chen, Lingxian Kong, Shulan Jiang, Shuang Xi, Guanglan Liao, and Xingyue Liu. "Boosting the Performance of Self-Powered CsPbCl3-Based UV Photodetectors by a Sequential Vapor-Deposition Strategy and Heterojunction Engineering." In: *ACS Appl. Mater. Interfaces* 13.38 (2021), pp. 45744–45757. DOI: 10.1021/acsami.1c15013 (cited on page 7).

[38] Letian Dou, Yang Yang, Jingbi You, Ziruo Hong, Wei-Hsuan Chang, and Gang Li. "Solution-processed hybrid perovskite photodetectors with high detectivity." In: *Nature Communications* 5.1 (2014), p. 5404. DOI: 10.1038/ncomms6404 (cited on page 7).

[39] Yong-Siou Chen, Joseph S. Manser, and Prashant V. Kamat. "All Solution-Processed Lead Halide Perovskite-BiVO4 Tandem Assembly for Photolytic Solar Fuels Production." In: *J. Am. Chem. Soc.* 137.2 (2015), pp. 974–981. DOI: 10.1021/ja511739y (cited on page 7).

[40] Jaeho Choi, Ji Su Han, Kootak Hong, Soo Young Kim, and Ho Won Jang. "Organic–Inorganic Hybrid Halide Perovskites for Memories, Transistors, and Artificial Synapses." In: *Advanced Materials* 30.42 (2018), p. 1704002. DOI: 10.1002/adma.201704002 (cited on page 7).

[41] Youngjun Park, Seong Hun Kim, Donghwa Lee, and Jang-Sik Lee. "Designing zero-dimensional dimer-type all-inorganic perovskites for ultra-fast switching memory." In: *Nature Communications* 12.1 (2021), p. 3527. DOI: 10.1038/s41467-021-23871-w (cited on page 7).

[42] Rohit Abraham John, Natalia Yantara, Yan Fong Ng, Govind Narasimman, Edoardo Mosconi, Daniele Meggiolaro, Mohit R. Kulkarni, Pradeep Kumar Gopalakrishnan, Chien A. Nguyen, Filippo de Angelis, Subodh G. Mhaisalkar, Arindam Basu, and Nripan Mathews. "Ionotronic Halide Perovskite Drift-Diffusive Synapses for Low-Power Neuromorphic Computation." In: *Advanced Materials* 30.51 (2018), p. 1805454. DOI: 10.1002/adma.201805454 (cited on page 7).

[43] Shuxia Tao, Ines Schmidt, Geert Brocks, Junke Jiang, Ionut Tranca, Klaus Meerholz, and Selina Olthof. "Absolute energy level positions in tin- and lead-based halide perovskites." In: *Nature Communications* 10.1 (2019), p. 2560. DOI: 10.1038/s41467-019-10468-7 (cited on page 7).

[44] T. Umebayashi, K. Asai, T. Kondo, and A. Nakao. "Electronic structures of lead iodide based low-dimensional crystals." In: *Physical Review B* 67.15 (2003), p. 155405. DOI: 10.1103/PhysRevB.67.155405 (cited on page 7).

[45] Laura M. Herz. "Charge-Carrier Dynamics in Organic-Inorganic Metal Halide Perovskites." In: *Annual Review of Physical Chemistry* 67.Volume 67, 2016 (2016), pp. 65–89. DOI: 10.1146/annurev-physchem-040215-112222 (cited on page 7).

[46] Christian Wehrenfennig, Giles E. Eperon, Michael B. Johnston, Henry J. Snaith, and Laura M. Herz. "High Charge Carrier Mobilities and Lifetimes in Organolead Trihalide Perovskites." In: *Advanced Materials* 26.10 (2014), pp. 1584–1589. DOI: 10.1002/adma.201305172 (cited on page 7).

[47] Wan-Jian Yin, Tingting Shi, and Yanfa Yan. "Unusual defect physics in CH3NH3PbI3 perovskite solar cell absorber." In: *Applied Physics Letters* 104.6 (2014), p. 63903. DOI: 10.1063/1.4864778 (cited on page 8).

[48] Jun Kang and Lin-Wang Wang. "High Defect Tolerance in Lead Halide Perovskite CsPbBr3." In: *J. Phys. Chem. Lett.* 8.2 (2017), pp. 489–493. DOI: 10.1021/acs.jpclett.6b02800 (cited on page 8).

[49] D. Indjin. "Optical properties of quantum wells." In: *Quantum Wells, Wires and Dots*. 2016, pp. 379–406. DOI: 10.1002/9781118923337.ch11 (cited on page 13).

[50] Aurelien David and Benton Miller. "Optical physics of quantum wells." In: *Quantum Dynamics of Simple Systems* (2020) (cited on page 14).

[51] P. K. Basu, ed. *Theory of Optical Processes in Semiconductors: Bulk and Microstructures*. Oxford University Press, 2003 (cited on page 16).

[52] R. R. Guseinov. "Coulomb Interaction and Excitons in a Superlattice." In: *physica status solidi (b)* 125.1 (1984), pp. 237–243. DOI: 10.1002/pssb.2221250128 (cited on page 17).

[53] Teruya Ishihara, Jun Takahashi, and Takenari Goto. "Exciton state in two-dimensional perovskite semiconductor (C10H21NH3)2PbI4." In: *Solid State Communications* 69.9 (1989), pp. 933–936. DOI: 10.1016/0038-1098(89)90935-6 (cited on page 17).

[54] Jasmina A. Sichert, Yu Tong, Niklas Mutz, Mathias Vollmer, Stefan Fischer, Karolina Z. Milowska, Ramon García Cortadella, Bert Nickel, Carlos Cardenas-Daw, Jacek K. Stolarczyk, Alexander S. Urban, and Jochen Feldmann. "Quantum Size Effect in Organometal Halide Perovskite Nanoplatelets." In: *Nano Lett* 15.10 (2015), pp. 6521–6527. DOI: 10.1021/acs.nanolett.5b02985 (cited on pages 17, 34, 56).

[55] Bernhard J. Bohn, Yu Tong, Moritz Gramlich, May Ling Lai, Markus Döblinger, Kun Wang, Robert L. Z. Hoye, Peter Müller-Buschbaum, Samuel D. Stranks, Alexander S. Urban, Lakshminarayana Polavarapu, and Jochen Feldmann. "Boosting Tunable Blue Luminescence of Halide Perovskite Nanoplatelets through Postsynthetic Surface Trap Repair." In: *Nano Lett* 18.8 (2018), pp. 5231–5238. DOI: 10.1021/acs.nanolett.8b02190 (cited on pages 17, 56, 63).

[56] Muhammad Imran, Palvasha Ijaz, Dmitry Baranov, Luca Goldoni, Urko Petralanda, Quinten Akkerman, Ahmed L. Abdelhady, Mirko Prato, Paolo Bianchini, Ivan Infante, and Liberato Manna. "Shape-Pure, Nearly Monodispersed CsPbBr3 Nanocubes Prepared Using Secondary Aliphatic Amines." In: *Nano Lett* 18.12 (2018), pp. 7822–7831. DOI: 10.1021/acs.nanolett.8b03598 (cited on page 18).

[57] Franziska Krieg, Peter C. Sercel, Max Burian, Hordii Andrusiv, Maryna I. Bodnarchuk, Thilo Stöferle, Rainer F. Mahrt, Denys Naumenko, Heinz Amenitsch, Gabriele Rainò, and Maksym V. Kovalenko. "Monodisperse Long-Chain Sulfobetaine-Capped CsPbBr3 Nanocrystals and Their Superfluorescent Assemblies." In: *ACS Central Science* 7.1 (2021), pp. 135–144. DOI: 10.1021/acscentsci.0c01153 (cited on page 18).

[58] Giles E. Eperon, Severin N. Habisreutinger, Tomas Leijtens, Bardo J. Bruijnaers, Jacobus J. van Franeker, Dane W. deQuilettes, Sandeep Pathak, Rebecca J. Sutton, Giulia Grancini, David S. Ginger, Rene A. J. Janssen, Annamaria Petrozza, and Henry J. Snaith. "The Importance of Moisture in Hybrid Lead Halide Perovskite Thin Film Fabrication." In: *ACS Nano* 9.9 (2015), pp. 9380–9393. DOI: 10.1021/acsnano.5b03626 (cited on page 19).

[59] Filipp Temerov, Yasmine Baghdadi, Ed Rattner, and Salvador Eslava. "A Review on Halide Perovskite-Based Photocatalysts: Key Factors and Challenges." In: *ACS Applied Energy Materials* 5.12 (2022), pp. 14605–14637. DOI: 10.1021/acsaem.2c02680 (cited on page 19).

[60] Qixuan Zhong, Muhan Cao, Huicheng Hu, Di Yang, Min Chen, Pengli Li, Linzhong Wu, and Qiao Zhang. "One-Pot Synthesis of Highly Stable CsPbBr3@SiO2 Core–Shell Nanoparticles." In: *ACS Nano* 12.8 (2018), pp. 8579–8587. DOI: 10.1021/acsnano.8b04209 (cited on page 19).

[61] Hung-Chia Wang, Shin-Ying Lin, An-Cih Tang, Bheeshma Pratap Singh, Hung-Chun Tong, Ching-Yi Chen, Yu-Chun Lee, Tzong-Liang Tsai, and Ru-Shi Liu. "Mesoporous Silica Particles Integrated with All-Inorganic CsPbBr3 Perovskite Quantum-Dot Nanocomposites (MP-PQDs) with High Stability and Wide Color Gamut Used for Backlight Display." In: *Angewandte Chemie International Edition* 55.28 (2016), pp. 7924–7929. DOI: 10.1002/anie.201603698 (cited on page 19).

[62] Daqin Chen, Gaoliang Fang, and Xiao Chen. "Silica-Coated Mn-Doped CsPb(Cl/Br)3 Inorganic Perovskite Quantum Dots: Exciton-to-Mn Energy Transfer and Blue-Excitable Solid-State Lighting." In: *ACS Appl. Mater. Interfaces* 9.46 (2017), pp. 40477–40487. DOI: 10.1021/acsami.7b14471 (cited on page 19).

[63] Tianshu Li, Xingang Zhao, Dongwen Yang, Mao-Hua Du, and Lijun Zhang. "Intrinsic Defect Properties in Halide Double Perovskites for Optoelectronic Applications." In: *Phys. Rev. Appl.* 10.4 (2018), p. 41001. DOI: 10.1103/PhysRevApplied.10.041001 (cited on pages 19, 69, 73).

[64] Anna Loiudice, Seryio Saris, Emad Oveisi, Duncan T. L. Alexander, and Raffaella Buonsanti. "CsPbBr3 QD/AlOx Inorganic Nanocomposites with Exceptional Stability in Water, Light, and Heat." In: *Angewandte Chemie International Edition* 56.36 (2017), pp. 10696–10701. DOI: 10.1002/anie.201703703 (cited on page 19).

[65] He Huang, Bingkun Chen, Zhenguang Wang, Tak Fu Hung, Andrei S. Susha, Haizheng Zhong, and Andrey L. Rogach. "Water resistant CsPbX3 nanocrystals coated with polyhedral oligomeric silsesquioxane and their use as solid state luminophores in all-perovskite white light-emitting devices." In: *Chemical Science* 7.9 (2016), pp. 5699–5703. DOI: 10.1039/C6SC01758D (cited on page 19).

[66] Christian Müller, Tobias Glaser, Marcel Plogmeyer, Michael Sendner, Sebastian Döring, Artem A. Bakulin, Carlo Brzuska, Roland Scheer, Maxim S. Pshenichnikov, Wolfgang Kowalsky, Annemarie Pucci, and Robert Lovrinčić. "Water Infiltration in Methylammonium Lead Iodide Perovskite: Fast and Inconspicuous." In: *Chem. Mater.* 27.22 (2015), pp. 7835–7841. DOI: 10.1021/acs.chemmater.5b03883 (cited on page 19).

[67] Edward Barry, Raelyn Burns, Wei Chen, Guilhem X. de Hoe, Joan Manuel Montes de Oca, Juan J. de Pablo, James Dombrowski, Jeffrey W. Elam, Alanna M. Felts, Giulia Galli, John Hack, Qiming He, Xiang He, Eli Hoenig, Aysenur Iscen, Benjamin Kash, Harold H. Kung, Nicholas H. C. Lewis, Chong Liu, Xinyou Ma, Anil Mane, Alex B. F. Martinson, Karen L. Mulfort, Julia Murphy, Kristian Mølhave, Paul Nealey, Yijun Qiao, Vepa Rozyyev, George C. Schatz, Steven J. Sibener, Dmitri Talapin, David M. Tiede, Matthew V. Tirrell, Andrei Tokmakoff, Gregory A. Voth, Zhongyang Wang, Zifan Ye, Murat Yesibolati, Nestor J. Zaluzec, and Seth B. Darling. "Advanced Materials for Energy-Water Systems: The Central Role of Water/Solid Interfaces in Adsorption, Reactivity, and Transport." In: *Chem. Rev.* 121.15 (2021), pp. 9450–9501. DOI: 10.1021/acs.chemrev.1c00069 (cited on page 19).

[68] Junming Li, Hai-Lei Cao, Wen-Bin Jiao, Qiong Wang, Mingdeng Wei, Irene Cantone, Jian Lü, and Antonio Abate. "Biological impact of lead from halide perovskites reveals the risk of introducing a safe threshold." In: *Nature Communications* 11.1 (2020), p. 310. DOI: 10.1038/s41467-019-13910-y (cited on page 20).

[69] Nakita K. Noel, Samuel D. Stranks, Antonio Abate, Christian Wehrenfennig, Simone Guarnera, Amir-Abbas Haghighirad, Aditya Sadhanala, Giles E. Eperon, Sandeep K. Pathak, Michael B. Johnston, Annamaria Petrozza, Laura M. Herz, and Henry J. Snaith. "Lead-free organic–inorganic tin halide perovskites for photovoltaic applications." In: *Energy & Environmental Science* 7.9 (2014), pp. 3061–3068. DOI: 10.1039/C4EE01076K (cited on page 20).

[70] Marina R. Filip and Feliciano Giustino. "Computational Screening of Homovalent Lead Substitution in Organic–Inorganic Halide Perovskites." In: *The Journal of Physical Chemistry C* 120.1 (2016), pp. 166–173. DOI: 10.1021/acs.jpcc.5b11845 (cited on pages 20, 23).

[71] Sukanya Ghosh, Hari Shankar, and Prasenjit Kar. "Recent developments of lead-free halide double perovskites: a new superstar in the optoelectronic field." In: *Materials Advances* 3.9 (2022), pp. 3742–3765. DOI: 10.1039/D2MA00071G (cited on pages 20, 22).

[72] Hari Shankar, Sukanya Ghosh, and Prasenjit Kar. "Highly stable blue fluorescent lead free all-inorganic Cs2ZnX4 2D perovskite nanocrystals." In: *Journal of Alloys and Compounds* 844 (2020), p. 156148. DOI: 10.1016/j.jallcom.2020.156148 (cited on page 20).

[73] Abhoy Karmakar, Srija Mukhopadhyay, Pierre G. B. Gachod, Victor Arturo Mora-Gomez, Guy M. Bernard, Alex Brown, and Vladimir K. Michaelis. "Uncovering Halogen Mixing and Octahedral Dynamics in Cs2SnX6 by Multinuclear Magnetic Resonance Spectroscopy." In: *Chem. Mater.* 33.15 (2021), pp. 6078–6090. DOI: 10.1021/acs.chemmater.1c01561 (cited on page 20).

[74] Ankit Jain, Oleksandr Voznyy, and Edward H. Sargent. "High-Throughput Screening of Lead-Free Perovskite-like Materials for Optoelectronic Applications." In: *The Journal of Physical Chemistry C* 121.13 (2017), pp. 7183–7187. DOI: 10.1021/acs.jpcc.7b02221 (cited on page 20).

[75] Yanming Sun, Alberto José Fernández-Carrión, Yunhui Liu, Congling Yin, Xing Ming, Bo-Mei Liu, Jing Wang, Hui Fu, Xiaojun Kuang, and Xianran Xing. "Bismuth-Based Halide Double Perovskite Cs2LiBiCl6: Crystal Structure, Luminescence, and Stability." In: *Chem. Mater.* 33.15 (2021), pp. 5905–5916. DOI: 10.1021/acs.chemmater.1c00854 (cited on page 21).

[76] Adam D. Wright, Leonardo R. V. Buizza, Kimberley J. Savill, Giulia Longo, Henry J. Snaith, Michael B. Johnston, and Laura M. Herz. "Ultrafast Excited-State Localization in Cs2AgBiBr6 Double Perovskite." In: *The Journal of Physical Chemistry Letters* 12.13 (2021), pp. 3352–3360. DOI: 10.1021/acs.jpclett.1c00653 (cited on pages 21, 23, 25).

[77] Ryszard Jakubas, Jacek Zaleski, and Lucjan Sobczyk. "Phase transitions in (CH3NH3)3Bi2I9 (MAIB)." In: *Ferroelectrics* 108.1 (1990), pp. 109–114. DOI: 10.1080/00150199008018741 (cited on page 22).

[78] Shijing Sun, Satoshi Tominaka, Jung-Hoon Lee, Fei Xie, Paul D. Bristowe, and Anthony K. Cheetham. "Synthesis, crystal structure, and properties of a perovskite-related bismuth phase, (NH4)3Bi2I9." In: *APL Materials* 4.3 (2016), p. 031101. DOI: 10.1063/1.4943680 (cited on page 22).

[79] George Volonakis, Marina R. Filip, Amir Abbas Haghighirad, Nobuya Sakai, Bernard Wenger, Henry J. Snaith, and Feliciano Giustino. "Lead-Free Halide Double Perovskites via Heterovalent Substitution of Noble Metals." In: *The Journal of Physical Chemistry Letters* 7.7 (2016), pp. 1254–1259. DOI: 10.1021/acs.jpclett.6b00376 (cited on page 22).

[80] Md Roknuzzaman, Chunmei Zhang, Kostya Ostrikov, Aijun Du, Hongxia Wang, Lianzhou Wang, and Tuquabo Tesfamichael. "Electronic and optical properties of lead-free hybrid double perovskites for photovoltaic and optoelectronic applications." In: *Scientific Reports* 9.1 (2019), p. 718. DOI: 10.1038/s41598-018-37132-2 (cited on page 22).

[81] Gerd Meyer. "The synthesis and structures of complex rare-earth halides." In: *Progress in Solid State Chemistry* 14.3 (1982), pp. 141–219. DOI: 10.1016/0079-6786(82)90005-X (cited on page 22).

[82] W.M.A. Smit, G. J. Dirksen, and D. J. Stufkens. "Infrared and Raman spectra of the elpasolites Cs2NaSbCl6 and Cs2NaBiCl6: Evidence for a pseudo Jahn-Teller distorted ground state." In: *Journal of Physics and Chemistry of Solids* 51.2 (1990), pp. 189–196. DOI: 10.1016/0022-3697(90)90092-T (cited on page 22).

[83] Eric T. McClure, Molly R. Ball, Wolfgang Windl, and Patrick M. Woodward. "Cs2AgBiX6 (X = Br, Cl): New Visible Light Absorbing, Lead-Free Halide Perovskite Semiconductors." In: *Chem. Mater.* 28.5 (2016), pp. 1348–1354. DOI: 10.1021/acs.chemmater.5b04231 (cited on pages 22, 23).

[84] Fengxia Wei, Zeyu Deng, Shijing Sun, Fei Xie, Gregor Kieslich, Donald M. Evans, Michael A. Carpenter, Paul D. Bristowe, and Anthony K. Cheetham. "The synthesis, structure and electronic properties of a lead-free hybrid inorganic–organic double perovskite (MA)2KBiCl6 (MA = methylammonium)." In: *Materials Horizons* 3.4 (2016), pp. 328–332. DOI: 10.1039/C6MH00053C (cited on page 22).

[85] Fengxia Wei, Zeyu Deng, Shijing Sun, Fenghua Zhang, Donald M. Evans, Gregor Kieslich, Satoshi Tominaka, Michael A. Carpenter, Jie Zhang, Paul D. Bristowe, and Anthony K. Cheetham. "Synthesis and Properties of a Lead-Free Hybrid Double Perovskite: (CH3NH3)2AgBiBr6." In: *Chem. Mater.* 29.3 (2017), pp. 1089–1094. DOI: 10.1021/acs.chemmater.6b03944 (cited on page 22).

[86] Zewen Xiao, Zhaoning Song, and Yanfa Yan. "From Lead Halide Perovskites to Lead-Free Metal Halide Perovskites and Perovskite Derivatives." In: *Advanced Materials* 31.47 (2019), p. 1803792. DOI: 10.1002/adma.201803792 (cited on page 22).

[87] Sidney E. Creutz, Evan N. Crites, Michael C. de Siena, and Daniel R. Gamelin. "Colloidal Nanocrystals of Lead-Free Double-Perovskite (Elpasolite) Semiconductors: Synthesis and Anion Exchange To Access New Materials." In: *Nano Lett* 18.2 (2018), pp. 1118–1123. DOI: 10.1021/acs.nanolett.7b04659 (cited on page 23).

[88] Amrita Dey, Alexander F. Richter, Tushar Debnath, He Huang, Lakshminarayana Polavarapu, and Jochen Feldmann. "Transfer of Direct to Indirect Bound Excitons by Electron Intervalley Scattering in Cs2AgBiBr6 Double Perovskite Nanocrystals." In: *ACS Nano* 14.5 (2020), pp. 5855–5861. DOI: 10.1021/acsnano.0c00997 (cited on pages 23, 25, 34, 69, 74).

[89] Davide Bartesaghi, Adam H. Slavney, María C. Gélvez-Rueda, Bridget A. Connor, Ferdinand C. Grozema, Hemamala I. Karunadasa, and Tom J. Savenije. "Charge Carrier Dynamics in Cs2AgBiBr6 Double Perovskite." In: *The Journal of Physical Chemistry C* 122.9 (2018), pp. 4809–4816. DOI: 10.1021/acs.jpcc.8b00572 (cited on pages 24, 25).

[90] Yu Bi, Eline M. Hutter, Yanjun Fang, Qingfeng Dong, Jinsong Huang, and Tom J. Savenije. "Charge Carrier Lifetimes Exceeding 15 ms in Methylammonium Lead Iodide Single Crystals." In: *The Journal of Physical Chemistry Letters* 7.5 (2016), pp. 923–928. DOI: 10.1021/acs.jpclett.6b00269 (cited on page 24).

[91] Wenmei Ming, Shiyou Chen, and Mao-Hua Du. "Chemical instability leads to unusual chemical-potential-independent defect formation and diffusion in perovskite solar cell material CH3NH3PbI3." In: *Journal of Materials Chemistry A* 4.43 (2016), pp. 16975–16981. DOI: 10.1039/C6TA07492H (cited on page 24).

[92] Zhi-Jun Li, Elan Hofman, Jian Li, Andrew Hunter Davis, Chen-Ho Tung, Li-Zhu Wu, and Weiwei Zheng. "Photoelectrochemically Active and Environmentally Stable CsPbBr3/TiO2 Core/Shell Nanocrystals." In: *Advanced Functional Materials* 28.1 (2018), p. 1704288. DOI: 10.1002/adfm.201704288 (cited on page 24).

[93] Enrico Greul, Michiel L. Petrus, Andreas Binek, Pablo Docampo, and Thomas Bein. "Highly stable, phase pure Cs2AgBiBr6 double perovskite thin films for optoelectronic applications." In: *Journal of Materials Chemistry A* 5.37 (2017), pp. 19972–19981. DOI: 10.1039/C7TA06816F (cited on page 25).

[94] Liping Yu and Alex Zunger. "Identification of Potential Photovoltaic Absorbers Based on First-Principles Spectroscopic Screening of Materials." In: *Physical Review Letters* 108.6 (2012), p. 068701. DOI: 10.1103/PhysRevLett.108.068701 (cited on page 25).

[95] Christopher N. Savory, Aron Walsh, and David O. Scanlon. "Can Pb-Free Halide Double Perovskites Support High-Efficiency Solar Cells?" In: *ACS Energy Letters* 1.5 (2016), pp. 949–955. DOI: 10.1021/acsenergylett.6b00471 (cited on page 25).

[96] Raman Singh Lamba, Pooja Basera, Sahil Singh, Saswata Bhattacharya, and Sameer Sapra. "Lead-Free Alloyed Double-Perovskite Nanocrystals of Cs2(NaxAg1−x)BiBr6 with Tunable Band Gap." In: *The Journal of Physical Chemistry C* 125.3 (2021), pp. 1954–1962. DOI: 10.1021/acs.jpcc.0c09554 (cited on page 25).

[97] Bao Ke, Ruosheng Zeng, Zhuang Zhao, Qilin Wei, Xiaogang Xue, Kun Bai, Chunxiao Cai, Weichang Zhou, Zhiguo Xia, and Bingsuo Zou. "Homo- and Heterovalent Doping-Mediated Self-Trapped Exciton Emission and Energy Transfer in Mn-Doped Cs2Na1−xAgxBiCl6 Double Perovskites." In: *The Journal of Physical Chemistry Letters* 11.1 (2020), pp. 340–348. DOI: 10.1021/acs.jpclett.9b03387 (cited on page 25).

[98] Na Chen, Tong Cai, Wenhao Li, Katie Hills-Kimball, Hanjun Yang, Meidan Que, Yasutaka Nagaoka, Zhenyang Liu, Dong Yang, Angang Dong, Cheng-Yan Xu, Rashid Zia, and Ou Chen. "Yb- and Mn-Doped Lead-Free Double Perovskite Cs2AgBiX6 (X = Cl−, Br−) Nanocrystals." In: *ACS Appl. Mater. Interfaces* 11.18 (2019), pp. 16855–16863. DOI: 10.1021/acsami.9b02367 (cited on page 25).

[99] Julian A. Steele, Pascal Puech, Masoumeh Keshavarz, Ruoxi Yang, Subhasree Banerjee, Elke Debroye, Cheol Woong Kim, Haifeng Yuan, Nam Ho Heo, Johan Vanacken, Aron Walsh, Johan Hofkens, and Maarten B. J. Roeffaers. "Giant Electron–Phonon Coupling and Deep Conduction Band Resonance in Metal Halide Double Perovskite." In: *ACS Nano* 12.8 (2018), pp. 8081–8090. DOI: 10.1021/acsnano.8b02936 (cited on page 25).

[100] Wei Zheng, Ruijia Sun, Yeqi Liu, Xiaojia Wang, Nianqiao Liu, Yanchen Ji, Liangling Wang, Hong Liu, and Yuhai Zhang. "Excitation Management of Lead-Free Perovskite Nanocrystals Through Doping." In: *ACS Appl. Mater. Interfaces* 13.5 (2021), pp. 6404–6410. DOI: 10.1021/acsami.0c20230 (cited on page 25).

[101] S. J. Zelewski, J. M. Urban, A. Surrente, D. K. Maude, A. Kuc, L. Schade, R. D. Johnson, M. Dollmann, P. K. Nayak, H. J. Snaith, P. Radaelli, R. Kudrawiec, R. J. Nicholas, P. Plochocka, and M. Baranowski. "Revealing the nature of photoluminescence emission in the metal-halide double perovskite Cs2AgBiBr6." In: *Journal of Materials Chemistry C* 7.27 (2019), pp. 8350–8356. DOI: 10.1039/C9TC02402F (cited on page 25).

[102] Zewen Xiao, Weiwei Meng, Jianbo Wang, and Yanfa Yan. "Thermodynamic Stability and Defect Chemistry of Bismuth-Based Lead-Free Double Perovskites." In: *ChemSusChem* 9.18 (2016), pp. 2628–2633. DOI: 10.1002/cssc.201600771 (cited on page 25).

[103] AKIRA FUJISHIMA and KENICHI HONDA. "Electrochemical Photolysis of Water at a Semiconductor Electrode." In: *Nature* 238.5358 (1972), pp. 37–38. DOI: 10.1038/238037a0 (cited on pages 27, 30).

[104] Allen J. Bard. "Photoelectrochemistry." In: *Science* 207.4427 (1980), pp. 139–144. DOI: 10.1126/science.207.4427.139 (cited on page 27).

[105] Shan Wang, Aolin Lu, and Chuan-Jian Zhong. "Hydrogen production from water electrolysis: role of catalysts." In: *Nano Convergence* 8.1 (2021), p. 4. DOI: 10.1186/s40580-021-00254-x (cited on page 29).

[106] Rengui Li and Can Li. "Chapter One - Photocatalytic Water Splitting on Semiconductor-Based Photocatalysts." In: *Advances in Catalysis*. Ed. by Chunshan Song. Vol. 60. Academic Press, 2017, pp. 1–57. DOI: 10.1016/bs.acat.2017.09.001 (cited on page 29).

[107] Hongjian Yan, Jinhui Yang, Guijun Ma, Guopeng Wu, Xu Zong, Zhibin Lei, Jingying Shi, and Can Li. "Visible-light-driven hydrogen production with extremely high quantum efficiency on Pt–PdS/CdS photocatalyst." In: *Journal of Catalysis* 266.2 (2009), pp. 165–168. DOI: 10.1016/j.jcat.2009.06.024 (cited on page 29).

[108] G. N. Schrauzer and T. D. Guth. "Photolysis of Water and Photoreduction of Nitrogen on Titanium Dioxide." In: *J. Am. Chem. Soc.* 99.22 (1977), pp. 7189–7193. DOI: 10.1021/ja00464a015 (cited on page 29).

[109] Takuya Suguro, Fuminao Kishimoto, and Kazuhiro Takanabe. "Photocatalytic Hydrogen Production under Water Vapor Feeding□A Minireview." In: *Energy & Fuels* 36.16 (2022), pp. 8978–8994. DOI: 10.1021/acs.energyfuels.2c01478 (cited on page 30).

[110] V. Preethi and S. Kanmani. "Performance of gas-phase photocatalytic reactors on hydrogen production." In: *International Journal of Hydrogen Energy* 42.14 (2017), pp. 8997–9002. DOI: 10.1016/j.ijhydene.2016.05.245 (cited on page 30).

[111] Kayla Alicia Davis, Sunghoon Yoo, Eric W. Shuler, Benjamin D. Sherman, Seunghyun Lee, and Gyu Leem. "Photocatalytic hydrogen evolution from biomass conversion." In: *Nano Convergence* 8.1 (2021), p. 6. DOI: 10.1186/s40580-021-00256-9 (cited on page 30).

[112] Xiaobo Chen, Shaohua Shen, Liejin Guo, and Samuel S. Mao. "Semiconductor-based Photocatalytic Hydrogen Generation." In: *Chem. Rev.* 110.11 (2010), pp. 6503–6570. DOI: 10.1021/cr1001645 (cited on page 30).

[113] Chethana Gadiyar, Anna Loiudice, and Raffaella Buonsanti. "Colloidal nanocrystals for photoelectrochemical and photocatalytic water splitting." In: *Journal of Physics D: Applied Physics* 50.7 (2017), p. 074006. DOI: 10.1088/1361-6463/aa50cd (cited on page 30).

[114] Zhiji Han, Fen Qiu, Richard Eisenberg, Patrick L. Holland, and Todd D. Krauss. "Robust Photogeneration of H2 in Water Using Semiconductor Nanocrystals and a Nickel Catalyst." In: *Science* 338.6112 (2012), pp. 1321–1324. DOI: 10.1126/science.1227775 (cited on page 30).

[115] Yuval Ben-Shahar, Francesco Scotognella, Ilka Kriegel, Luca Moretti, Giulio Cerullo, Eran Rabani, and Uri Banin. "Optimal metal domain size for photocatalysis with hybrid semiconductor-metal nanorods." In: *Nature Communications* 7.1 (2016), p. 10413. DOI: 10.1038/ncomms10413 (cited on page 30).

[116] Jacek K. Stolarczyk, Santanu Bhattacharyya, Lakshminarayana Polavarapu, and Jochen Feldmann. "Challenges and Prospects in Solar Water Splitting and CO2 Reduction with Inorganic and Hybrid Nanostructures." In: *ACS Catalysis* 8.4 (2018), pp. 3602–3635. DOI: 10.1021/acscatal.8b00791 (cited on page 30).

[117] Thomas Simon, Michael T. Carlson, Jacek K. Stolarczyk, and Jochen Feldmann. "Electron Transfer Rate vs Recombination Losses in Photocatalytic H2 Generation on Pt-Decorated CdS Nanorods." In: *ACS Energy Letters* 1.6 (2016), pp. 1137–1142. DOI: 10.1021/acsenergylett.6b00468 (cited on page 30).

[118] Lilac Amirav and A. Paul Alivisatos. "Photocatalytic Hydrogen Production with Tunable Nanorod Heterostructures." In: *The Journal of Physical Chemistry Letters* 1.7 (2010), pp. 1051–1054. DOI: 10.1021/jz100075c (cited on page 30).

[119] Jiawen Fang, Tushar Debnath, Santanu Bhattacharyya, Markus Döblinger, Jochen Feldmann, and Jacek K. Stolarczyk. "Photobase effect for just-in-time delivery in photocatalytic hydrogen generation." In: *Nature Communications* 11.1 (2020), p. 5179. DOI: 10.1038/s41467-020-18583-6 (cited on page 31).

[120] Yaqiang Wu, Peng Wang, Zihan Guan, Junxue Liu, Zeyan Wang, Zhaoke Zheng, Shengye Jin, Ying Dai, Myung-Hwan Whangbo, and Baibiao Huang. "Enhancing the Photocatalytic Hydrogen Evolution Activity of Mixed-Halide Perovskite CH3NH3PbBr3−xIx Achieved by Bandgap Funneling of Charge Carriers." In: *ACS Catalysis* 8.11 (2018), pp. 10349–10357. DOI: 10.1021/acscatal.8b02374 (cited on page 31).

[121] Yang-Fan Xu, Xu-Dong Wang, Jin-Feng Liao, Bai-Xue Chen, Hong-Yan Chen, and Dai-Bin Kuang. "Amorphous-TiO2-Encapsulated CsPbBr3 Nanocrystal Composite Photocatalyst with Enhanced Charge Separation and CO2 Fixation." In: *Advanced Materials Interfaces* 5.22 (2018), p. 1801015. DOI: 10.1002/admi.201801015 (cited on page 32).

[122] Yan-Fei Mu, Wen Zhang, Xiao-Xuan Guo, Guang-Xing Dong, Min Zhang, and Tong-Bu Lu. "Water-Tolerant Lead Halide Perovskite Nanocrystals as Efficient Photocatalysts for Visible-Light-Driven CO2 Reduction in Pure Water." In: *ChemSusChem* 12.21 (2019), pp. 4769–4774. DOI: 10.1002/cssc.201902192 (cited on page 32).

[123] Teresa García, Rocío García-Aboal, Josep Albero, Pedro Atienzar, and Hermenegildo García. "Vapor-Phase Photocatalytic Overall Water Splitting Using Hybrid Methylammonium Copper and Lead Perovskites." In: *Nanomaterials* 10.5 (2020). DOI: 10.3390/nano10050960 (cited on page 32).

[124] "Lead Halide Perovskite Nanocrystals: From Discovery to Self-assembly and Applications." In: *CHIMIA* 71.7-8 (2017), p. 461. DOI: 10.2533/chimia.2017.461 (cited on page 34).

[125] He Ren, Yue Wu, Chenchen Wang, and Yong Yan. "2D Perovskite Nanosheets with Intrinsic Chirality." In: *J. Phys. Chem. Lett.* 12.10 (2021), pp. 2676–2681. DOI: 10.1021/acs.jpclett.1c00315 (cited on page 34).

[126] Dandan Zhang, Yi Yu, Yehonadav Bekenstein, Andrew B. Wong, A. Paul Alivisatos, and Peidong Yang. "Ultrathin Colloidal Cesium Lead Halide Perovskite Nanowires." In: *J. Am. Chem. Soc.* 138.40 (2016), pp. 13155–13158. DOI: 10.1021/jacs.6b08373 (cited on page 34).

[127] Javad Shamsi, Alexander S. Urban, Muhammad Imran, Luca de Trizio, and Liberato Manna. "Metal Halide Perovskite Nanocrystals: Synthesis, Post-Synthesis Modifications, and Their Optical Properties." In: *Chem. Rev.* 119.5 (2019), pp. 3296–3348. DOI: 10.1021/acs.chemrev.8b00644 (cited on pages 34, 37).

[128] Loredana Protesescu, Sergii Yakunin, Olga Nazarenko, Dmitry N. Dirin, and Maksym V. Kovalenko. "Low-Cost Synthesis of Highly Luminescent Colloidal Lead Halide Perovskite Nanocrystals by Wet Ball Milling." In: *ACS Appl. Nano Mater.* 1.3 (2018), pp. 1300–1308. DOI: 10.1021/acsanm.8b00038 (cited on page 34).

[129] Verena A. Hintermayr, Alexander F. Richter, Florian Ehrat, Markus Döblinger, Willem Vanderlinden, Jasmina A. Sichert, Yu Tong, Lakshminarayana Polavarapu, Jochen Feldmann, and Alexander S. Urban. "Tuning the Optical Properties of Perovskite Nanoplatelets through Composition and Thickness by Ligand-Assisted Exfoliation." In: *Advanced Materials* 28.43 (2016), pp. 9478–9485. DOI: 10.1002/adma.201602897 (cited on page 34).

[130] Yu Tong, Eva Bladt, Meltem F. Aygüler, Aurora Manzi, Karolina Z. Milowska, Verena A. Hintermayr, Pablo Docampo, Sara Bals, Alexander S. Urban, Lakshminarayana Polavarapu, and Jochen Feldmann. "Highly Luminescent Cesium Lead Halide Perovskite Nanocrystals with Tunable Composition and Thickness by Ultrasonication." In: *Angewandte Chemie International Edition* 55.44 (2016), pp. 13887–13892. DOI: 10.1002/anie.201605909 (cited on pages 34, 35).

[131] Kasturi Muthoosamy and Sivakumar Manickam. "State of the art and recent advances in the ultrasound-assisted synthesis, exfoliation and functionalization of graphene derivatives." In: *Ultrasonics Sonochemistry* 39 (2017), pp. 478–493. DOI: 10.1016/j.ultsonch.2017.05.019 (cited on page 35).

[132] Hangxun Xu, Brad W. Zeiger, and Kenneth S. Suslick. "Sonochemical synthesis of nanomaterials." In: *Chem. Soc. Rev.* 42.7 (2013), pp. 2555–2567. DOI: 10.1039/C2CS35282F (cited on page 35).

[133] Jin Ho Bang and Kenneth S. Suslick. "Applications of Ultrasound to the Synthesis of Nanostructured Materials." In: *Advanced Materials* 22.10 (2010), pp. 1039–1059. DOI: 10.1002/adma.200904093 (cited on page 35).

[134] Yu Tong, Bernhard J. Bohn, Eva Bladt, Kun Wang, Peter Müller-Buschbaum, Sara Bals, Alexander S. Urban, Lakshminarayana Polavarapu, and Jochen Feldmann. "From Precursor Powders to CsPbX3 Perovskite Nanowires: One-Pot Synthesis, Growth Mechanism, and Oriented Self-Assembly." In: *Angewandte Chemie International Edition* 56.44 (2017), pp. 13887–13892. DOI: 10.1002/anie.201707224 (cited on page 35).

[135] Yu Tong, En-Ping Yao, Aurora Manzi, Eva Bladt, Kun Wang, Markus Döblinger, Sara Bals, Peter Müller-Buschbaum, Alexander S. Urban, Lakshminarayana Polavarapu, and Jochen Feldmann. "Spontaneous Self-Assembly of Perovskite Nanocrystals into Electronically Coupled Supercrystals: Toward Filling the Green Gap." In: *Advanced Materials* 30.29 (2018), p. 1801117. DOI: 10.1002/adma.201801117 (cited on page 35).

[136] Dmitri V. Talapin, Jong-Soo Lee, Maksym V. Kovalenko, and Elena V. Shevchenko. "Prospects of Colloidal Nanocrystals for Electronic and Optoelectronic Applications." In: *Chem. Rev.* 110.1 (2010), pp. 389–458. DOI: 10.1021/cr900137k (cited on page 36).

[137] Nguyen T. K. Thanh, N. Maclean, and S. Mahiddine. "Mechanisms of Nucleation and Growth of Nanoparticles in Solution." In: *Chem. Rev.* 114.15 (2014), pp. 7610–7630. DOI: 10.1021/cr400544s (cited on page 36).

[138] Franziska Krieg, Stefan T. Ochsenbein, Sergii Yakunin, Stephanie ten Brinck, Philipp Aellen, Adrian Süess, Baptiste Clerc, Dominic Guggisberg, Olga Nazarenko, Yevhen Shynkarenko, Sudhir Kumar, Chih-Jen Shih, Ivan Infante, and Maksym V. Kovalenko. "Colloidal CsPbX3 (X = Cl, Br, I) Nanocrystals 2.0: Zwitterionic Capping Ligands for Improved Durability and Stability." In: *ACS Energy Lett* 3.3 (2018), pp. 641–646. DOI: 10.1021/acsenergylett.8b00035 (cited on page 38).

[139] Franziska Krieg, Quy K. Ong, Max Burian, Gabriele Rainò, Denys Naumenko, Heinz Amenitsch, Adrian Süess, Matthias J. Grotevent, Frank Krumeich, Maryna I. Bodnarchuk, Ivan Shorubalko, Francesco Stellacci, and Maksym V. Kovalenko. "Stable Ultraconcentrated and Ultradilute Colloids of CsPbX3 (X = Cl, Br) Nanocrystals Using Natural Lecithin as a Capping Ligand." In: *J. Am. Chem. Soc.* 141.50 (2019), pp. 19839–19849. DOI: 10.1021/jacs.9b09969 (cited on page 38).

[140] Heinz-Helmut Perkampus. "Principles." In: *UV-VIS Spectroscopy and Its Applications*. Ed. by Heinz-Helmut Perkampus. Berlin, Heidelberg: Springer Berlin Heidelberg, 1992, pp. 3–9. DOI: 10.1007/978-3-642-77477-5{\textunderscore}2 (cited on page 39).

[141] Rudi Berera, Rienk van Grondelle, and John T. M. Kennis. "Ultrafast transient absorption spectroscopy: principles and application to photosynthetic systems." In: *Photosynthesis Research* 101.2 (2009), pp. 105–118. DOI: 10.1007/s11120-009-9454-y (cited on page 41).

[142] Ardi Hartono and Inna Kim. "Calculation of Vapor-Liquid Equilibria for Methanol-Water Mixture using Cubic-Plus-Association Equation of State Project work in the subject KP8108 ■Advanced Thermodynamics." In: 2004 (cited on page 50).

[143] Samuel D. Stranks and Henry J. Snaith. "Metal-halide perovskites for photovoltaic and light-emitting devices." In: *Nature Nanotechnology* 10.5 (2015), pp. 391–402. DOI: 10.1038/nnano.2015.90 (cited on page 53).

[144] Chunxiong Bao, Zhongcheng Yuan, Wenxiao Niu, Jie Yang, Zijian Wang, Tao Yu, Jianpu Wang, and Feng Gao. "A multifunctional display based on photo-responsive perovskite light-emitting diodes." In: *Nature Electronics* 7.5 (2024), pp. 375–382. DOI: 10.1038/s41928-024-01151-x (cited on page 53).

[145] Yingjie Tang, Peng Jin, Yan Wang, Dingwei Li, Yitong Chen, Peng Ran, Wei Fan, Kun Liang, Huihui Ren, Xuehui Xu, Rui Wang, Yang Yang, and Bowen Zhu. "Enabling low-drift flexible perovskite photodetectors by electrical modulation for wearable health monitoring and weak light imaging." In: *Nature Communications* 14.1 (2023), p. 4961. DOI: 10.1038/s41467-023-40711-1 (cited on page 53).

[146] Rajdeep Das, Avijit Patra, Sumit Kumar Dutta, Sanjib Shyamal, and Narayan Pradhan. "Facets-Directed Epitaxially Grown Lead Halide Perovskite-Sulfobromide Nanocrystal Heterostructures and Their Improved Photocatalytic Activity." In: *J. Am. Chem. Soc.* 144.40 (2022), pp. 18629–18641. DOI: 10.1021/jacs.2c08639 (cited on page 53).

[147] Meng Liu, Pan Xia, Guohui Zhao, Chengming Nie, Kaimin Gao, Shan He, Lifeng Wang, and Kaifeng Wu. "Energy-Transfer Photocatalysis Using Lead Halide Perovskite Nanocrystals: Sensitizing Molecular Isomerization and Cycloaddition." In: *Angewandte Chemie International Edition* 61.35 (2022), e202208241. DOI: 10.1002/anie.202208241 (cited on page 53).

[148] Kaifeng Wu, Haiming Zhu, Zheng Liu, William Rodríguez-Córdoba, and Tianquan Lian. "Ultrafast Charge Separation and Long-Lived Charge Separated State in Photocatalytic CdS–Pt Nanorod Heterostructures." In: *J. Am. Chem. Soc.* 134.25 (2012), pp. 10337–10340. DOI: 10.1021/ja303306u (cited on pages 59, 60).

[149] Tze Chien Sum, Nripan Mathews, Guichuan Xing, Swee Sien Lim, Wee Kiang Chong, David Giovanni, and Herlina Arianita Dewi. "Spectral Features and Charge Dynamics of Lead Halide Perovskites: Origins and Interpretations." In: *Acc. Chem. Res.* 49.2 (2016), pp. 294–302. DOI: 10.1021/acs.accounts.5b00433 (cited on page 61).

[150] Thomas R. Hopper, Andrei Gorodetsky, Jarvist M. Frost, Christian Müller, Robert Lovrincic, and Artem A. Bakulin. "Ultrafast Intraband Spectroscopy of Hot-Carrier Cooling in Lead-Halide Perovskites." In: *ACS Energy Lett* 3.9 (2018), pp. 2199–2205. DOI: 10.1021/acsenergylett.8b01227 (cited on page 62).

[151] Xiaofeng Lai, Song Wang, Ying Xie, Binghang Liu, Jianhui Sun, Yuxin Li, Haitao Yu, and Kai Pan. "Recycling and Recovery of Deactivated CsPbBr3 Perovskite after Photocatalytic CO2 Reduction Reaction." In: *ACS Appl. Mater. Interfaces* 15.28 (2023), pp. 33712–33720. DOI: 10.1021/acsami.3c07922 (cited on page 63).

[152] Weicheng Pan, Haodi Wu, Jiajun Luo, Zhenzhou Deng, Cong Ge, Chao Chen, Xiaowei Jiang, Wan-Jian Yin, Guangda Niu, Lujun Zhu, Lixiao Yin, Ying Zhou, Qingguo Xie, Xiaoxing Ke, Manling Sui, and Jiang Tang. "Cs2AgBiBr6 single-crystal X-ray detectors with a low detection limit." In: *Nature Photonics* 11.11 (2017), pp. 726–732. DOI: 10.1038/s41566-017-0012-4 (cited on page 67).

[153] Zhe Liu, Weidong Qiu, Xiaomei Peng, Guanwei Sun, Xinyan Liu, Denghui Liu, Zhenchao Li, Fangru He, Chenyang Shen, Qing Gu, Fulong Ma, Hin-Lap Yip, Lintao Hou, Zhengjian Qi, and Shi-Jian Su. "Perovskite Light-Emitting Diodes with EQE Exceeding 28% through a Synergetic Dual-Additive Strategy for Defect Passivation and Nanostructure Regulation." In: *Advanced Materials* 33.43 (2021), p. 2103268. DOI: 10.1002/adma.202103268 (cited on page 67).

[154] Amrita Dey, Pravin Rathod, and Dinesh Kabra. "Role of Localized States in Photoluminescence Dynamics of High Optical Gain CsPbBr3 Nanocrystals." In: *Advanced Optical Materials* 6.11 (2018), p. 1800109. DOI: 10.1002/adom.201800109 (cited on page 70).

[155] Julian A. Steele, Weicheng Pan, Cristina Martin, Masoumeh Keshavarz, Elke Debroye, Haifeng Yuan, Subhasree Banerjee, Eduard Fron, Dries Jonckheere, Cheol Woong Kim, Wouter Baekelant, Guangda Niu, Jiang Tang, Johan Vanacken, Mark van der Auweraer, Johan Hofkens, and Maarten B. J. Roeffaers. "Photophysical Pathways in Highly Sensitive Cs2AgBiBr6 Double-Perovskite Single-Crystal X-Ray Detectors." In: *Advanced Materials* 30.46 (2018), p. 1804450. DOI: 10.1002/adma.201804450 (cited on page 71).

[156] Laura M. Herz. "Charge-Carrier Mobilities in Metal Halide Perovskites: Fundamental Mechanisms and Limits." In: *ACS Energy Lett* 2.7 (2017), pp. 1539–1548. DOI: 10.1021/acsenergylett.7b00276 (cited on page 71).

[157] Bin Yang, Xin Mao, Feng Hong, Weiwei Meng, Yuxuan Tang, Xusheng Xia, Songqiu Yang, Weiqiao Deng, and Keli Han. "Lead-Free Direct Band Gap Double-Perovskite Nanocrystals with Bright Dual-Color Emission." In: *J. Am. Chem. Soc.* 140.49 (2018), pp. 17001–17006. DOI: 10.1021/jacs.8b07424 (cited on page 74).

[158] Subramaniam Ramya, Devaraj Nataraj, Sangameswaran Krishnan, Sellan Premkumar, Thankappan Thrupthika, Arumugam Sangeetha, Kittusamy Senthilkumar, and T. Daniel Thangadurai. "Aggregation induced emission behavior in oleylamine acetone system and its application to get improved photocurrent from In2S3 quantum dots." In: *Scientific Reports* 10.1 (2020), p. 19712. DOI: 10.1038/s41598-020-76703-0 (cited on page 74).

[159] S. Sekar, J. George Muller, J. Karthikeyan, P. Murugan, and N. Lakshminarasimhan. "Unveiling the multifunctional roles of hitherto known capping ligand oleic acid as blue emitter and sensitizer in tuning the emission colour to white in red-emitting phosphors." In: *Phys. Chem. Chem. Phys.* 20.28 (2018), pp. 19087–19097. DOI: 10.1039/C8CP02954G (cited on page 74).

[160] Federico Locardi, Emanuela Sartori, Joka Buha, Juliette Zito, Mirko Prato, Valerio Pinchetti, Matteo L. Zaffalon, Maurizio Ferretti, Sergio Brovelli, Ivan Infante, Luca de Trizio, and Liberato Manna. "Emissive Bi-Doped Double Perovskite Cs2Ag1–xNaxInCl6 Nanocrystals." In: *ACS Energy Lett* 4.8 (2019), pp. 1976–1982. DOI: 10.1021/acsenergylett.9b01274 (cited on page 75).

[161] Shai Levy, Sasha Khalfin, Nicholas G. Pavlopoulos, Yaron Kauffmann, Galit Atiya, Saar Shaek, Shaked Dror, Reut Shechter, and Yehonadav Bekenstein. "The Role Silver Nanoparticles Plays in Silver-Based Double-Perovskite Nanocrystals." In: *Chem. Mater.* 33.7 (2021), pp. 2370–2377. DOI: 10.1021/acs.chemmater.0c04536 (cited on page 76).

[162] Jinkyung Park, Soon Gu Kwon, Samuel Woojoo Jun, Byung Hyo Kim, and Taeghwan Hyeon. "Large-Scale Synthesis of Ultra-Small-Sized Silver Nanoparticles." In: *ChemPhysChem* 13.10 (2012), pp. 2540–2543. DOI: 10.1002/cphc.201101035 (cited on page 76).

Appendix

Chemicals

All the reagents were directly used as received without further purification: $PbBr_2$ (≥98%, Aldrich), Cs_2CO_3 (≥99.99%, Aldrich), methylammonium bromide (MABr, 98%, Aldrich), 1-octadecene (ODE, 90%, Aldrich), oleylamine (OLA, 80-90%, ACROS), n-Hexane (≥99% GC, Carl Roth), oleic acid (OA, 90%, Aldrich), L-ascorbic acid (AA, ≥99%), methanol (≥99%, Aldrich), ethyl acetate, H_2PtCl_6, silver acetate (Ag(OAc), 99%, Alfa Aesar), bismuth (III) acetate ($Bi(OAc)_3$, 99%, Thermo Scientific), lecithin (97%, Carl Roth), toluene (99.5%, Sigma-Aldrich), chlorotrimethylsilane (TMSCl, 99%, Aldrich).

Synthesis of $MAPbBr_3$ and $CsPbBr_3$ NPls

In a typical preparation, MABr (0.3 mmol, 33.6 mg) and $PbBr_2$ (0.3 mmol, 110.1 mg) were added into a 30 mL glass vial with 9 mL of OA and 1 mL of OLA. The mixture was treated by tip sonication at 30 W for 10 min. Then, the reaction was quenched by an ice-water bath immediately. The synthetic method of $CsPbBr_3$ NPls is similar to that of $MAPbBr_3$ NPls. Cs_2CO_3 (0.1 mmol, 32.6 mg) was used instead of MABr (0.3 mmol, 33.6 mg). All other steps remained unchanged.

After synthesis, the crude solution was centrifuged for 5 min at 10 krpm. The supernatant was discarded, and the precipitate was redispersed in 4 mL of hexane and 8 mL of ethyl acetate to remove the residual ligands. Then the mixture was centrifuged at 10 krpm for 5 min. The supernatant was discarded, and the precipitate was washed three times with hexane. Subsequently, the product was dried by N_2.

Synthesis of $Cs_2AgBiCl_6$ NCs

Specifically, Cs_2CO_3 (16.95 mg), Ag(OAc) (17.17 mg), $Bi(OAc)_3$ (38.85 mg), 1-octadecene (5 mL), and oleic acid (1 mL) were transferred into a three-neck flask (25 mL) and degassed for 10 minutes. The mixture was heated to 120 ℃ under a nitrogen atmosphere and kept at this temperature for 30 minutes. Subsequently, the temperature of the solution was raised to 145 ℃, and lecithin (322 mg) was added. TMSCl (65 μL) was then swiftly injected into the solution, and the reaction was quenched by an ice-water bath for 30 s. The resulting product was washed with ethyl acetate as an anti-solvent and centrifuged at 12000 rpm for 4 min. The sediment was then re-dispersed in toluene (2 mL) for further measurement and storage. To control nanoparticle size, the injection temperature was set to 120, 145, and 160 ℃, individually.

List of Figures

List of Tables

List of Abbreviations

APD avalanche photodiode

BBO β-Barium borate

CB conduction band

CCD charge-coupled device

DP double perovskite

EQE external quantum efficiency

GC gas chromatograph

HAADF-STEM high-angle annular dark-field scanning transmission electron microscopy

HER hydrogen evolution rate

IRF instrument response function

LED light-emitting diode

LHP lead halide perovskite

LSPR localized surface plasmon resonance

NC nanocrystal

NP nanoparticle

NPl nanoplatelet

ND neutral density

ODE octedecene

OA oleic acid

OLA oleylamine

PSC perovskite solar cell

PL photoluminescence

PLE photoluminescence excitation

QD quantum dot

VB valence band

SOC spin-orbit coupling

SOE spin-orbit electron

SOH spin-orbit hole

TCSPC time correlated single photon counting

TCD thermal conductivity detector

TEM transmission electron microscopy

TAS transient absorption spectroscopy

TCSPC time-correlated single photon counting

TMSCl trimethylsilyl chloride

Acknowledgments

Now I come to the end of my PhD studies. It has been four and a half years since I came to Germany. I still remember the day I arrived–16.05.2021. I took a flight from my hometown, Shandong, to Shanghai, where I boarded another flight to Frankfurt. The train I had booked from Frankfurt to Munich was delayed, and eventually, I took an overnight train to the Munich train station, where Yiou picked me up. It was early in the morning; many crows were chirping, yet I felt calm. That was the beginning of my PhD journey in Germany.

My PhD began at the onset of COVID-19, followed by rising prices and the Russia–Ukraine war. These events indirectly influenced the academic environment. Before, I had never imagined how personal development could be so closely tied to global events. However, through this journey, I have learned a great deal and now have a clearer understanding of what I want to realize and pursue in the future.

I would like to express my deepest gratitude to many people.

First and foremost, I would like to thank Prof. Feldmann for giving me the opportunity to join the group, for providing a platform for science, and for your guidance throughout my studies.

I would also like to thank Yiou for picking me up at the train station, for your care, and for your collaboration.

My sincere thanks go to Amrita, Quinten, and Yiou for their guidance, and to all my colleagues for the inspiring discussions and kindness. Thank you, Mariam, Dominik, Paul, Francis, Kush, Huayang, Sushant, Anja, Philipp, Julian, Lena, Matthias, and many others. I would also like to thank Talee and Gerlinda for their help and support.

I truly appreciate the companionship of my friends in Munich (Jan, Xiangyuan, Yizhuo…) and in China (Yang Liu, for your support). I am deeply grateful to my family — I love you all so much.

I will always remember my experience in PhOG and turn it into motivation for the next chapter of my journey.